UNIVERSITE BRETAGNE LOIRE

université angers

Thèse de Doctorat

Angel Martin FERNANDEZ ALVAREZ

Mémoire présenté en vue de l'obtention du
grade de Docteur de l'Université d'Angers
sous le sceau de l'Université Bretagne Loire

Mémoire présenté en vue de l'obtention du
grade de Docteur de la Universidad Técnica Federico Santa María

Mémoire présenté en vue de l'obtention du
grade de Docteur de la Pontificia Universidad Católica de Valparaíso

École doctorale : *3MPL*

Discipline : *Science*

Unité de recherche : *UMR 6200.*

Soutenue le *21 juin 2016*

Experiments for Laser Beam Propagation through Optical Turbulence: Development, Analysis and Applications

JURY

Rapporteurs :	**German VARAS**, Maître de conférences, Pontificia Universidad Católica de Valparaíso **Samuel FLEWETT**, Maître de conférences, Pontificia Universidad Católica de Valparaíso
Examinateurs :	**Jaime ANGUITA**, Doyen, Universidad de Los Andes.
Directeur de Thèse :	**Dario PEREZ**, Professeur, Pontificia Universidad Católica de Valparaíso
Co-directeur de Thèse :	**Régis BARILLE**, Professeur, Université d'Angers

Experiments for Laser Beam Propagation through Optical Turbulence: Development, Analysis and Applications.

Angel Martín Fernández Alvarez

May 18, 2016

Doctoral Thesis

Experiments for Laser Beam Propagation through Optical Turbulence: Development, Analysis and Applications.

Angel Martín Fernández Alvarez

Universidad Técnica Federico Santa María, Departamento de Física.

Pontificia Universidad Católica de Valparaíso, Facultad de Ciencias, Instituto de Física.

Université d'Angers. Laboratoire MOLTECH-Anjou, UMR CNRS 6200.

Doctoral Thesis

presented in

Departamento de Física
Universidad Técnica Federico Santa María

To earn the degree in PhD in Physics & Docteur en Physique

by

Angel Martín Fernández Alvarez

Title

Experiments for Laser Beam Propagation through Optical Turbulence: Development, Analysis and Applications.

Directors

Darío Gabriel Pérez and Regis Barillé.

Valparaíso, Chile. June 2016

To my family

&

In memory of Bristela Muñoz
(1920–2015)

Disfruta tu cafe . . .

— Genoveva A. M.

. . . so he got up from the meal, took off his outer clothing, and wrapped a towel around his waist. After that, he poured water into a basin and began to wash his disciples' feet, drying them with the towel that was wrapped around him . . .

— John 13: 4-5

Espectacular XoRo . . .

— Vano J.F.A

Acknowledgements

Be grateful is a fundamental attribute of a person in life, and I do not want to be alien of this virtue.

First of all, to God, for all the opportunities and persons presented in this period of my life. To my family, especially to my mother and my brother for the support and encouragement over all this time.

To you, Darío, my most sincere gratitude. Especially, for the knowledge and academic advices. Also, for the chance to be one of the first members of the laboratory and for contribute to my development as a person.

To you, Regis, my most sincere respect. I am thankful for all the experiments developed here in France, as well as, all the academic experiences and the freedom to develop my dexterity in physics. They are a big part of this thesis. Also, for your human quality and for all your effort turning my stay in Angers as best as possible.

To Gustavo Funes, for the moments shared at the laboratory, as well as all the tools and skills learned from you.

To Antonin Poisson, for let me work with you and be part of your research.

To CONICyT, Becas Chile, Universidad Técnica Federico Santa María, for all the financial support throughout my postgraduate studies. Moreover, to the French government for the CAF, it was very helpful during this period of time lived in France.

To you, Mario Garavaglia, my respect and appreciation, for be an inspiration while I was an undergraduate student. Also, to Cristian D'Angelo, Fabian Mosso, for have been a part of this process.

To my friends.

June 2016.

Preface

Atmospheric turbulence, generated by a temperature differential between the Earth's surface and the atmosphere, causes effects on optical waves that have been of great interest to scientists for many years. During daytime, the Earth is hotter than the air, if it this negative temperature gradient is sufficiently strong, it can result in an inverted image known as a *mirage*, which is a meteorological phenomenon; also belong to this category *blue sky*, *rainbow*, *red sunset*, *halo*, etc. Temperature gradients are positive during nighttime hours, resulting in downward bending of light rays. This downward bending of light rays through refraction enables one to see objects, like stars, slightly below the horizon, a phenomenon called *looming*.

Day to day as atmospheric conditions vary. These varying conditions are caused by factors like rain, snow, sleet, fog, haze, pollution, etc., that can greatly limit our ability to view distant objects. These same factors also affect the transmission of electromagnetic radiation through the atmosphere, particularly optical waves.

The three primary atmospheric phenomena that affect optical wave propagation are *absorption*, *scattering*, and *refractive-index fluctuations*—i.e., *optical turbulence*. Absorption and scattering by the constituent gases and particulates of the atmosphere are wavelength dependent and give rise primarily to attenuation of an optical wave.

Wind blowing over an aerodynamically rough region of the Earth's surface in the presence of a temperature gradient creates fluctuations in the atmosphere's refractive index known as optical turbulence. Wavefront distortions in the optical wave induced by atmospheric turbulence result in a *spreading of the beam* beyond that due to pure diffraction, random variations of the position of the beam centroid called *beam wander*, and a random redistribution of the beam energy within a cross section of the beam leading to *irradiance fluctuations*. Perhaps the most well-known effect of atmospheric turbulence is the *twinkling* of stars, which is an irregular change in brightness of the image. In addition, the atmospheric turbulence that limits astronomical seeing gradually destroys the *spatial coherence* of a laser beam as it propagates through the atmosphere. Unfortunately, these detrimental effects have far-reaching consequences on astronomical imaging, free-space optical communications, remote sensing, laser satellite communication, astronomical imaging, adaptive optics, target designation, hyperspectral

LiDAR, and other applications that require the transmission of optical waves through the atmosphere. For example, the loss of spatial coherence limits the extent to which laser beams may be collimated or focused, resulting in significant power level reductions in optical communication and radar systems.

The behavior of a subportion of optical turbulence may be described in a statistical manner, and this forms the basis of most propagation theories. Consequently, the propagation of an optical wave through optical turbulence can also be described by statistical quantities (IR propagation is also contained). Inherent in the methods of analysis, theoretical studies concerning optical wave propagation through optical turbulence are typically classified into one of two general categories—*weak fluctuations* or *strong fluctuations*. Weak fluctuation theory is usually based on the *Rytov perturbation approximation*, which yields relatively simple mathematical models for a number of basic statistical quantities involving the wave field.

The experimental and theoretical results presented in this thesis are based on the Rytov method, strong fluctuation theory is not consider here. Throughout this thesis, we introduce the globally concept of *turbulence*, focusing in atmospheric turbulence. Diverse experiments have been carried out, for instance, the propagation of two parallel thin beam under geometrical optics condition for the study of the optical turbulence parameters—the same optical configuration was used to investigate the best sampling rate for optical turbulence. Furthermore, we measure evapotranspiration by remote sensing, in which we heed the fluctuations of the refractive index through the intensities of the turbulence. Finally, some experiences in which consider new transmitters are also developed, such as *flipped mode* and *supercontinuum*, showing a experimental reduction on the irradiance fluctuations induced by the turbulence. These beams have a high performance as a transmitter of information in optical communications.

Contents

List of Figures

Chapter 1

Laser Beam Propagation through Turbulent Media

Atmospheric turbulence has received most of the attention in the last years, for it covers a wide range of natural and engineering settings, especially today, its study is applied for answer a wide variety of research questions in climate science. This study is developed from the *passive scalar fields* point of view, on account of the nature of the temperature. The turbulent refractive index also belongs to this class; this is not a novelty (Tatarskĭ, 1961), due to the temperature fluctuations are proportional to those of index.

Our interest in lightwave propagation through turbulent media must start here then. That is, we have to comprehend the media before attempt a description of the propagation itself. In the forthcoming sections we will have an overview of atmospheric turbulence as it pertains to *velocity fluctuations*, *temperature fluctuations*, and *index of refraction fluctuations*. Furthermore, the primary objectives in this chapter are: introducing various models of the *power spectrum for optical turbulence* that are commonly used, a review to the *stochastic Helmholtz equation* as the governing partial differential equation for a scalar field of an optical wave propagating through a random media, together with the classical methods to solving the Helmholtz equation, e.g, the *Extended Huygens-Fresnel principle*, as well as *Born* and *Rytov* perturbation methods to predict all relevant statistical parameters under weak turbulence condition.

Above we have, without more precisions, referred to the atmospheric turbulence.

From now on, all our discussions will be targeting the atmosphere or experiments that resemble it. Of course, this section is intent to explain what '*turbulence*' is.

1.1 Turbulence

1.1.1 Kolmogorov Theory

Considering the atmosphere as a viscous fluid, two states of motion are differentiate—laminar and turbulent. The distinction between these states lies in the fact that mixing does not occur in *laminar flow* for which the velocity flow characteristics are uniform or change in some regular fashion. In *turbulent flow*, the velocity field loses its uniform characteristics due to dynamic mixing and acquires random subflows called optical turbules or *turbulent eddies*.

As it is well known fluids are governed by the Navier-Stokes equation:

$$\frac{\partial}{\partial t}\,\mathbf{v} + (\mathbf{v}\cdot\nabla)\mathbf{v} - \nu\,\triangle\mathbf{v} = \frac{1}{\rho}\,(\,\mathbf{F} - \nabla p)\,, \tag{1.1}$$

$\mathbf{v}(\mathbf{r},t) : \mathbb{R}^3 \times \mathbb{R}_+ \to \mathbb{R}^3$ is the velocity field, while ν is the kinematic viscosity of the fluid (with dimensions $[\nu] = L^2/T$), ρ the density, p the pressure and $\mathbf{F}$ the external force. It is worth noting that this equation is scale invariant. So it can be turned into the following adimensional equation,

$$\frac{\partial}{\partial\tilde{t}}\,\tilde{\mathbf{v}} + (\tilde{\mathbf{v}}\cdot\tilde{\nabla})\tilde{\mathbf{v}} - \left(\frac{\nu\tau}{l^2}\right)\tilde{\triangle}\tilde{\mathbf{v}} = \frac{1}{\tilde{\rho}}\left(\,\tilde{\mathbf{F}} - \tilde{\nabla}\tilde{p}\right), \tag{1.2}$$

with l and τ the characteristic length and time of the system. The constant multiplying the first term at the right-hand side of the latter equation introduces the Reynolds number,

$$\mathscr{R}_e(l) = \frac{v_l\,l}{\nu}, \tag{1.3}$$

v_l is the velocity change on the scale length l. The Reynolds number is a scale dependent quantity, and its magnitude measures the flow regime: it compares the non-linear advection term $(\mathbf{v}\cdot\nabla)\mathbf{v}$ against the dissipation $-\nu\,\triangle\mathbf{v}$. While low Reynolds numbers, $\mathscr{R}_e(l) \ll 1$, correspond to regular and laminar flows and intermediate numbers, $1 \lesssim \mathscr{R}_e(l) \lesssim 10^2$, exhibit complex patterns, higher Reynolds numbers, $\mathscr{R}_e(l) \gtrsim 10^4$,

drive the flow to an apparent spatial disorder: parcels of fluids follow chaotic trajectories. In particular, when the Reynolds number tends to infinity the flow exhibits a *fully developed turbulence*. The non-linear advection is preponderant because the dissipative term goes to zero. Close to the ground the characteristic scale size is $l \sim 2$ m, characteristic wind speed is 1 to 5 m/s, and $\nu \sim 0.15 \times 10^{-4}$ m^2/s, leading to large Reynolds numbers on the order $\mathscr{R}_e(l) \sim 10^5$. In such cases the motion is considered highly turbulent.

Turbulent motion of the atmosphere in the presence of moisture and temperature gradients gives rise to disturbances in the atmosphere's refractive index in the form of turbulent eddies. We define *optical turbulence* as the fluctuations in the index of refraction resulting from small temperature fluctuations.

It was Kolmogorov (1941) who first realized that from dimensional and reliable heuristic arguments that the subclass of all optical turbules could be explained. His success was to notice that the results of this analysis become universal laws in the statistical sense. The turbulent velocity field should be thought a stochastic variable in the ensemble's sense of the statistical mechanics. It is independent on how the turbulence began: it does not matter the way the energy is injected. That is, the statistics of the chosen force has no effect over the statistics of the turbulence.

Moreover, we will also assume that a fully developed turbulence is spatially isotropic, homogeneous, and stationary: for any linear transformation and translation the system looks the same.

1.1.2 Velocity fluctuations. The energy cascade in isotropic turbulence

The classical theory of turbulence developed by Kolmogorov concerns random fluctuations in both the magnitude and direction of the velocity field of a fluid. His theory was presented in terms of a set of hypotheses, based heavily on physical insight. For sufficiently large Reynolds numbers, it was hypothesized the existence of two scales, the small-scale and the large-scale structure of turbulence. The small-scale structure of turbulence is statistically homogeneous, isotropic, and independent of the large-scale structure, and further, that the motion associated with the small-scale structure is uniquely determined by the kinematic viscosity and the average rate of dissipation of

the turbulent energy per unit mass of the fluid.

In this section, to understand the structure of atmospheric turbulence, we will treat the turbulence development under the direct energy injection. The source of energy is either wind shear or convection, and it is injected by the largest disturbances of size L_0—the integral scale, called the *outer scale of turbulence*—corresponding to the size of the bath, and then it is transferred towards the smallest scales. Finally a minimum scale l_0—the microscale, called the *inner scale of turbulence*—is reached, there the energy is dumped by the viscosity into heat (the magnitude of the inner scale oscilates between 10^{-3}m and 10^{-2}m near the ground).

The range of scales l where the energy transfer happens without loss, the flux of energy from scale to scale is constant, is called *inertial range*

$$l_0 \ll l \ll L.$$

This process can be thought as a cascade of energy, called the *energy cascade theory* of turbulence due to Richardson, see Fig. 1.1, that propagates through the scales via a succession of disturbances (*eddies* which are portions of fluid with size l and velocity v_l).

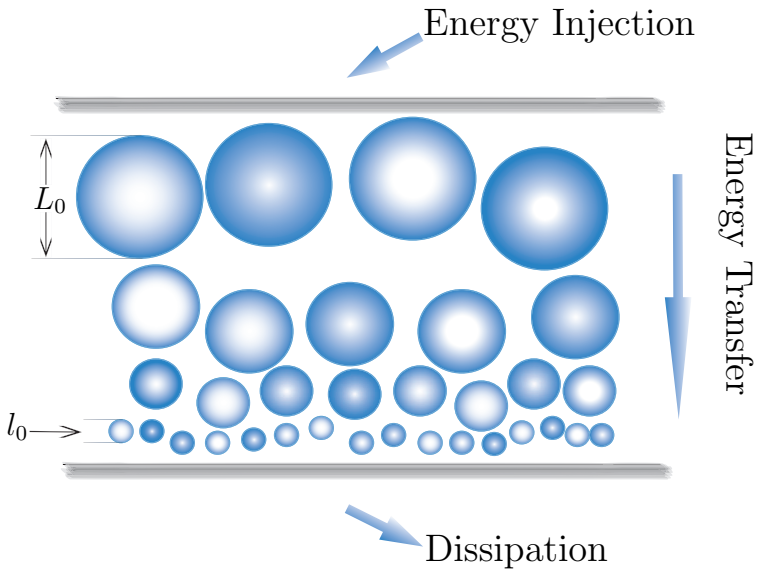

Figure 1.1: Richardson's energy cascade, where L_0 denotes the outer scale and l_0 is the inner scale. Eddies between scale sizes l_0 and L_0 form the inertial subrange.

Big eddies break up smaller ones under the influence of inertial forces. These eddies are arranged in a hierarchy according to its size, from the bigger to the smallest. Eddies of scale sizes smaller than L_0 are assumed *statistically homogeneous* and *isotropic*, whereas those equal to L_0 are generally *nonisotropic* and their structure is not well defined. The family of eddies bounded above by the outer scale L_0 and below by the inner scale l_0 forms the *inertial subrange*. Scale sizes smaller than the inner scale l_0 belong to the *viscous dissipation range*.

By using dimensional analysis, Kolmogorov showed that the longitudinal structure function of wind velocity in the inertial range satisfies the universal 2/3 power law

$$D_{RR}(R) = \langle (V_1 - V_2)^2 \rangle = C_V^2 R^{2/3}, \qquad l_0 \ll R \ll L_0, \tag{1.4}$$

where V_1, V_2 represent velocity components at two points separated by distance R and C_V^2, the velocity structure constant (in units of $\mathrm{m}^{4/3}/\mathrm{s}^2$), is a measure of the total amount of energy in the turbulence. The structure constant is related to the average energy dissipation rate ε by

$$C_V^2 = 2\varepsilon^{2/3}.$$

The velocity inner scale l_0, is on the order of the Kolmogorov microscale η, i.e.

$$l_0 \sim \eta = \left(\frac{\nu^3}{\varepsilon} \right)^{1/4}. \tag{1.5}$$

This shows that strong turbulence has smaller inner scales and weak turbulence has larger inner scales. The outer scale L_0 is proportional to $\varepsilon^{1/2}$, and unlike the inner scale, the outer scale increases and decreases directly with the strength of turbulence.

The behavior of the longitudinal structure function at small-scale sizes ($R \ll l_0$) varies with the square of separation distance R. This quadratic behavior is easily inferred from a Taylor series expansion of the structure function at small distances. The constant of proportionality is chosen so that the two power laws agree when $R = l_0$, which, when combined with Eq. (1.4), leads to the asymptotic forms

$$D_{RR}(R) = \begin{cases} C_V^2 l_0^{-4/3} R^2, & 0 \leqslant R \ll l_0, \\ C_V^2 R^{2/3}, & l_0 \ll R \ll L_0. \end{cases} \tag{1.6}$$

Because the random field of velocity fluctuations is basically nonisotropic for scale sizes larger than the outer scale L_0, no general description of the structure function can be predicted.

The 2/3 power law behavior of the structure function in the inertial range is equivalent to the power spectrum in three dimensions given by

$$\begin{aligned}\Phi_{RR}(\kappa) &= 0.066\ \varepsilon^{2/3}\kappa^{-11/3} \\ &= 0.033 C_V^2 \kappa^{-11/3}, \qquad 1/L_0 \ll \kappa \ll 1/l_0,\end{aligned} \tag{1.7}$$

where κ is the spatial wave number, also called the scalar *spatial frequency* (in units of rad/m). Observe that the power spectrum exhibits a $-11/3$ power law, which corresponds to a one-dimensional spectrum with a $-5/3$ power law. The validity of the power laws for the structure function and for the power spectrum have been established over a wide range of experiments. However, a number of works suggest a modest change in the power law behavior of the structure function, such small changes have little effect on second order statistical quantities, but may be important in higher-order statistics.

1.1.3 Temperature fluctuations

The basic ideas of Kolmogorov concerning velocity fluctuations have also been applied to *passive scalar fields*, such as potential temperature* (rather than absolute temperature). Temperature fluctuations are considered passive because they do not exchange energy with the velocity turbulence, i. e., fluctuations do not affect the dynamic state of the system. The inertial range for the temperature fluctuations is known as the *inertial-convective range*, in which two scales are distinguished—the inner scale l_0 and outer scale L_0. Also, the dissipation mechanism for temperature is molecular diffusion, not viscosity as in the case of velocity fluctuations. By extending the Kolmogorov theory of structure functions given above to statistically homogeneous and isotropic temperature fluctuations, we are led to the same power law relations as found with

*The potential temperature θ is related to absolute temperature T by $\theta = T + \alpha_a h$, where α_a is called the adiabatic rate and h is height above the Earth's surface. For a small range of height, we can neglect α_a and treat T as a passive scalar as we do here.

longitudinal velocity fluctuations, viz.,

$$D_T(R) = \langle (T_1 - T_2)^2 \rangle = \begin{cases} C_T^2 l_0^{-4/3} R^2, & 0 \leqslant R \ll l_0, \\ C_T^2 R^{2/3}, & l_0 \ll R \ll L_0, \end{cases} \tag{1.8}$$

where T_1, T_2 denote the temperature at two points separated by distance R and C_T^2, the temperature structure constant (in units of $\mathrm{deg}^2/\mathrm{m}^{2/3}$). The inner scale for temperature is of the same order of magnitude as the inner scale for velocity fluctuations

$$l_0 = 5.8 \left(\frac{D^3}{\varepsilon} \right)^{1/4}, \tag{1.9}$$

where D is the diffusivity of heat in air (in units of m^2/s). Based on the 2/3 power law behavior of the structure function in the inertial-convective range, the three-dimensional of temperature fluctuations takes the $-11/3$ power-law form

$$\begin{aligned} \Phi_T(\kappa) &= \frac{1}{4\pi} \, \beta \chi \varepsilon^{1/3} \kappa^{-11/3} \\ &= 0.033 C_T^2 \kappa^{-11/3}, \qquad 1/L_0 \ll \kappa \ll 1/l_0, \end{aligned} \tag{1.10}$$

where β is the Obukhov-Corrsin constant and χ is the rate of dissipation of mean-squared temperature fluctuations.

1.1.4 Refractive index fluctuations

The index of refraction n, is one of the most significant parameters of the atmosphere for optical wave propagation. It is (almost) directly proportional to temperature fluctuations. At a point $\mathbf{R}$ in space and time t, the index of refraction can be mathematically expressed by

$$n(\mathbf{R}, t) = n_0 + n_1(\mathbf{R}, t), \tag{1.11}$$

where $n_0 = \langle n(\mathbf{R}, t) \rangle \cong 1$ is the mean value of the index of refraction and $n_1(\mathbf{R}, t)$ represents the random deviation of $n(\mathbf{R}, t)$ from its mean value; thus, $\langle n_1(\mathbf{R}, t) \rangle = 0$. Time variations in the refractive index are often suppressed in the treatment of optical wave propagation. This means that the wave maintains a single frequency as it

propagates. Finally, it is customary to express Eq. (1.31) in the form

$$n(\mathbf{R}) = 1 + n_1(\mathbf{R}),$$

where $n(\mathbf{R})$ has been normalized by its mean value n_0. Fluctuations in the index of refraction are related to corresponding temperature and pressure fluctuations. In particular, the index of refraction for the atmosphere can be written for optical and IR wavelengths according to (Owens, 1967; Andrews and Phillips, 1998)

$$\begin{aligned} n(\mathbf{R}) &= 1 + 77.6 \times 10^{-6}(1 + 7.52 \times 10^{-3}\lambda^{-2})\frac{P(\mathbf{R})}{T(\mathbf{R})} \\ &\cong 1 + 79 \times 10^{-6}\frac{P(\mathbf{R})}{T(\mathbf{R})}, \end{aligned} \tag{1.12}$$

where λ is the optical wavelength, P is the pressure in millibars, and T is the temperature in kelvin. The wavelength dependence is small for optical frequencies, so we have set $\lambda = 0.5$ μm as typical in the equation above. Because pressure fluctuations are usually negligible, we see that index of refraction fluctuations associated with the visible and near-IR region of the spectrum are due primarily to random temperature fluctuations. Moreover, humidity fluctuations only contribute in the far-IR region. Changes in the optical signal due to absorption or scattering by molecules or aerosols are not considered here.

The statistical description of the random field of turbulence-induced fluctuations in the atmospheric refractive index is similar to that for the related random field of turbulent velocities. In particular, an inertial subrange exists between the outer scale L_0 and the inner scale l_0. Thus, the properties of statistical homogeneity and isotropy are inherited by the field of refractive-index fluctuations within the corresponding inertial subrange.

Because of $n_1(\mathbf{R})$ properties, the covariance function of $n(\mathbf{R})$ can be expressed as

$$B_n(\mathbf{R}_1, \mathbf{R}_2) \equiv B_n(\mathbf{R}_1, \mathbf{R}_1 + \mathbf{R}) = \langle n_1(\mathbf{R}_1) n_1(\mathbf{R}_1 + \mathbf{R}) \rangle,$$

which, if the random field of refractive-index fluctuations is statistically homogeneous, is a function of $\mathbf{R} = \mathbf{R}_1 - \mathbf{R}_2$. If the random field is both statistically homogeneous and isotropic, the covariance function further reduces to a function of only the scalar

distance $R = |\mathbf{R}_1 - \mathbf{R}_2|^2$. For statistically homogeneous and isotropic turbulence, the related structure function can be written as

$$D_n(R) = 2[B_n(0) - B_n(R)] = \begin{cases} C_n^2 l_0^{-4/3} R^2, & 0 \leqslant R \ll l_0, \\ C_n^2 R^{2/3}, & l_0 \ll R \ll L_0, \end{cases} \tag{1.13}$$

where C_n^2 is the index of refraction structure constant (in units of $m^{-2/3}$), sometimes called the structure parameter. The inner scale is $l_0 = 7.4\ \eta = 7.4\ (\nu^3/\varepsilon)^{1/4}$. The refractive-index structure constant C_n^2 is a measure of the strength of the fluctuations of the refractive index, and its behavior at a point along the propagation path can be deduced from the temperature structure function obtained from point measurements of the temperature. In this case, values of C_n^2 are connected to the temperature structure constant C_T^2, through Eq. (1.12)

$$C_n^2 = \left(79 \times 10^{-6} \frac{P}{T^2}\right)^2 C_{T.}^2 \tag{1.14}$$

Path-averaged values of C_n^2 and inner scale l_0 can be obtained simultaneously by optical measurements over a short path length, typically 150m, using an instrument called a scintillometer—see (Barillé et al., 2016) and references therein.

Values of C_n^2 typically range from 10^{-14} $\mathrm{m}^{-2/3}$ or less for conditions of "weak turbulence" and up to 10^{-12} $\mathrm{m}^{-2/3}$ or more when the turbulence is "strong". Over short time intervals at a fixed propagation distance and constant height above the ground it may be reasonable to assume that C_n^2 is essentially constant. However, for vertical and slant propagation paths the refractive index structure parameter varies as a function of height above ground.

1.2 Spectra for the flucutations of the refractive index.

As before, we are dealing with an homogeneous and isotropic turbulence. The energy is then constant throughout space. Thus, when we consider the transport of turbulent energy, this will be in wavenumber, $\boldsymbol{\kappa}$, rather than in the coordinate space. So, the

spatial power spectral density of refractive index fluctuations, $\Phi_n(\kappa)$, is related to the covariance function by the three-dimensional Fourier transform

$$\begin{aligned}\Phi_n(\kappa) &= \frac{1}{(2\pi)^3}\int\int\int_{-\infty}^{\infty} B_n(R)\exp[-i\ \boldsymbol{\kappa}\cdot\mathbf{R}]\ d^3R \\ &= \frac{1}{2\pi^2\kappa}\int_0^{\infty} B_n(R)\sin(\kappa R)R\ dR,\end{aligned} \tag{1.15}$$

where spherical symmetry has been used to obtain the last integral and $\kappa = |\boldsymbol{\kappa}|$ is the scalar wave number. By properties of the inverse Fourier transform we can obtain $B_n(R)$, and consequently, the structure function

$$\begin{aligned}D_n(R) &= 2[B_n(0) - B_n(R)] \\ &= 8\pi\int_0^{\infty}\kappa^2\Phi_n(\kappa)\left[1-\frac{\sin(\kappa R)}{\kappa R}\right]d\kappa.\end{aligned} \tag{1.16}$$

For optical wave propagation, refractive index fluctuations are caused almost exclusively by small fluctuations in temperature. Therefore, the functional form of the spatial power spectrum of refractive index fluctuations is the same as that for temperature and, further, that temperature fluctuations obey the same spectral laws as velocity fluctuations. Based on the inertial subrange and its 2/3 power law expression for the structure function, in Eq. (1.13), it can be deduced that the associated power spectral density for refractive index fluctuations satisfies

$$\Phi_n(\kappa) = 0.033C_n^2\kappa^{-11/3}, \qquad 1/L_0 \ll \kappa \ll 1/l_0. \tag{1.17}$$

The equation above it is the well known *Obukhov-Kolmogorov* (OK) spectrum. Because of its relatively simple mathematical form, it is widely used in theoretical calculations. Nonetheless, this spectrum model is theoretically valid only over the inertial subrange $1/L_0 \ll \kappa \ll 1/l_0$. To justify its use in certain calculations over all wave numbers, it is ordinarily assumed that the outer scale is infinite and the inner scale is negligibly small. However, Eq. (1.17) is acceptable, if and only if the integrals that contain $\Phi_n(\kappa)$ are convergent.

Other spectral models have been proposed for making calculations when scale effects cannot be ignored. For purposes of mathematical convenience, it is suggested

a Gaussian function that essentially truncates the spectrum at high wave numbers, obtaining (Tatarskǐ, 1961; Andrews and Phillips, 1998):

$$\Phi_n(\kappa) = 0.033 C_n^2 \kappa^{-11/3} \exp\left(- \frac{\kappa^2}{\kappa_m^2} \right), \qquad \kappa \ll 1/L_0, \qquad \kappa_m = 5.92/l_0. \tag{1.18}$$

This spectrum is widely called the *Tatarskǐ spectrum*. Like the Kolmogorov spectrum, the Tatarskǐ spectrum has a singularity at $\kappa = 0$ or $L_0 \to \infty$. This means, that the structure function $D_n(R)$ can be calculated but the covariance function $Bn_(R)$ cannot. Although atmospheric turbulence is almost always locally homogeneous and isotropic, the spatial power spectrum is isotropic only in the inertial subrange or dissipation range for which $\kappa > 1/L_0$.

There is a third spectrum which allows wave numbers in the input range $\kappa < 1/L_0$, i. e., $\kappa \to 0$:

$$\Phi_n(\kappa) = \frac{0.033 C_n^2}{(\kappa^2 + \kappa_0^2)^{-11/6}}, \qquad 0 \leq \kappa \ll 1/l_0, \qquad \kappa_0 = 2\pi/L_0. \tag{1.19}$$

The spectrum above is called *von Kármán*[†]. Finally, modifications of the *Tatarskǐ* and *von Kármán* spectrum let that the turbulence can be modeled as if it were statistically homogeneous and isotropic over all wave numbers. This spectrum is named *modified von Kármán spectrum*, and is given by:

$$\Phi_n(\kappa) = \frac{0.033 C_n^2}{(\kappa^2 + \kappa_0^2)^{-11/6}} \exp\left(- \frac{\kappa^2}{\kappa_m^2} \right), \qquad 0 \leq \kappa < \infty. \tag{1.20}$$

Both spectra are reduced to the Kolmogorov spectrum in the inertial subrange. These models are based in mathematical convenience and they are widely used.

Another spectrum model with outer scale parameter is the *exponential spectrum*

$$\Phi_n(\kappa) = 0.033 C_n^2 \kappa^{-11/3} \left[1 - \exp\left(- \frac{\kappa^2}{\kappa_0^2} \right) \right], \qquad 0 \leq \kappa \ll 1/l_0. \tag{1.21}$$

Here κ_0 is related to outer scale in general by $\kappa_0 = C_0/L_0$, where the scaling constant

[†]Due to the outer scale is not well defined, the numerator can change. Therefor, we can find: 1, 4π up to 8π (Andrews and Phillips, 1998)

C_0 is chosen differently depending on the application.

However, from the experimental data appear the non-Kolmogorov (non-K) turbulence. Non-K turbulence is the name given for all kind of turbulences which do not present the classical behavior $\kappa^{-11/3}$ in the inertial range.[‡] Furthermore, it is considered non-K turbulence those ones where its structure function does not fulfill the behavior $r^{2/3}$. Therefore, there are spectra which feature a physical background, e.g., *modified atmospheric*—it is an spectrum defined for all wave numbers, $0 \leq \kappa < \infty$. Moreover, there is a *generalized (non-K) von Kármán spectrum* in function of the Hurst parameter, introduced by Toselli et al. (2007)

$$\Phi_n(\kappa) = \frac{\sin(\pi H)\Gamma(2H+2)}{4\pi^2} C_n^2 \frac{\exp\left[-\kappa^2/\kappa_m^2\right]}{(\kappa^2+\kappa_0^2)^{H+3/2}}, \qquad 0 < H \leqslant 1/3. \tag{1.22}$$

Nowadays, there is a generalized spectrum for any kind of turbulence OK or not called the *quasi-wavelet spectra* (Pérez and Funes, 2015).

1.3 Random fields and atmospheric temporal statistics

An electromagnetic wave which propagates through the atmosphere is identified as a *random field* or *stochastic field*. It is the spatial variation in the complex random field that concerns us most in our applications involving optical wave propagation through a random medium. For that reason, we will suppress the time dependency of the random field in our subsequent treatment.

The statistical averages of the random field discussed in this chapter are called ensemble averages, which are connected with temporal averages. The bond between the two types of statistical averaging in our physical model of the atmosphere, is given by the so-called *frozen turbulence hypothesis of Taylor*. This hypothesis says that temporal variations of meteorological quantities at a point are produced by advection of these quantities by the mean wind speed flow and not by changes in the quantities themselves. Thus, with knowledge of the mean wind speed, we can directly convert

[‡]Here, non-Kolmogorov turbulence is referred exclusively to the modification of the exponents in the spectrum and not another phenomenons, such as loss of Gaussianity and frozen turbulence.

from spatial statistics to temporal statistics.

We note that in the atmosphere there are essentially two time scales of concern; one that is due to motion of the atmosphere across the path of observation and the other resulting from dynamics of the turbulent eddies. The first time scale, that due to advection, can be estimated by $L_0/V_\perp$, where L_0 is the outer scale of turbulence and $V_\perp$ is the mean wind speed transverse to the observation path. This time scale is typically on the order of 1 s. The second time scale, associated with the eddy turnover time, is typically on the order of 10 s. Because the second time scale is much slower than the first, it can ordinarily be neglected in comparison with the mean wind flow. Hence, under the *Taylor frozen turbulence hypothesis*, turbulent eddies are treated as frozen in space and moved across the observation path by the mean wind speed component. However, Taylor's hypothesis fails when $V_\perp$ is considerably less than the magnitude of turbulent fluctuations in wind velocity, such as occurs when the mean wind speed is parallel/near parallel to the line of sight.

1.4 Free space propagation of optical waves

Let us denote the electromagnetic field by $u(\mathbf{R}, t)$, which is a function of $\mathbf{R} = (x, y, z)$ and time t that satisfies the wave equation

$$\nabla^2 u = \frac{1}{c^2}\frac{\partial^2 u}{\partial t^2}, \tag{1.23}$$

where ∇^2 is the Laplacian and c represents the speed of the propagating wave in the medium, for our study it corresponds to the speed of light. In this chapter, we look for solutions where the time variations in the field are sinusoidal, usually called a monochromatic wave, this is $u(\mathbf{R}, t) = U_0(\mathbf{R})e^{-i\omega t}$; where ω is the angular frequency and $U_0(\mathbf{R})$ is the complex amplitude of the wave. The substitution of this solution form into the wave equation leads to the time-independent reduced wave equation, or *Helmholtz equation*

$$\nabla^2 U_0 + k^2 U_0 = 0, \tag{1.24}$$

where k is the optical wave number related to the optical wavelength λ by
$k = 2\pi/\lambda = \omega/c$.

The classical approaches to solve the Helmholtz equation are: *paraxial approximation*, *extended Huygens Fresnel principle*, and *Feynman path integral*, the last one is not consider here; see Andrews and Phillips (1998) and Charnotskii (2015).

1.4.1 Paraxial wave equation

We can further reduce the Helmholtz equation to what is called the paraxial wave equation. Under the paraxial approximation is based on the notion that the propagation distance for an optical wave along the z-axis is much greater than the transverse spreading of the wave. From which we obtain the *paraxial wave equation*

$$\frac{1}{r}\frac{\partial}{\partial r}\left(r\frac{\partial V}{\partial r}\right) + 2ik\frac{\partial V}{\partial z} = 0. \tag{1.25}$$

where we replaced $V(r,z) = U_0(r,z)e^{-ikz}$ assuming cylindrical symmetry. The slowly varying field envelope is denoted by $V(r,z)$ and e^{-ikz} depicts the fast oscillating phasor.

There are basically two methods of solution of the paraxial wave equation, one called the direct method and the other relying on the classical Huygens-Fresnel principle, also called Huygens-Fresnel integral (Andrews and Phillips, 1998).

1.4.2 Extended Huygens–Fresnel principle

The Extended Huygens-Fresnel principle provides a method of analysis for the Helmholtz equation. This principle is the most common technique used in theoretical studies of the optical propagation, including turbulence. Henceforth, the complex amplitude at propagation distance z from the source will be represented by the *Huygens-Fresnel integral*

$$U_0(\mathbf{r},z) = -2ik\int\int_{-\infty}^{\infty} G(\mathbf{s},\mathbf{r};z)\; U_0(\mathbf{s},0)\; d^2s, \tag{1.26}$$

where $U_0(\mathbf{s},z)$ is the optical wave at the source plane and $G(\mathbf{s},\mathbf{r};z)$ is the free-space Green's function. In general, the free-space Green's function is a spherical wave which, under the paraxial approximation,

$$G(\mathbf{s},\mathbf{r};z) = \frac{e^{ik|\mathbf{R}-\mathbf{S}|}}{4\pi|\mathbf{R}-\mathbf{S}|} \simeq \frac{1}{4\pi z}\exp\left[ikz + \frac{ik}{2z}|\mathbf{s}-\mathbf{r}|^2\right]. \tag{1.27}$$

therefore,

$$U_0(\mathbf{r}, z) \simeq -\frac{ik}{2\pi z} \exp[ikz] \int\int_{-\infty}^{\infty} U_0(\mathbf{s}, 0) \exp\left[\frac{ik}{2z}|\mathbf{s}-\mathbf{r}|^2\right] d^2s. \tag{1.28}$$

this result will be fundamental in the following chapters.

1.5 Stochastic wave equation

Optical wave propagation in an unbounded continuous medium with smoothly varying stochastic refractive index; is governed by a differential equation with random coefficients which is called *stochastic wave equation*

$$\nabla^2\mathbf{E} + k^2n^2(\mathbf{R})\mathbf{E} + 2\nabla[\mathbf{E}\cdot\nabla\log n(\mathbf{R})] = \mathbf{0}, \tag{1.29}$$

we are assuming that time variations in the refractive index are sufficiently slow that a quasi steady-state approach can be used, which permits us to treat $n(\mathbf{R})$ as a function of position only.

The stochastic wave equation can be reduced by imposing a simple set of fundamental assumptions on the propagating wave. Backscattering and depolarization effects are neglected, because the wavelength for optical radiation is much smaller than the inner scale of turbulence. As a further consequence, the term relating to the change in polarization of the wave as it propagates is negligible. By dropping this term, Eq. (1.29) simplifies to

$$\nabla^2\mathbf{E} + k^2n^2(\mathbf{R})\mathbf{E} = \mathbf{0}.$$

If we let $U(\mathbf{R})$ denotes one of the scalar components that is transverse to the direction of propagation along the positive z-axis, the approximate stochastic wave equation is replaced by the *scalar stochastic Helmholtz equation*

$$\nabla^2U(\mathbf{R}) + k^2n^2(\mathbf{R})U(\mathbf{R}) = 0. \tag{1.30}$$

Then again, we assume that the refractive index is delta correlated in the direction of propagation. This leaves both, the well known *Markov approximation* in the

statistically homogeneous covariance function and the refractive index expressed as:

$$n(\mathbf{R}) = n_0 + n_1(\mathbf{R}), \tag{1.31}$$

where $n_0 = \langle n(\mathbf{R})\rangle \cong 1$, and $n_1(\mathbf{R})$ is a small random quantity with mean value zero, thus $\langle n_1(\mathbf{R})\rangle = 0$.

Even with the above simplifications, Eq. (1.30) has proven difficult to solve. Historically, the first approach to solving the problem was based on the method of Green's function, reducing it to an equivalent integral equation. Some more fruitful early attempts to solve scalar stochastic Helmholtz equation were based on the geometrical optics method (GOM), which ignores diffraction effects, and on two perturbation theories widely known as the *Born* and *Rytov approximation*. Both of these perturbation theories are restricted to regimes of *weak irradiance fluctuations*.

To solve Eq. (1.30) under small random fluctuations of the index of refraction, we first write its square as

$$n^2(\mathbf{R}) = [n_0 + n_1(\mathbf{R})]^2 \simeq 1 + 2n_1(\mathbf{R}), \quad |n_1(\mathbf{R})| \ll 1. \tag{1.32}$$

Then, the optical field can be expressed as sum of terms

$$U(\mathbf{R}) = U_0(\mathbf{R}) + U_1(\mathbf{R}) + U_2(\mathbf{R}) + \ldots, \tag{1.33}$$

$U_0(\mathbf{R})$ denotes the unperturbed portion of the field in the absence of turbulence and the remaining terms represent perturbations caused by random inhomogeneities. It is generally assumed that $|U_2(\mathbf{R})| \ll |U_1(\mathbf{R})| \ll |U_0(\mathbf{R})|$. The *Born approximation* method reduces the Eq. (1.30) to a system of differential equations with constant coefficients. The procedure we use is to substitute Eq. (1.32) and Eq. (1.33) into Eq. (1.30) and then equate term of the same order, thus

$$\nabla^2 U_0 + k^2 U_0 = 0, \tag{1.34}$$

$$\nabla^2 U_1 + k^2 U_1 = -2k^2 n_1(\mathbf{R}) U_0(\mathbf{R}), \tag{1.35}$$

$$\nabla^2 U_2 + k^2 U_2 = -2k^2 n_1(\mathbf{R}) U_1(\mathbf{R}), \tag{1.36}$$

The solution of the homogeneous Eq. (1.34), is simply the unperturbed field $U_0(\mathbf{R})$

studied in Sec. 1.4. Each of the nonhomogeneous equations can be solved by the method of Green's function.

The solution of Eq. (1.35) can be expressed in the integral form

$$U_1(\mathbf{R}) = \int\int\int_V G(\mathbf{S},\mathbf{R})[2k^2 n_1(\mathbf{S})U_0(\mathbf{S})]d^3S \tag{1.37}$$

where $U_0(\mathbf{R})$ is known and $G(\mathbf{S},\mathbf{R}) \equiv G(\mathbf{R},\mathbf{S})$ is the Green's function. From the conditions proposed in 1.5, and to use the Eq. (1.27) at 1.4.2, the *first-order perturbation* takes the specific form

$$U_1(\mathbf{r},L) = \frac{k^2}{2\pi}\int_0^L dz \int\int_{-\infty}^{\infty} d^2s \exp\left[ik(L-z) + \frac{ik|\mathbf{s}-\mathbf{r}|^2}{2(L-z)}\right] U_0(\mathbf{s},z)\frac{n_1(\mathbf{s},z)}{L-z}. \tag{1.38}$$

Because $\langle n_1(\mathbf{s},z)\rangle = 0$ by definition, it follows that the ensemble average of the first-order Born approximation also vanishes, i.e., $\langle U_1(\mathbf{r},L)\rangle = 0$. Next, recursively the mth-order perturbation term can be expressed as

$$U_m(\mathbf{r},L) = \frac{k^2}{2\pi}\int_0^L dz \int\int_{-\infty}^{\infty} d^2s \exp\left[ik(L-z) + \frac{ik|\mathbf{s}-\mathbf{r}|^2}{2(L-z)}\right] U_{m-1}(\mathbf{s},z)\frac{n_1(\mathbf{s},z)}{L-z}. \tag{1.39}$$

where $m = 1, 2, 3, \ldots$.

A different perturbational approach to solving Eq. (1.30), is called the *Rytov approximation*. Restricted to weak fluctuation conditions, the Rytov method consists of writing the field of the electromagnetic wave as

$$U(\mathbf{R}) \equiv U(\mathbf{r},L) = U_0(\mathbf{r},L)\exp[\psi(\mathbf{r},L)], \tag{1.40}$$

where ψ is a *complex phase perturbation* due to turbulence that takes the form

$$\psi(\mathbf{r},L) = \psi_1(\mathbf{r},L) + \psi_2(\mathbf{r},L) + \ldots. \tag{1.41}$$

$\psi_1(\mathbf{r},L)$ and $\psi_2(\mathbf{r},L)$ represent the first-order and second-order complex phase perturbations, respectively. Straightforward, we can relate these perturbation terms directly to the Born perturbations already calculated. To do so, it is convenient to introduce

the *normalized Born perturbations* defined by

$$\Phi_m(\mathbf{r}, L) = \frac{U_m(\mathbf{r}, L)}{U_0(\mathbf{r}, L)}, \quad m = 1, 2, 3, \ldots. \tag{1.42}$$

By equating the first-order Rytov and first-order Born perturbations according to

$$\begin{aligned} U_0(\mathbf{r}, L)\exp[\psi_1(\mathbf{r}, L)] &= U_0(\mathbf{r}, L) + U_1(\mathbf{r}, L) \\ &= U_0(\mathbf{r}, L)[1 + \Phi_1(\mathbf{r}, L)] \end{aligned} \tag{1.43}$$

the perturbations at first-order are equal under

$$\psi_1(\mathbf{r}, L) = \ln[1 + \Phi_1(\mathbf{r}, L)] \cong \Phi_1(\mathbf{r}, L), \quad |\Phi_1(\mathbf{r}, L)| \ll 1 \tag{1.44}$$

therefore, the normalized perturbation is given by

$$\begin{aligned} \Phi_1(\mathbf{r}, L) &= \frac{U_1(\mathbf{r}, L)}{U_0(\mathbf{r}, L)} \\ &= \frac{k^2}{2\pi}\int_0^L dz \int\int_{-\infty}^{\infty} d^2 s \exp\left[ik(L-z) + \frac{ik|\mathbf{s}-\mathbf{r}|^2}{2(L-z)}\right]\frac{U_0(\mathbf{s}, z)}{U_0(\mathbf{r}, L)}\frac{n_1(\mathbf{s}, z)}{(L-z)}. \end{aligned} \tag{1.45}$$

As before, recursively, the integral representation for the second-order of the normalized Born perturbation, is obtained from Eq. (1.39), thus

$$\begin{aligned} \Phi_2(\mathbf{r}, L) &= \frac{U_2(\mathbf{r}, L)}{U_0(\mathbf{r}, L)} \\ &= \frac{k^2}{2\pi}\int_0^L dz \int\int_{-\infty}^{\infty} d^2 s \exp\left[ik(L-z) + \frac{ik|\mathbf{s}-\mathbf{r}|^2}{2(L-z)}\right]\frac{U_0(\mathbf{s}, z)}{U_0(\mathbf{r}, L)}\frac{\Phi_1(\mathbf{s}, z) n_1(\mathbf{s}, z)}{L-z}. \end{aligned} \tag{1.46}$$

by equating the Born and Rytov perturbations through second-order terms, we see that

$$U_0(\mathbf{r}, L)\exp[\psi_1(\mathbf{r}, L) + \psi_2(\mathbf{r}, L)] = U_0(\mathbf{r}, L)[1 + \Phi_1(\mathbf{r}, L) + \Phi_2(\mathbf{r}, L)]. \tag{1.47}$$

if besides we assume $|\Phi_2(\mathbf{r}, L)| \ll 1$ and from Eq. (1.44) we can writing the equality of

perturbations at second-order

$$\psi_2(\mathbf{r}, L) = \Phi_2(\mathbf{r}, L) - \frac{1}{2}\Phi_1^2(\mathbf{r}, L). \tag{1.48}$$

The first-order perturbation is sufficient for calculating several of the statistical quantities of interest, such as the log-amplitude variance, phase variance, intensity and phase correlation functions, and the wave structure function. However, to obtain any of the statistical moments of the optical field from the Rytov theory, including the mean value $\langle U(\mathbf{r}, L)\rangle$, it is necessary to incorporate the second-order perturbation ψ_2 in addition to the first-order perturbation ψ_1. Hence, both Rytov perturbation terms will play a major role in our later calculations involving the second-order and fourth-order moments of the field.

The first-order spectral respresentation is accomplished in part by writing the index-ofrefraction fluctuation in the form of a *two-dimensional* Riemann-Stieltjes integral (Tatarskĭ, 1971, Chp. 1, Sec. 4).

$$n_1(\mathbf{s}, L) = \int\int_{-\infty}^{\infty} \exp[i\boldsymbol{\kappa}\cdot\mathbf{s}]\ d\nu(\boldsymbol{\kappa}, z) \tag{1.49}$$

where $d\nu(\boldsymbol{\kappa}, z)$ is the random amplitude of the refractive-index fluctuations and $\boldsymbol{\kappa} = (\kappa_x, \kappa_y, 0)$ is the three dimensional wave vector with $\kappa_z = 0$.

For the case of particular interest to us, the unperturbed field $U_0(\mathbf{r}, L)$ at propagation distance L is described by the Gaussian-beam wave

$$U_0(\mathbf{r}, z) = (\Theta - i\Lambda)\exp\left[ikz + \frac{ik}{2z}\left(\overline{\Theta} + i\Lambda\right)\|\mathbf{r}\|^2\right] \tag{1.50}$$

where $\overline{\Theta} = 1 - \Theta$, $\Theta - i\Lambda = 1/(\Theta_0 + i\Lambda_0)$, with

$$\Theta_0 = 1 - \frac{z}{F_0}, \quad \text{and} \quad \Lambda_0 = \frac{2z}{kW_0^2} \tag{1.51}$$

the *curvature* and *Fresnel parameters*, respectively. Replacing Eqs. (1.49) and (4.5)

into Eq. (1.45), we get the *first-order spectral representation*

$$\begin{aligned}\psi_1(\mathbf{r}, L) = \Phi_1(\mathbf{r}, L) = \\ = ik \int_0^L dz \int \int_{-\infty}^{\infty} d\nu(\boldsymbol{\kappa}, z) \exp\left[i\gamma \boldsymbol{\kappa} \cdot \mathbf{r} - \frac{i\kappa^2 \gamma}{2k}(L - z) \right].\end{aligned} \tag{1.52}$$

where $\kappa = |\boldsymbol{\kappa}|$ and $\gamma = \gamma(z)$ is the complex *path amplitude weighting parameter* defined by

$$\gamma = \frac{\Theta_0(z) + i\Lambda_0(z)}{\Theta_0(L) + i\Lambda_0(L)} = \frac{1 + i\alpha_0 z}{1 + i\alpha_0 L} = \frac{p(z)}{p(L)}, \tag{1.53}$$

$$\alpha_0 = \frac{2}{kW_0^2} + i\frac{1}{F_0}. \tag{1.54}$$

W_0 and F_0 are respectively the *effective beam radius* and *radius of curvature* at the input or transmitter plane—see Andrews and Phillips (1998, Sec. 5.4.1) for details.

Under the same procedure, we begin by inserting Eqs. (1.49) and (4.5), and Eq. (1.52); into Eq. (1.46). On doing so, we are led to the *second-order spectral representation* for the normalized second order Born perturbation given by

$$\begin{aligned}\Phi_2(\mathbf{r}, L) = \psi_2(\mathbf{r}, L) + \frac{1}{2}\psi_1^2(\mathbf{r}, L) = \\ = -k^2 \int_0^L dz \int_0^z dz' \int \int_{-\infty}^{\infty} \int \int_{-\infty}^{\infty} d\nu(\boldsymbol{\kappa}, z) d\nu(\boldsymbol{\kappa}', z') \\ \times \exp\left[i\gamma(\boldsymbol{\kappa} + \gamma' \boldsymbol{\kappa}') \cdot \mathbf{r} - \frac{i\gamma |\boldsymbol{\kappa} + \gamma' \boldsymbol{\kappa}'|^2}{2k}(L - z) - \frac{i\gamma' \kappa'^2}{2k}(z - z') \right].\end{aligned} \tag{1.55}$$

where $\gamma' = (1 + i\alpha_0 z')/(1 + i\alpha_0 z)$.

Before to defining the statistical moments, we need to introduce the strength of turbulence and how it is classified.

1.5.1 Weak and strong fluctuation conditions

Theoretical studies of optical wave propagation are traditionally classified as belonging to either weak, moderate or strong fluctuation theories. When using the Kolmogorov spectrum—see Sec. 1.2, in the study of *plane wave* that has propagated over a path of length L, represented by $U_0(r, L) = A_0 \exp(i\varphi_0 + ikL)$—with amplitude A_0, phase φ_0,

and optical wave number denoted by k. It is customary to distinguish between these cases by values of *Rytov variance*

$$\sigma_R^2 = 1.23\ C_n^2\ k^{7/6}\ L^{7/6}, \tag{1.56}$$

where C_n^2 is the refractive index structure parameter. Fluctuations are classified as follows:

$$\sigma_R^2 = \begin{cases} < 1 & \textit{weak} \\ \simeq 1 & \textit{moderate} \\ > 1 & \textit{strong} \end{cases}$$

For a Gaussian-beam wave and arbitrary refractive-index spectral model, weak fluctuations are also described by

$$q < 1 \quad \text{and} \quad q\Lambda < 1$$

where the parameter $q = L/k\rho_{pl}^2$ and ρ_{pl} is the plane wave spatial coherence radius—see Andrews and Phillips (1998, Sec. 6.4.1) for details. The diffraction parameter is denoted by $\Lambda = 2L/kW^2$ with W is the free space beam radius at the receiver.

1.5.2 Statistical moments

Optical wave propagation through a random medium characterized by small fluctuations in the refractive index, cause spreading of the beam beyond that due to pure diffraction, random wandering of the instantaneous beam center, loss of spatial coherence, and random fluctuations in the irradiance and phase. Scale sizes larger than the beam diameter cause beam wander, whereas scale sizes on the order of the first Fresnel zone are the primary cause of irradiance fluctuations. These detrimental effects are embedded in the behavior of the beam throughout the turbulence. Knowledge of the behavior of an optical wave in turbulence is important in optical communications, laser radar, imaging, adaptive optics, target designation, ranging, and remote sensing, among other areas. The beam behavior is described by the *statistical moments*.

Throughout this thesis, ψ is considered as a Gaussian random variable, and it fulfills

$$\langle \exp[\psi(\mathbf{r}, L)] \rangle = \exp\left[\langle \psi(\mathbf{r}, L) \rangle + \frac{1}{2} \left(\langle \psi(\mathbf{r}, L)^2 \rangle - \langle \psi(\mathbf{r}, L) \rangle^2 \right) \right]. \tag{1.57}$$

Therefore, the *probability density function* (PDF) for the complex phase perturbation of the field due to random inhomogeneities, is completly defined by gaussian function with parameters, such as the mean and the variance.

From previous results—see Sec. 1.5, we have that $\langle \psi_1(\mathbf{r}, L)\rangle = \langle \Phi_1(\mathbf{r}, L)\rangle = 0$ as a consequence of $\langle n_1(\mathbf{r}, L)\rangle = 0$. Ensemble averages of second-order approximations, however, do not vanish. Thus, if we let $\mathbf{r}_1$ and $\mathbf{r}_2$ denote two points in the transverse plane at $z = L$, it is notationally expedient in our following work to define the three second-order statistical moments:

$$E_1(\mathbf{r}, \mathbf{r}) \equiv \langle \Phi_2(\mathbf{r}, L)\rangle = \langle \psi_2(\mathbf{r}, L)\rangle + \frac{1}{2}\langle \psi_1^2(\mathbf{r}, L)\rangle, \tag{1.58}$$

$$E_2(\mathbf{r}_1, \mathbf{r}_2) \equiv \langle \Phi_1(\mathbf{r}_1, L)\Phi_1^*(\mathbf{r}_2, L)\rangle = \langle \psi_1(\mathbf{r}_1, L)\psi_1^*(\mathbf{r}_2, L)\rangle, \tag{1.59}$$

$$E_3(\mathbf{r}_1, \mathbf{r}_2) \equiv \langle \Phi_1(\mathbf{r}_1, L)\Phi_1(\mathbf{r}_2, L)\rangle = \langle \psi_1(\mathbf{r}_1, L)\psi_1(\mathbf{r}_2, L)\rangle. \tag{1.60}$$

The asterisk in the previous equations, refers to the complex conjugate of the quantity.

1.6 Second and fourth moment

In the following sections we develop tractable expressions for various specializations of the second-order field moment associated with line-of-sight propagation. Here we derive our results using weak-fluctuation theory. Most analytic expressions obtained in the next chapters (and sections) are based on a *constant* refractive-index structure parameter C_n^2, characteristic of a near-ground *horizontal propagation path.*

1.6.1 Angle-of-Arrival fluctuations

In most applications we characterize the received wave in terms of statistical moments of the random optical field $U(\mathbf{r}, L)$, where L is the propagation distance along the positive z-axis from the emitting aperture of the transmitter to the receiver and $\mathbf{r}$ is a vector in the receiver plane transverse to the propagation axis. The *mutual coherence function* (MCF) of the wave is defined by the *second moment*

$$\Gamma_2(\mathbf{r}_1, \mathbf{r}_2, L) = \langle U(\mathbf{r}_1, L)U^*(\mathbf{r}_2, L)\rangle = \Gamma_2^0(\mathbf{r}_1, \mathbf{r}_2, L)\exp[2E_1(0, 0) + E_2(\mathbf{r}_1, \mathbf{r}_2)]\,. \tag{1.61}$$

where $\mathbf{r}_1$ and$\mathbf{r}_2$ are observation points in the receiver plane and $U^*(\mathbf{r}, L)$ denotes the complex conjugate field. $\Gamma_2^0(\mathbf{r}_1, \mathbf{r}_2, L)$ is the free-space MCF given by the unperturbed fields—$\Gamma_2^0(\mathbf{r}_1, \mathbf{r}_2, L) = U_0(\mathbf{r}_1, L)U_0^*(\mathbf{r}_2, L)$. For identical observation points, the MCF determines the *mean irradiance* from which turbulence-induced beam spread is deduced. Also obtained from the MCF is the *modulus of the complex degree of coherence* that describes the loss of spatial coherence of an initially coherent wave.

As is reviewed in Andrews and Phillips (1998, Sec. 6.5), further from the MCF can be calculated the *wave structure function* (WSF)—$D(\mathbf{r}_1, \mathbf{r}_2, L) = \mathrm{Re}[\triangle(\mathbf{r}_1, \mathbf{r}_2, L)]$—Re denotes the real part. The WSF is actually a sum of the *log-amplitude structure function*—$D_\chi(\mathbf{r}_1, \mathbf{r}_2, L)$ and the *phase structure function*—$D_S(\mathbf{r}_1, \mathbf{r}_2, L)$, the latter being the dominant component. These statistical quantities have important consequences on beam wave propagation applications such as imaging, lasercom, laser radar, etc.

Angle-of-arrival fluctuations of an optical wave in the plane of the receiver aperture are associated with image jitter (dancing) in the focal plane of an imaging system. Fluctuations in the angle of arrival β_a can be described in terms of the "phase structure function". To understand this, let ΔS denote the total phase shift across a collecting lens of diameter $2W_G$ and Δl the corresponding optical path difference. These quantities are related by $k\Delta l = \Delta S$. Under geometrical optics condition—$\sin(\beta_a) \simeq \beta_a$ and further assuming the mean $\langle \beta_a \rangle = 0$, the *variance of the AoA* remains,

$$\langle \beta_a^2 \rangle = \frac{D_S(2W_G, L)}{(2kW_G)^2} \tag{1.62}$$

where $D_S(2W_G, L)$ is the phase structure function. In the case of a spherical wave and Kolmogorov spectrum, Eq. (1.62) reduces to

$$\langle \beta_a^2 \rangle = \begin{cases} 1.09 C_n^2 L l_0^{-1/3} \left[1 - 0.72(\kappa_0 l_0)^{1/3}\right], & 2W_G \ll l_0, \\ 1.09 C_n^2 L (2W_G)^{-1/3} \left[1 - 0.72(2\kappa_0 W_G)^{1/3}\right], & 2W_G \gg l_0. \end{cases} \tag{1.63}$$

we have approximated the phase structure function by the WSF and included the effects of both inner and outer scale. Notice that Eq. (1.63) is independent of optical wavelength—however, this is true only if the Fresnel zone is sufficiently small compared with the receiver aperture diameter, i.e; $\sqrt{L/k} \gg 2W_G$.

Although the mean angle-of-arrival, or tilt angle, is zero, it is useful to introduce

the notion of the *root-mean-square* (*rms*) *angle-of-arrival*, defined by $\sqrt{\langle \beta_a^2 \rangle}$. It is wise introducing the *rms image displacement*, which is defined as the rms AoA multiplied by the focal length f of the collecting lens of the receiver. This yields, for Eq. (1.63)

$$\text{rms image jitter} = \begin{cases} f\sqrt{1.09 C_n^2 L l_0^{-1/3}\left[1 - 0.72(\kappa_0 l_0)^{1/3}\right]}, & 2W_G \ll l_0, \\ f\sqrt{1.09 C_n^2 L (2W_G)^{-1/3}\left[1 - 0.72(2\kappa_0 W_G)^{1/3}\right]}, & 2W_G \gg l_0. \end{cases} \tag{1.64}$$

1.6.2 Beam wander

The propagation of a laser beam in a free-space produces angular spread in the far-field due to natural diffraction, of the order of λ/D, where D is the beam diameter. In presence of optical turbulence, however, a finite optical beam will experience random deflections as it propagates, leading further spreading of the beam by large-scale inhomogeneity of the atmosphere, therefore the "hot spot" or *instantaneous center* of the beam will be randomly displaced in the receiver plane, producing what is commonly called *beam wander*.

Beam wander at the receiver plane can be modeled as a random tilt angle arising at the transmitter plane, similar to angle-of-arrival fluctuations of a reciprocal propagating wave with the receiver diameter replaced by the transmitter beam diameter as in Andrews and Phillips (1998, Sec. 6.6). Moreover, beam wandering is mostly caused by a large-scale turbulence near the transmitter where the outer scale of turbulence forms an upper bound on the inhomogeneity size. For this reason, the analysis often follows the Geometrical Optics (G.O) condition, where natural diffraction effects are neglected.

This phenomenon can be characterized statistically by the variance of the hot spot displacement along an axis or by the variance of the magnitude of the hot spot displacement. To develop an analytic expression for the variance of beam wander fluctuations, we will use the *long-term spot size*

$$W_{LT} \equiv W\sqrt{1+T} \tag{1.65}$$

where T is the on-axis mean irradiance. This term arises from the effects of turbulent

cells or "eddies" of all scale sizes, it can be split into different terms

$$W_{LT} = W^2(1+T) = W^2 + W^2\ T_{SS} + W^2\ T_{LS} \tag{1.66}$$

where we have partitioned the term $T = T_{SS} + T_{LS}$ into a sum of small-scale (SS) and large-scale (LS) contributions. Doing so, we can interpret the first term as that due pure diffraction spreading W, the first and middle terms as the defining "beam breathing" and the short-term beam radius $W_{ST}^2 = W^2\ T_{SS}$, and the last term as that describing "beam wander" or the variance of the instantaneous center of beam in the receiver plane $\langle r_c^2 \rangle = W^2\ T_{LS}$. Because it arises from large-scale turbulence, the last term is model by the expression

$$\begin{aligned}\langle r_c^2 \rangle &= W^2\ T_{LS} = \\ &= 4\pi^2 k^2 W^2 \int_0^L \int_0^\infty \kappa\ \Phi_n(\kappa) H_{LS}(\kappa, z) \left(1 - \exp\left[-\frac{\kappa^2 L}{k}\Lambda\xi^2\right]\right) d\kappa\ dz\end{aligned} \tag{1.67}$$

where $\xi = 1 - z/L$ and we have introduced the large-scale filter function—see Andrews and Phillips (1998, Chp. 6) and references therein,

$$H_{LS}(\kappa, z) = \exp\left[-\kappa^2 W^2(z)\right] = \exp\left[-\kappa^2 W_0^2[(1 - z/F_0)^2 + (2z/kW_0^2)^2\right] \tag{1.68}$$

where W_0 and F_0 are respectively the *effective beam radius* and *radius of curvature* at the input or transmitter plane. $W(z)$ is the free space beam radius at variable distance z $(0 < z < L)$ from the transmitter. The Gaussian filter function—Eq. (1.68) only permits random inhomogeneities equal to the beam size and larger to contribute to beam wander, thereby eliminating small-scale effects that lead to the second term in Eq. (1.66).

To emphasize the refractive nature of beam wander, we drop the diffractive term in Eq. (1.68) and use the geometrical optics approximation

$$1 - \exp\left[-\frac{\kappa^2 L}{k}\Lambda\xi^2\right] \simeq \frac{\Lambda L \kappa^2 \xi^2}{k}, \quad L\kappa^2/k \ll 1 \tag{1.69}$$

Some special cases we identify here, e.g. for an infinite outer scale—$\kappa_0 = 0$, and for

the exponential spectrum model—see Sec. 1.2, the integral in Eq. (1.67) yields

$$\langle r_c^2 \rangle = 2.42 C_n^2 L^3 W_0^{-1/3} \, {}_2F_1\left(-\frac{1}{3}, 1; 4; 1 - |\Theta_0|\right) \tag{1.70}$$

Eq. (1.70) emphasizes the close connection between beam wander in the receiver plane and the tilt angle variance $\langle \beta_a^2 \rangle$ at the transmitter of a reciprocal propagating plane wave—see Andrews and Phillips (2005, Eq. 83 at Sec. 6.5). The equation above is for a collimated, divergent, and convergent beam. For collimated beam ($\Theta_0 = 1$) the hypergeometric function in Eq. (1.70) is unity, and the expression is reduced to

$$\langle r_c^2 \rangle = 2.42 C_n^2 L^3 W_0^{-1/3} \tag{1.71}$$

from which we deduce $\langle r_c^2 \rangle \simeq L^2 \langle \beta_a^2 \rangle$ by equating $W_G = W_0$—see Sec. 1.6.1. If f is the focal length, the angle-of-arrival is recovered after divided by it—see Sec. 1.6.1. Therefore, it is well known that at first approximation, the variance of the angle-of-arrival fulfills the relation

$$\sigma_{\text{AoA}}^2 = 2.8375 C_n^2 \delta h D^{-1/3}. \tag{1.72}$$

where $D = 2W_0$ is the diameter and δh is the thickness of the turbulent layer.

1.6.3 Scintillation index

Fluctuations in the irradiance of the field are described by the *cross-coherence function* of the field or *fourth-order moment*

$$\begin{aligned} \Gamma_4(\mathbf{r}_1, \mathbf{r}_2, \mathbf{r}_3, \mathbf{r}_4, L) &= \langle U(\mathbf{r}_1, L) U^*(\mathbf{r}_2, L) U(\mathbf{r}_3, L) U^*(\mathbf{r}_4, L) \rangle = \\ &= \Gamma_2(\mathbf{r}_1, \mathbf{r}_2, L) \Gamma_2(\mathbf{r}_3, \mathbf{r}_4, L) \exp[E_2(\mathbf{r}_1, \mathbf{r}_4) + E_2(\mathbf{r}_3, \mathbf{r}_2) + E_3(\mathbf{r}_1, \mathbf{r}_3) + E_3^*(\mathbf{r}_2, \mathbf{r}_4)] \,. \end{aligned} \tag{1.73}$$

where $\Gamma(\cdot)$ is the MCF and $U^*(\mathbf{r}, L)$ denotes the complex conjugate field. Specializations of the fourth moment lead to the *second moment of irradiance* that, along with the mean irradiance, is used to define the *scintillation index*.

The irradiance fluctuations in the receiver plane resulting from optical turbulence

are commonly described as scintillation, and they are estimated by the refractive index structure parameter C_n^2. Turbulent eddies with sizes at the scale of the order of the first Fresnel zone are the primary cause of irradiance fluctuations. These fluctuations include the temporal variation in the received irradiance, such as star twinkle, and spatial variations within a receiver aperture, such as speckle. In the weak fluctuation regime, it is natural to work with the log amplitude variance σ_χ^2 rather than the irradiance variance itself σ_I^2, because the logarithm of the amplitude of an optical wave is assumed to follow a Gaussian statistical law in this regime.

The *covariance function of irradiance* at the same point in the space, is reduced to the *scintillation index* (Andrews and Phillips, 1998, Chp. 8)

$$\sigma_I^2(\mathbf{r}, L) = \frac{\langle I^2(\mathbf{r}, L)\rangle}{\langle I(\mathbf{r}, L)\rangle^2} - 1 \tag{1.74}$$

Eq. (1.74) is related to the *log-amplitude variance*, when the last one is sufficiently small ($\sigma_\chi^2 \ll 1$)

$$\sigma_I^2(\mathbf{r}, L) \simeq 4\sigma_\chi^2 = 2\ \mathrm{Re}[\mathbf{E}_2(\mathbf{r}, \mathbf{r}) + \mathbf{E}_3(\mathbf{r}, \mathbf{r})] \tag{1.75}$$

where $\mathbf{E}_2(\mathbf{r}, \mathbf{r})$ and $\mathbf{E}_3(\mathbf{r}, \mathbf{r})$ are the statistical moments defined in Sec. 1.5.2—Re denotes the real part. Therefore, we can write for a Gaussian beam

$$\begin{aligned}\sigma_I^2(\mathbf{r}, L) = 8\pi^2 k^2 L \int_0^1 \int_0^\infty \kappa\ \Phi_n(\kappa) \exp\left[-\frac{\kappa^2 L}{k}\Lambda\xi^2\right] \\ \times \mathrm{Re}\left\{ I_0(2\Lambda r\xi\kappa) - \exp\left[-\imath\frac{\kappa^2 L}{k}\xi\left(1 - (1-\Theta)\,\xi\right)\right]\right\} d\xi\ d\kappa\end{aligned} \tag{1.76}$$

the *diffraction* and *refraction* parameter are denoted by Λ and Θ, respectively—$I_0(\cdot)$ is the modified Bessel function of the first kind, $k = 2\pi/\lambda$ with wavelength λ, and L is the beam path length (m). Usually, for interpretation purpose, it is convenient to express the scintillation index as a sum of radial and longitudinal components, leading to $\sigma_I^2(\mathbf{r}, L) = \sigma_{I,r}^2(\mathbf{r}, L) + \sigma_{I,l}^2(L)$. The quantity $\sigma_{I,r}^2(\mathbf{r}, L)$ is the *radial component* of the scintillation index and describes physically the off-axis contribution to the fluctuations of the intensity and $\sigma_{I,l}^2(L)$ is called the *longitudinal component* of the scintillation index and corresponds to the on-axis scintillation index.

For the special case of a Kolmogorov spectrum—see Eq. (1.17) in Sec. 1.2, and in the

limiting cases of a plane wave ($\Theta = 1$, $\Lambda = 0$) and a spherical wave ($\Theta = \Lambda = 0$), the Eq. (1.76) is reduced, respectively, to the well-known results (Solignac, 2009; Andrews and Phillips, 1998; Tatarskĭ, 1971, Chp. 3),

$$\sigma^2_{I,pl}(L) = \sigma^2_R = 1.23 C_n^2 k^{7/6} L^{11/6} \qquad \text{plane wave,} \tag{1.77}$$

$$\sigma^2_{I,sp}(L) = 0.4\ \sigma^2_R = 0.5 C_n^2 k^{7/6} L^{11/6} \qquad \text{spherical wave.} \tag{1.78}$$

where σ^2_R is the Rytov variance.

Chapter 2

Parameters of the Optical Turbulence

Light-wave propagation through a turbulent medium has been investigated during over forty years. In this chapter we are going develop a series of experiments to study and determine several parameters of the turbulence, such as the inner and outer scale, through the application of new procedures. Also, we introduce a technique for establishing the best sampling rate for any type of optical turbulence without the requirement of a theoretical model.

2.1 Differential Laser Tracking Motion Meter (DLTMM)

Based in the studies developed by Consortini and O'Donnell (1991, 1993) we obtained an insight for the new configuration. In particular, Consortini and O'Donnell (1991) introduced one of the simplest and less expensive techniques available today, capable of capturing several parameters of the optical turbulence. It is based in a Geometric Optics (GO*) model, developed by them, for the propagation of twin thin-beams through a turbulent media; particularly, for their covariances. Experimental measurements of these correlations allowed the determination of the scales of turbulence.

*The geometrical optics approximation means that diffraction effects are negligible. It is generally characterized by the limiting case in which wavelength $\lambda \to 0$

As a result of the fluctuating nature of the refractive index in a turbulent medium any laser beam that propagates through it experiments deflections. These displacements are always perpendicular to the initial unperturbed direction of propagation, and arise from the beam phase fluctuations. This phenomenon is commonly known as laser beam wandering because of the dancing the beam performs over a screen. Since it is very sensitive to the turbulence nature, it has been used in different experimental configurations to measure the characteristic scales and parameters related to it (Masciadri and Vernin, 1997; Innocenti and Consortini, 2005; Pérez et al., 2012).

The implications of a non-Kolmogorov turbulence on the wandering statistics for any propagation distance have been studied by Pérez and Funes (2012). Specifically, they were most interested in short path propagation, and partially filled paths: conditions frequently observed in the laboratory.

In this section we introduce both an improved experimental setup and refined analyses techniques. A new version of the Differential Laser Tracking Motion Meter (DLTMM) employs cross-polarized laser beams that allows us to inspect more carefully distances in the range of the inner-scale, thus even superimposed beams can be discriminated. Moreover, in this experimental setup the convective turbulence produced by electrical heaters (see Section 2.1) previously used was superseded by a chamber that replicates isotropic atmospheric turbulence—anisotropic turbulence is also reproducible. Therefore, we are able to replicate the same state of the turbulent flow, specified by Rytov variance, for every separation between beams through the course of the experience. In this way, we are able to study the change in our Multi-fractal Detrended Fluctuation Analysis (MFDFA) quantifiers with different strengths of the turbulence, and their relation with better known optical quantities. The movements of the two laser beams are recorded at 6 kHz; this apparent oversampling is crucial for detecting the turbulence's characteristics scales under improved MFDFA techniques. The estimated characteristic scales and multi-fractal nature detected by this experiment provides insight into the non-Gaussian nature of propagated light.

The purpose of this work is to experimentally check these results, and corroborate that the simple covariances defined by the geometrical optics (GO) approximation are insufficient to describe the state of turbulent media. New statistical quantifiers are required to complete the classical methods: the MFDFA will provide insight in the development state of the turbulence.

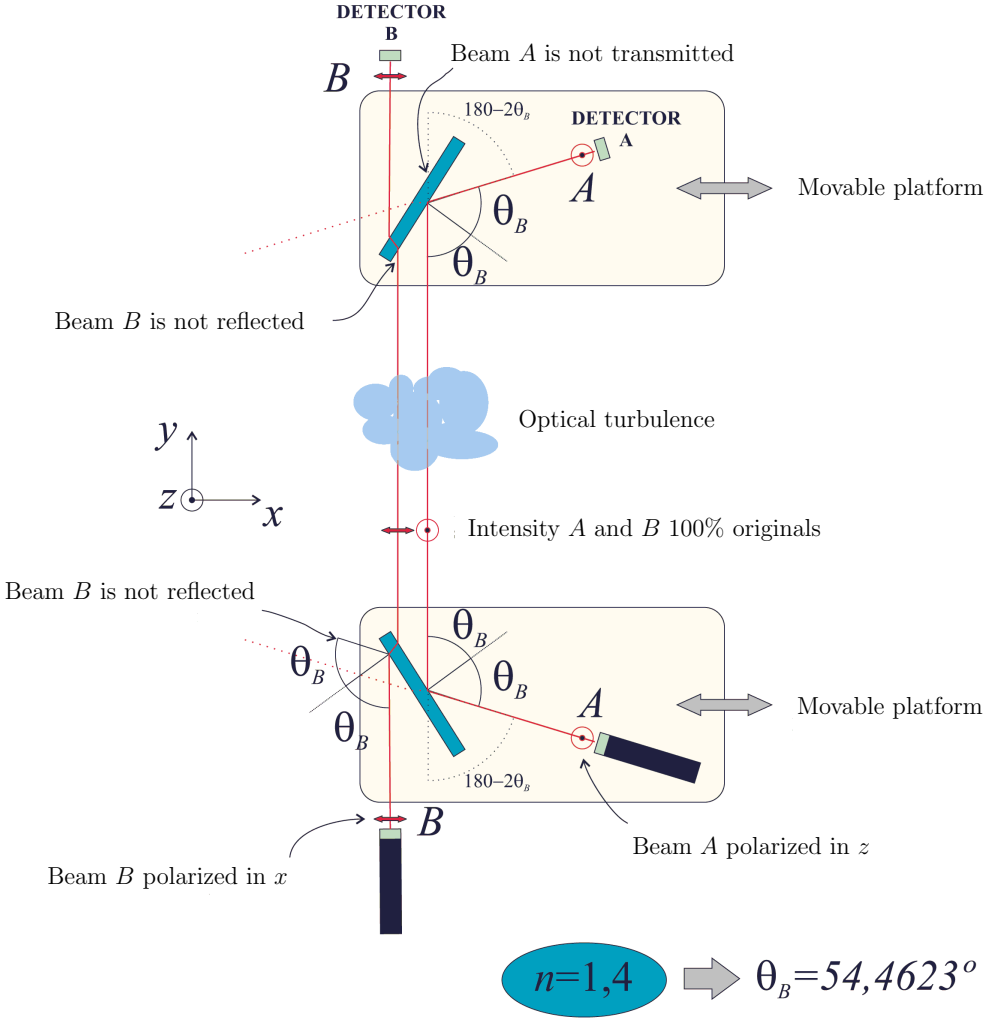

Figure 2.1: Optical configuration. It is composed by two identical lasers polarized in perpendicular directions to the propagation direction; and also, there are two movable plataforms which change the distance of beam A with respect to beam B. Beam B is fixed.

In Chile we have had a new task, it involves the improvement of a technique, DLTMM. Fig. 2.1 (Pérez, 2010), is an optical configuration for DLTMM, used as a robust device to determine many optical parameters related to atmospheric turbulence. It consisted of two thin laser beams, each beam is perpendicular polarized to the propagation distance—linearly polarized light is not affected by the turbulence. The beam B is fixed whereas the platform in which beam A is placed remains movable,

as well as the platform where the detector for beam A is positioned—its separations can be modified. Every beam splitter are positioned with the Brewster's angle to avoid the polarized beam coming from laser A going into the detector B. The beams propagate through convective air, then each random wandering was registered with position detectors, sampled at 800 Hz.

The experiment above presents a lot of limitations, for example, it is prone to mechanical vibrations and misalignments to name a few. However, one of the main problems found have been the dimensions of the instrumental optics, e.g., the displacement of the platform at the limit distance (zero), instruments at both emitter and receptor collide between them—see figure 7. in Consortini and O'Donnell (1991). Besides, we did not have two identical lasers. Those defects have not made possible to carry out the experiment at that moment in Chile.

Thereafter, we were designated to build a new optical setup for DLTMM—a more compact one, stable and efficient to averting the limitations previously mentioned. The propagation of the beams was through an optical turbulence simulator.

2.1.1 Generator of turbulence

The turbulent media was created by a *turbulator*—see Fig. 2.2, a device introduced by Keskin et al. (2006). A turbulator is a turbulence generator based in the dynamic mixing of two air fluxes at different temperatures, the technique is statistically repeatable.

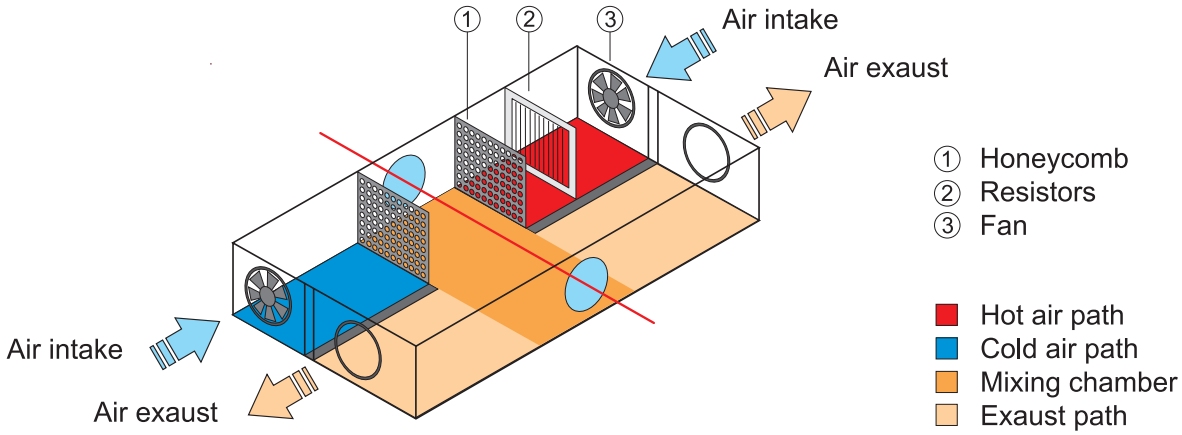

Figure 2.2: Sketch's *Turbulator*.

Real optical turbulence only appears when a temperature gradient appears in a tur-

bulence flux (i.e., air in turbulence motion). This can be achieved mixing two colliding fluxes of air at different temperatures in a confined space: the turbulence chamber. Two opposite tunnels produce turbulent air, with the same statistical properties, while in one entrance the air is heated (hot intake) the other is at ambient temperature (cold intake), the velocity of the fluxes is the same in both tunnels. In our device the optical turbulence extending over a 37 cm channel is the product of the collision of two masses of air pushed by identical fans through honeycombs placed opposite each other at the sides of this chamber.

Any device that produces optical turbulence is characterized its refractive index structure constant. There exists a basic and simple experiment that is capable of giving such constant, method of angle-of-arrival (AoA) for instance. For the characterization of the turbulator we use the method described in Section 1.6.1, and it is schematized in Fig. 2.3.

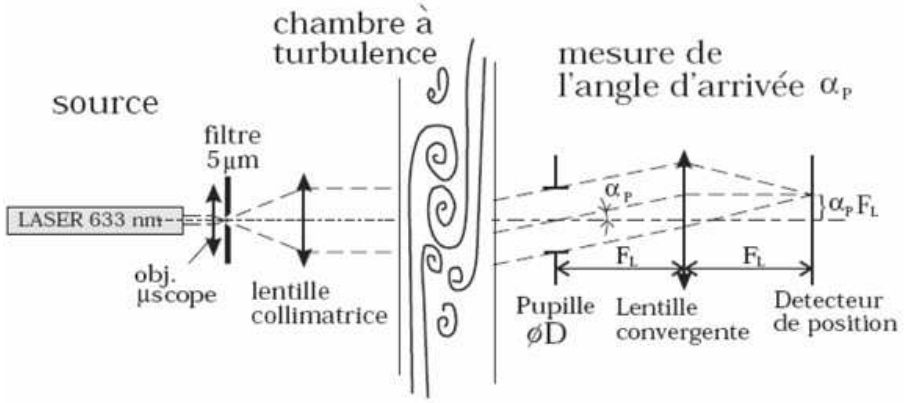

Figure 2.3: AoA setup from Pérez (2010).

The spot wandering is measured, and the angle-of-arrival is calculated from Eq. (1.72) at Sec. 1.6.2. In our laboratory we perform these tests as follows:

1. The velocity of the air flux is fixed, and at a given difference of temperature we perform the AoA measuremente for different pupil sizes. The focal distance is $f = 450$ mm, and the diameter range is between 1 and 10 cm.

2. With this focal distance the systems is very sensitive, we perform the focal point spot wandering at 1000FPS.

3. Then for each temperature difference we extrapolate the structure constant from the log-log fitting of the angle-of-arrival formula.

After an laborious measurement and analysis, the following Fig. 2.4 shows the (linear) relation between the structure constant and ΔT:

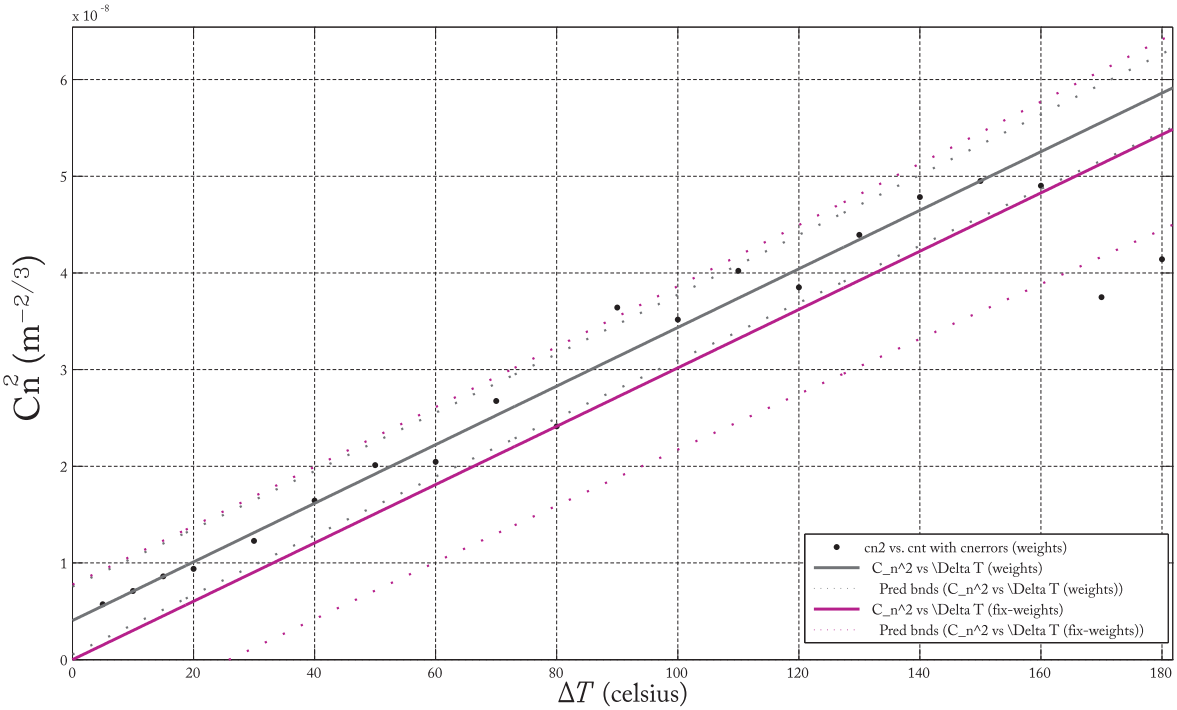

Figure 2.4: C_n^2 vs ΔT. Characterization of the turbulator. Figure from Pérez (2010).

The black line fit is without fixing the point $\Delta T = 0$ to $C_n^2 = 0$, its equation is

$$C_n^2(\Delta T) = 3.038(\pm 0.1835) \times 10^{-10} \Delta T + 4.036(\pm 1.2380) \times 10^{-9}; \quad R = 0.987, \quad (2.1)$$

while the purple line is obtained fixing the origin: the slope is exactly the same. This line, completely typifies our turbulator. This device produces turbulence with strength given by the *structure constant*, C_n^2, in the range 2.93–8.63 $\times 10^{-9}$ m$^{-2/3}$.

2.1.2 Experimental setup

For the new DLTMM setup we used two platforms, a heavier one for the emitter (Thorlabs XT95 − 5000)—photo 2.5, with two bigger drop-on right angle carriages

(Thorlabs XT95P2); and a lighter platform for the receptor (Throlabs XT66 − 500), pictured below—photo 2.6, with a pair of rail carriages (Throlabs XT66P2/M). The useful area for these is 48 × 48 mm.

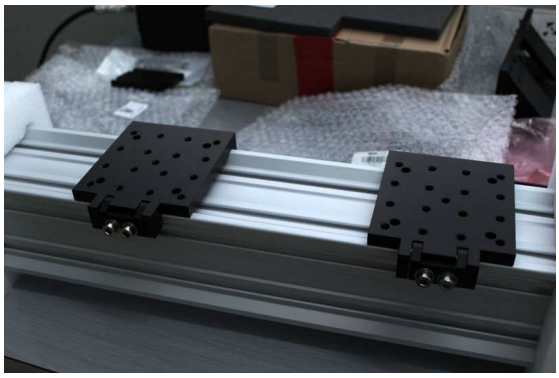

Figure 2.5: Platform XT95-5000.

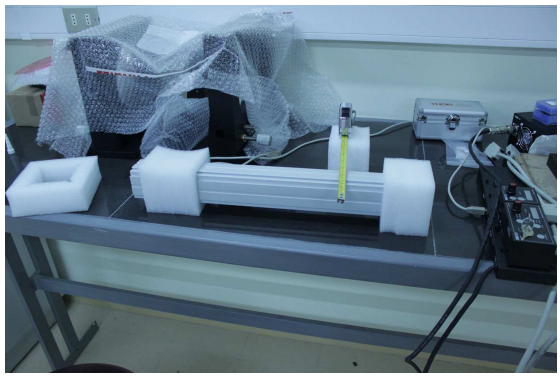

Figure 2.6: Plataform XT66-5000.

As part of the emitter platform a 35mW laser diode (λ = 635nm, DL5038-021, Thorlabs TLD001 driver) is employed, and collimating optics is setup to maintain the beam waist around 3mm along the propagation path; additionally, a $\lambda/4$ wave plate turns it a circular polarised beam (CCP). As sketched in Fig. 2.7, this laser beam is split by a 50/50 polarising cube beam splitter (PCBS), fixed to the platform. The two departing beams now are cross-polarised. The reflected beam has two more reflections (M1,M2) until exiting the emitter platform, while the transmitted beam reflects in a pellicle beam splitter (MPBS), fixed to a moving platform on a rail system, exiting the platform parallel to the first one. This system provides separations between the beams ranging from 0 to 300 mm; ultimately, the maximum separation available is 100 mm because of the limited size of the optical windows of the turbulator. Once the beams output the turbulator, at the end of the propagation a second platform is setup to measure the wandering of both beams simultaneously. Two position sensitive detectors, with an area of 1cm^2 (UDT SC-10 D) measure the centroid position of the impinging laser beam—with relative accuracy of 2.5μm, so very small position deflections can be measured. The first detector (D1) was mounted in a moving platform like the PBS splitter, but the second detector (D2) was placed out of the beam trajectory, a fixed pellicle beam splitter (FPBS) reflected the beam back to D2. With this setup we avoided the physical constrains imposed by the size of the detectors; thus, allowing us to measure simultaneously the wandering of the two beams separated by distances

under 20 mm.

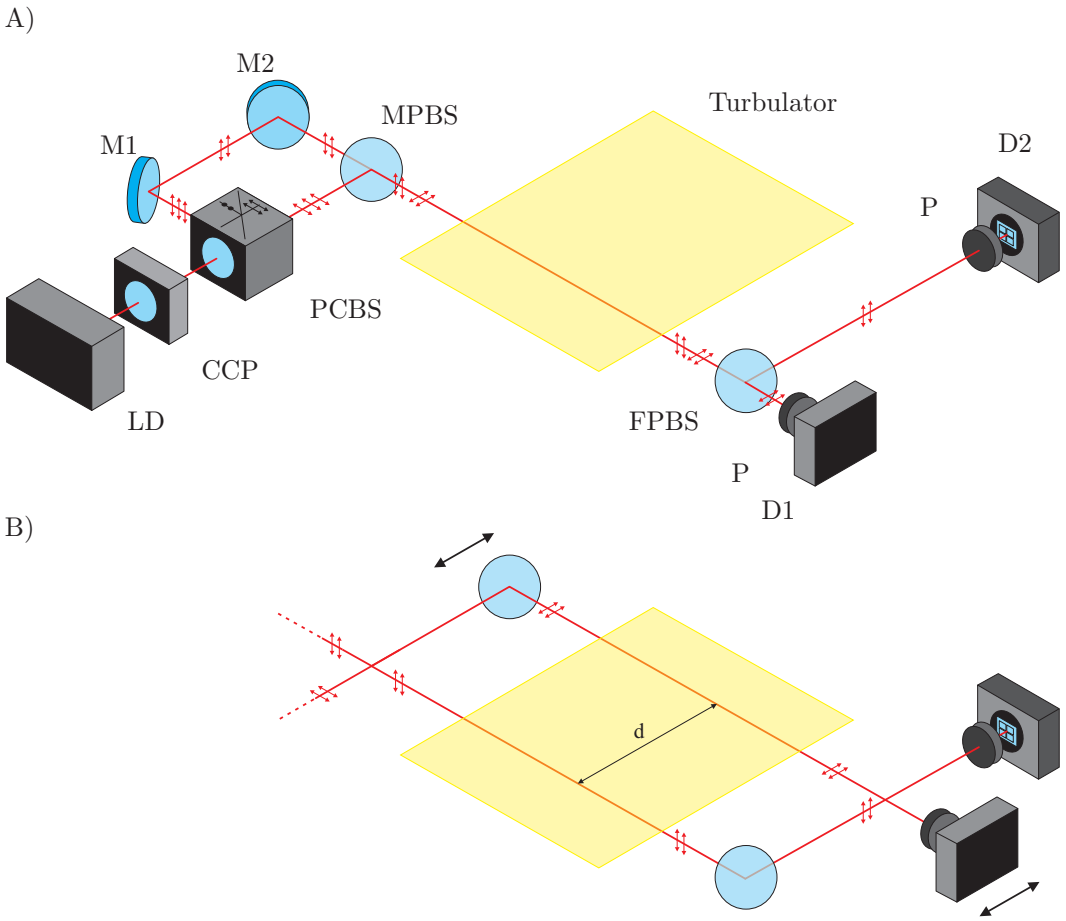

Figure 2.7: The emitter platform produces two cross polarised beams running parallel to each other as they pass through the turbulator. The laser diode (LD) beam is collimated and pass trough a $\lambda/4$-wave plate (CCP) then the thin beam is split in two cross-polarised beams: a beam reflecting in two mirrors (M1 and M2), and a second on a movable pellicle beam splitter (MPBS). These two thin beams emerge parallel to each other. A) for small distances the fixed pellicle beam splitter allow detection of wandering for small separations of position detectors D1 and D2, the polarisers (P) forbid position detection mixing. B) for separations over 20 mm both detectors receive direct light from the emitter platform.

Finally, we have had to place the platforms over tripods. Henceforth, we designed two mounts in AutoCad which were molded in Argentina by a milling machine. The platforms look like in photos 2.8 and 2.9.

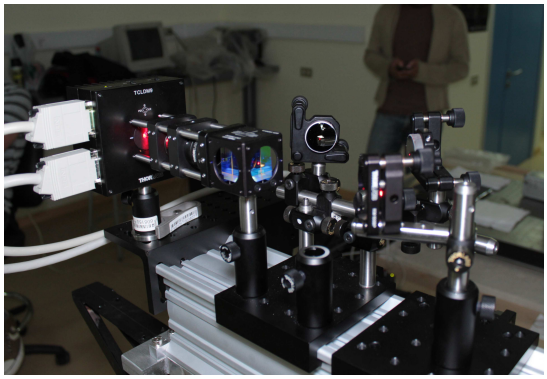

Figure 2.8: Emitter platform.

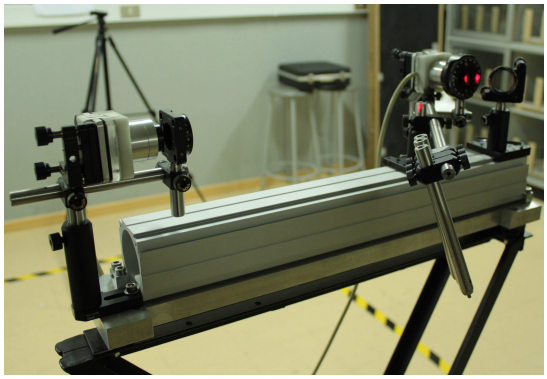

Figure 2.9: Receptor platform.

The experimental measurements were performed in controlled conditions: the turbulent media was created by the turbulator—see Sec. 2.1.1.

For the experiment we chose the following set of 25 distances: $0, 1, 2, 3, 4, 5, 6, 7, 8, 18, 19, 20, 21, 22, 23, 24, 25, 30, 40, 50, 60, 70, 80, 90,$ and 100 millimetres. The total propagation distance for the twin-beam is 1.29 m, but only 0.37 m are inside the turbulent medium, thus the factor from the inactive air is $p \simeq 0.71$.

Both detectors were interfaced to a computer which allowed an acquisition rate of 6000 samples per second. Twenty five consecutive records of 60000 pairs of centroid laser beam coordinates, a total of 300,000 data, were obtained for each separation distance between the two beams—each record was acquired in ~ 50 s. The four coordinates were stored in a hard disk, and the statistical analysis was performed afterwards.

Eight identical experiments were made at different turbulence strength, changing temperature differential between the hot and cold air fluxes: 2.930×10^{-9}(@40°C), 4.830×10^{-9}(@80°C), 5.780×10^{-9}(@100°C), 6.731×10^{-9}(@120°C), 7.206×10^{-9}(@130°C), 7.681×10^{-9}(@140°C), 8.156×10^{-9}(@150°C) and 8.631×10^{-9}(@160°C)$\mathrm{m}^{-2/3}$. For each intensity we collected the beam wandering data for each designated separation. Additionally, we have performed complete acquisitions for each separation studied with the hot source is off; thus, both mass of air just collide generating turbulence where the perturbations to the refractive index are negligible. They can be considered as background measurements that quantify the mechanical, electronic, and other noises produced by this particular experimental arrangement.

The final setup is presented at the picture below 2.10.

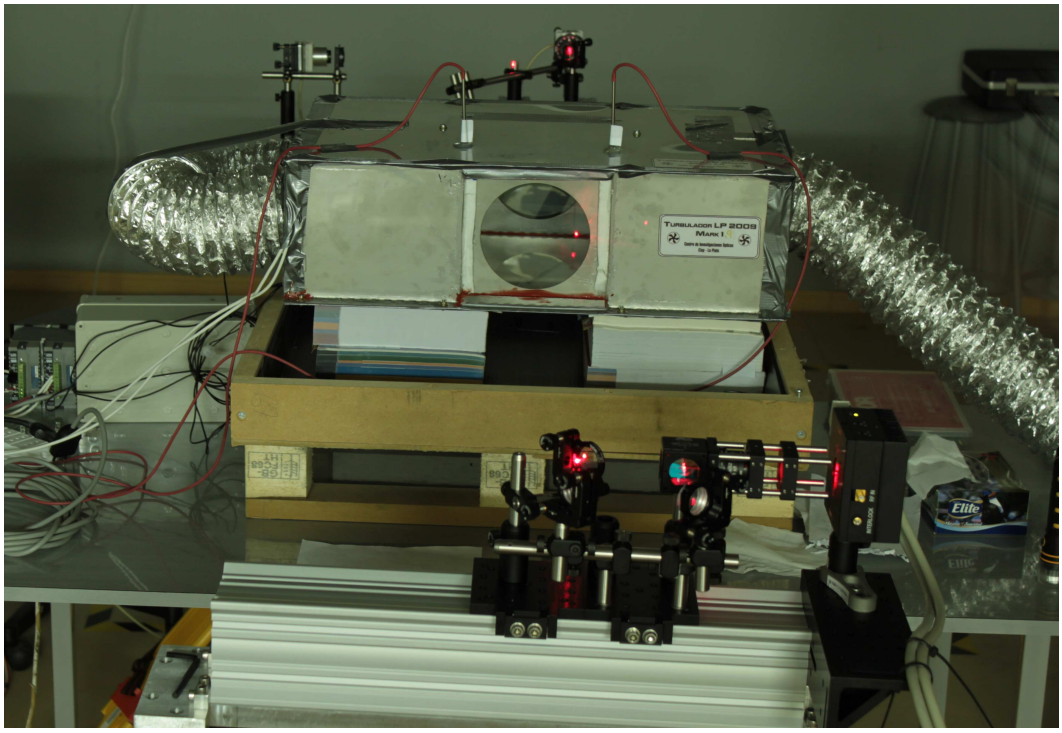

Figure 2.10: Optical configuration for twin beam propagation.

2.1.3 Twin beam covariance for generalized spectra for partially filled paths

The model of Consortini and O'Donnell (1991, 1993) is devised to study thin beams propagating in turbulence along large paths. This approximation is not suited to analyse the small distances usually found in the laboratory. Moreover, it is unable to model deviations from the OK theory. Our extension of their work is capable of handling the situations we have found in our experiment. First note, that on- and off-plane covariances can be reduced to adimensional forms separating the effects of the different scales from the geometric constrains of the problem. Therefore, under the non-Kolmogorov von Kármán (nKvK) model, the on- and off-plane covariance for two beams propagating (partially) across a turbulent region—see Fig. 2.11

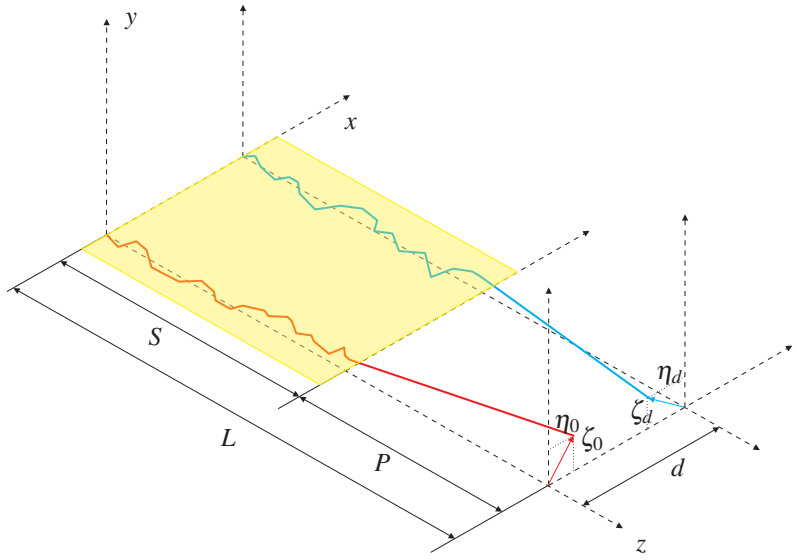

Figure 2.11: Twin beam sketch. Two parallels thin beams propagating in a turbulent media. The turbulent region is confined to the zone of length S, after that the beams propagate in a region of length P without being deflected. Originally, the beams are separated a distance d, and the arrival position with respect to the original trajectory is given by (η_0, ζ_0) and (η_d, ζ_d). Figure from Pérez and Funes (2012).

and results Pérez and Funes (2012),

$$B_x(d) = \langle \eta_d \eta_0 \rangle = \\ = L_m^{5/2} \left[\int_0^1 \tilde{g}_n(u,\delta) \left(\frac{2}{3} - u + \frac{u^3}{3} \right) du - p^2 \int_0^1 \tilde{g}_n(u,\delta) \left(u + \frac{2}{3}p \right) du \right], \tag{2.2}$$

with $p = P/L$ the fraction of inactive turbulence (taking a region of length P) in the propagation path of length L, $L_m = \kappa_m L$ represents the *adimensional propagation distance*, a function of $\kappa_m = 2\pi/\ell_0$ the inner-scale cut-off, and

$$\tilde{g}_n(u,\delta) = \frac{\sin(\pi H)\Gamma(2H+2)}{\pi \kappa_m^{2H+2}} C_n^2 \int_0^\infty \frac{k \exp(-k^2)}{(q^2+k^2)^{H+3/2}} \left[\frac{k^{3/2} J_{3/2}\left(kL_m\sqrt{u^2+\delta^2}\right)}{(u^2+\delta^2)^{3/4}} \right] dk \tag{2.3}$$

where $\delta = d/L$ is the separation between beams relative to the propagation distance, the *relative separation*. Observe that the second term in Eq. (2.2) can be thought as a correcting term function of p; moreover, when p is small its contribution to the

covariance is negligible. On the other hand, the on-plane covariance is functionally dependent of $\tilde{g}_n$, so it can be defined from Eq. (2.2) and the *covariance difference*

$$\begin{aligned}\Delta(d) &= B_x(d) - B_y(d) = \\ &= \delta^2 L_m^{7/2}\left[\int_0^1 \tilde{h}_n(u,\delta)\left(\frac{2}{3} - u + \frac{u^3}{3}\right)du - p^2\int_0^1 \tilde{h}_n(u,\delta)\left(u + \frac{2}{3}p\right)du\right],\end{aligned} \tag{2.4}$$

with

$$\tilde{h}_n(u,\delta) = \frac{\sin(\pi H)\Gamma(2H+2)}{\pi\kappa_m^{2H+2}}C_n^2\int_0^\infty \frac{k\exp\left(-k^2\right)}{\left(q^2+k^2\right)^{H+3/2}}\left[\frac{k^{5/2}J_{5/2}\left(kL_m\sqrt{u^2+\delta^2}\right)}{\left(u^2+\delta^2\right)^{5/4}}\right]dk. \tag{2.5}$$

In both definitions, $\tilde{g}_n$ and $\tilde{h}_n$, are obtained from the adimensional form of the non-Kolmogorov von Kármán spectrum—see Eq. (1.22) at Sec. 1.2, the *scale ratio* $q = \ell_0/L_0$ controls the size of the inertial range, and the Hurst parameter H establishes the degree of development of the turbulence, while C_n^2 quantifies the strength of the turbulence—beware that the structure constant must have dimensions compatible with the power spectrum of the inertial range. These covariances are analytically intractable for propagation distances comparable with the beam separation; that is, $\delta = d/L \ll 1$ for the conditions given in Consortini and O'Donnell (1991) be valid regardless of the value of L_m and q. Pérez and Funes (2012) have presented a detailed treatment of this property. In particular, they have found that separation for which the maximum of $\Delta(d)$ is reached behaves as

$$d = p(H)\frac{\ell_0}{\cosh\left[m(H)\left(\frac{\ell_0}{L_0}\right)^{c(H)}\right]}, \tag{2.6}$$

where

$$\begin{aligned} p(H) &= 7.645(\pm 3.664)H^2 + 1.907(\pm 0.921)H + 3.470(\pm 0.045), \\ c(H) &= -0.5989(\pm 0.599)H^2 - 0.3902(\pm 0.376)H + 0.6082(\pm 0.029), \\ m(H) &= 1.39(\pm 1.000)H^2 + 0.765(\pm 0.361)H + 1.023(\pm 0.026); \end{aligned}$$

the changes in H accounts up to 25% in the determination of the inner-scale from the

position of the maxima, for small values of q. Therefore, it is required some previous knowledge of the scale-ratio (q) and Hurst exponent (H) for the determination of the inner-scale from Eq. (2.6). On the other hand, the axis cut-off provides a more complex relation: even the for the smallest values of variation on scale-ratio gives very different, and non-linear, functions of L_m. Therefore, the axis-cut should be excluded as a valid method for estimating the outer-scale.

2.1.4 The stochastic nature of the turbulent refractive index fluctuations

Scale invariance and self-similarity for time series can be associated with a single type of structure characterized by a single exponent, H, or by composition of several sub-structures with certain local exponent, h. The former is called mono-fractal and the latter multi-fractal. The statistical characteristics (correlations for instance) of these series are dominated by these local exponents, being the first a special case of the latter. In recent years, a widely adopted method used for the determination of the fractal scaling properties and detection of long-range correlations in noisy and non-stationary time series is the *multifractal detrended fluctuation analysis* (MFDFA)—It is a highly robust and easy to implement technique. The local exponent is a continuous function of the order s which is associated, roughly speaking, to the size of the fluctuations in the original series. The value h at $s = 2$ is equal to the well-known Hurst exponent in the case of stationary series. If the local exponent remains constant then we are observing a mono-fractal; that is, all the scales have the same (statistical) self-similarity law.

Under the assumption that the refractive index perturbations due to the turbulence are Gaussian. Using the classical definition given to wave-front phase, in weak regime, it can be shown that index perturbations from a partially developed turbulence with Hurst exponent H produce phase fluctuations with exponent equal to $H + \frac{1}{2}$—5/6 for the Kolmogorov case. This is the expected exponent controlling the time-series obtained in each coordinate axis.

2.1.5 Analysis of the measurements

After the data recollection the on- and off-plane covariances can be evaluated; nevertheless, without preparation, effects due either to electronic or mechanical noise notably affect the results. As observed in Fig. 2.12, the covariances and their difference, $\Delta(d)$, although similar to the theoretical curves, present unexpected behaviours: at the origin $d = 0$ on- and off-plane covariances should match, there is a mismatch not attributable to experimental error; then, for distances above 30 mm the asymptotic trend to zero is notably slowed.

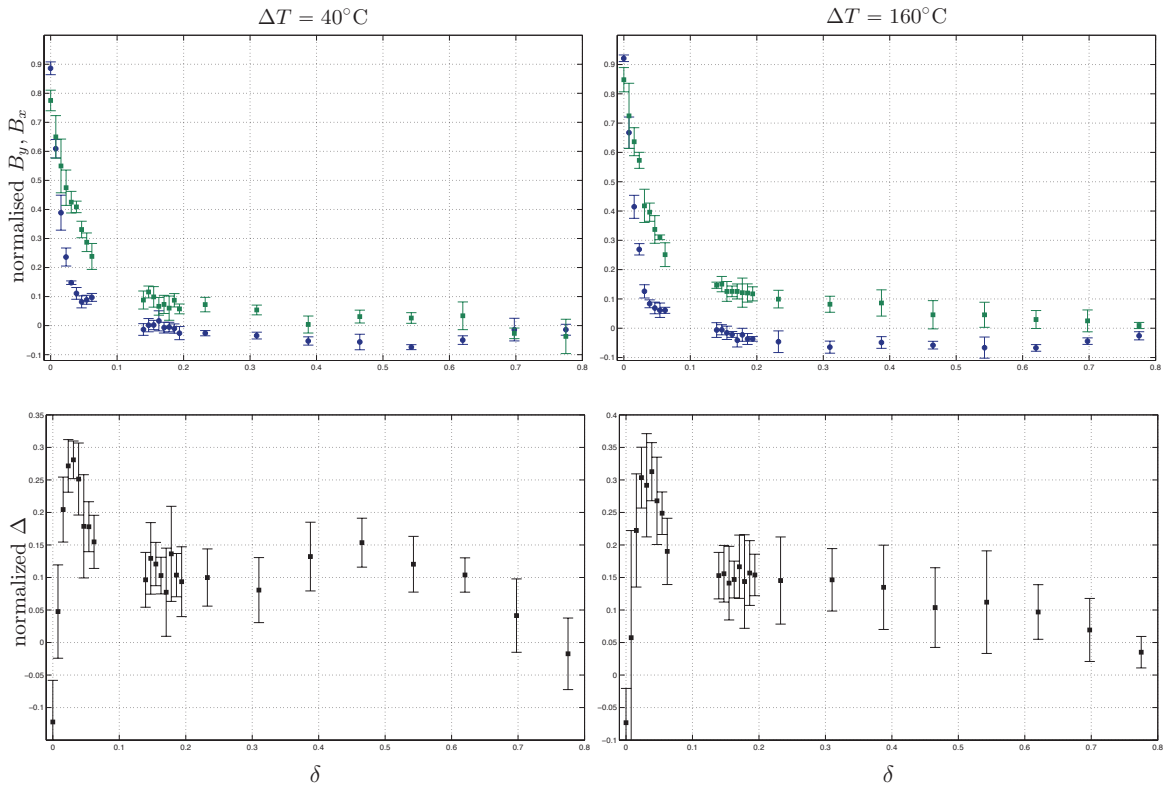

Figure 2.12: Unfiltered covariances: (Top) the normalised on- (■) and off-plane (●) covariances are displayed for the weakest and stronger turbulence available. (Bottom) the covariance difference produced by unfiltered data, the deviations from the theoretical model are so strong that fits are unsatisfactory—particularly, for temperature differences above 100°C.

Fitting these data is possible, but huge inconsistencies between the fits for each covariance function at a given temperature are found—the parameters L_m and q are

quite different in each variance fit. Regardless of the mechanical quality of the setup, we have confirmed through wavelet analysis that some energy levels (in the wavelet decomposition—see (Mallat, 2009)) are spurious contributions unrelated to the turbulence dynamics.

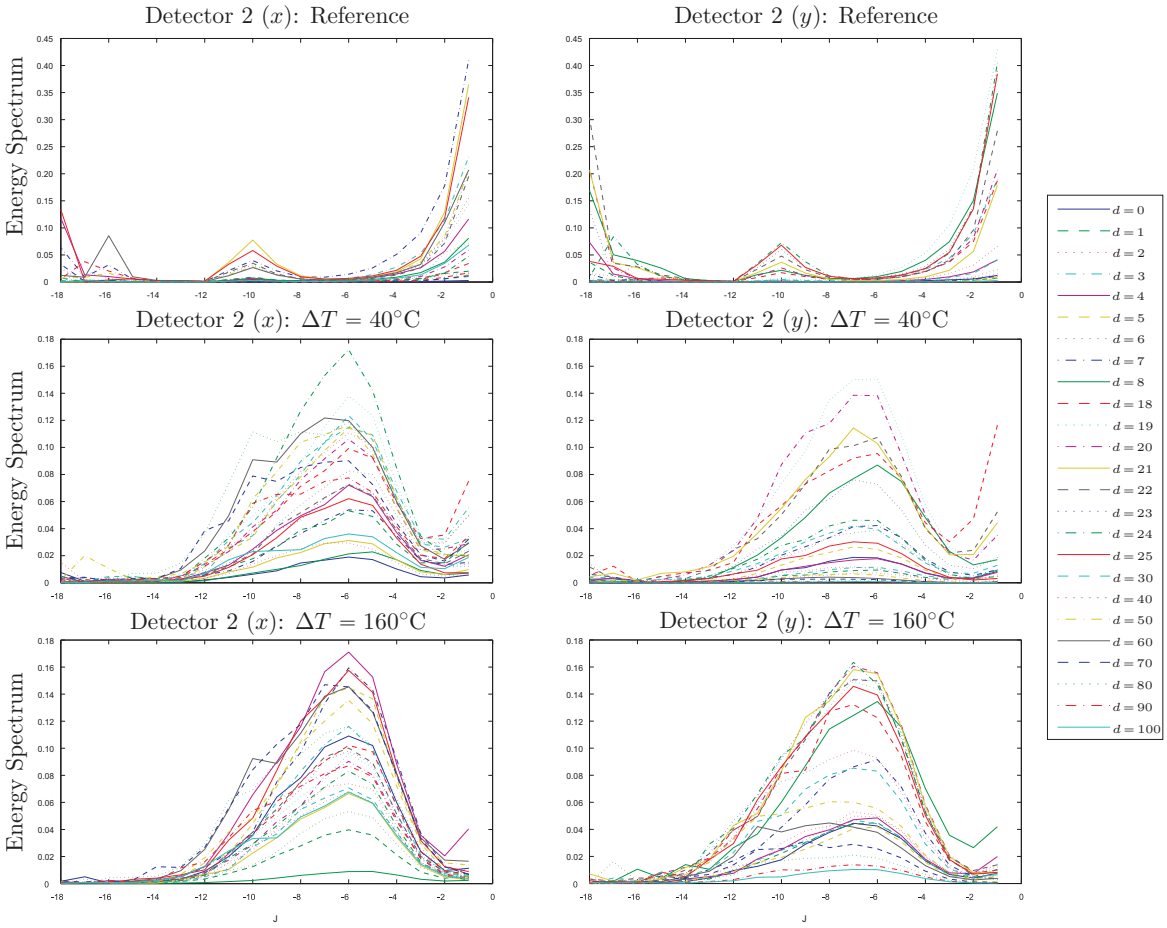

Figure 2.13: (Top) the noise observed in the energy levels of the wavelet decomposition in the second detector when the hot source is off. (Middle) energy spectrum for the weakest turbulence in our experiment; the effects of turbulence in the signal are clearly distinguished. (Bottom) as for the weakest turbulence, the strongest analysed presents the same characteristic energy spectrum. The noise is present in all the spectra in the lowest and highest energy levels.

In Fig. 2.13 (Top), we observe the noise of the system in the detected wandering generated by the turbulator when no optical turbulence is generated. For all the turbulence strength levels a consistent signature is found in level range $(-14, -4)$:

this is obviously product of the optical turbulence, see Fig. 2.13 (Middle, Bottom). Therefore, the signal is reconstructed from the energy levels in this range; therefore, cutting out the contributions from the system noises.

As Fig. 2.14 shows, the value at the origin for both covariances is exactly the same; originally attributed to some anisotropic phenomena, the mismatch was a product of noise and nonlinearities of the original setup. Nevertheless, the fat-tails fail to be corrected by this approach. Above 30 mm there is a slower decay that is not produced by the experiment setup, thus it is an effect of this specific turbulence.

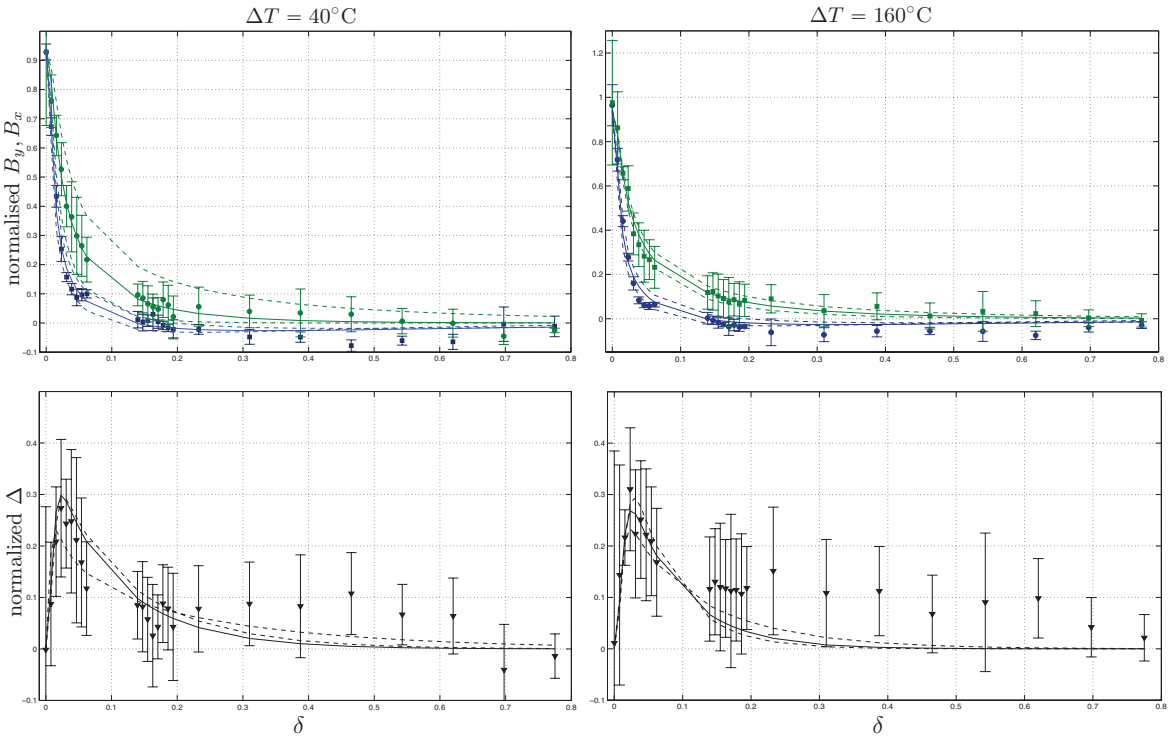

Figure 2.14: Filtered covariances: (Top) the normalised on-(■) and off-plane (●) covariances are displayed for the weakest and stronger turbulence available; the solid lines correspond to the best fit, with dashed lines the the 95% prediction bounds are shown. (Bottom) the covariance difference (▼) produced by filtered data, the fits from theoretical model are satisfactory for any value of C_n^2, excluding the tails.

To understand the peculiarities found in the classical analysis more powerful tools are needed. To this effect, we analyse the series produced by the DLTMM experiment with MFDFA3 as follows: we produce two differential time series from the detectors original pair, $x_t(0) - x_t(d)$ and $y_t(0) - y_t(d)$, and split them in 10 series of $30,000$

data-points each in order to obtain a mean value of the Hurst exponent, $h(2) = H$ (with error given by its standard deviation). The detrending algorithm employed in the estimation of H uses a polynomial of degree 3, thus the acronym MFDFA3. The fitting range for the exponent estimation was carefully chosen studying the fluctuation functions and their log-log derivative.

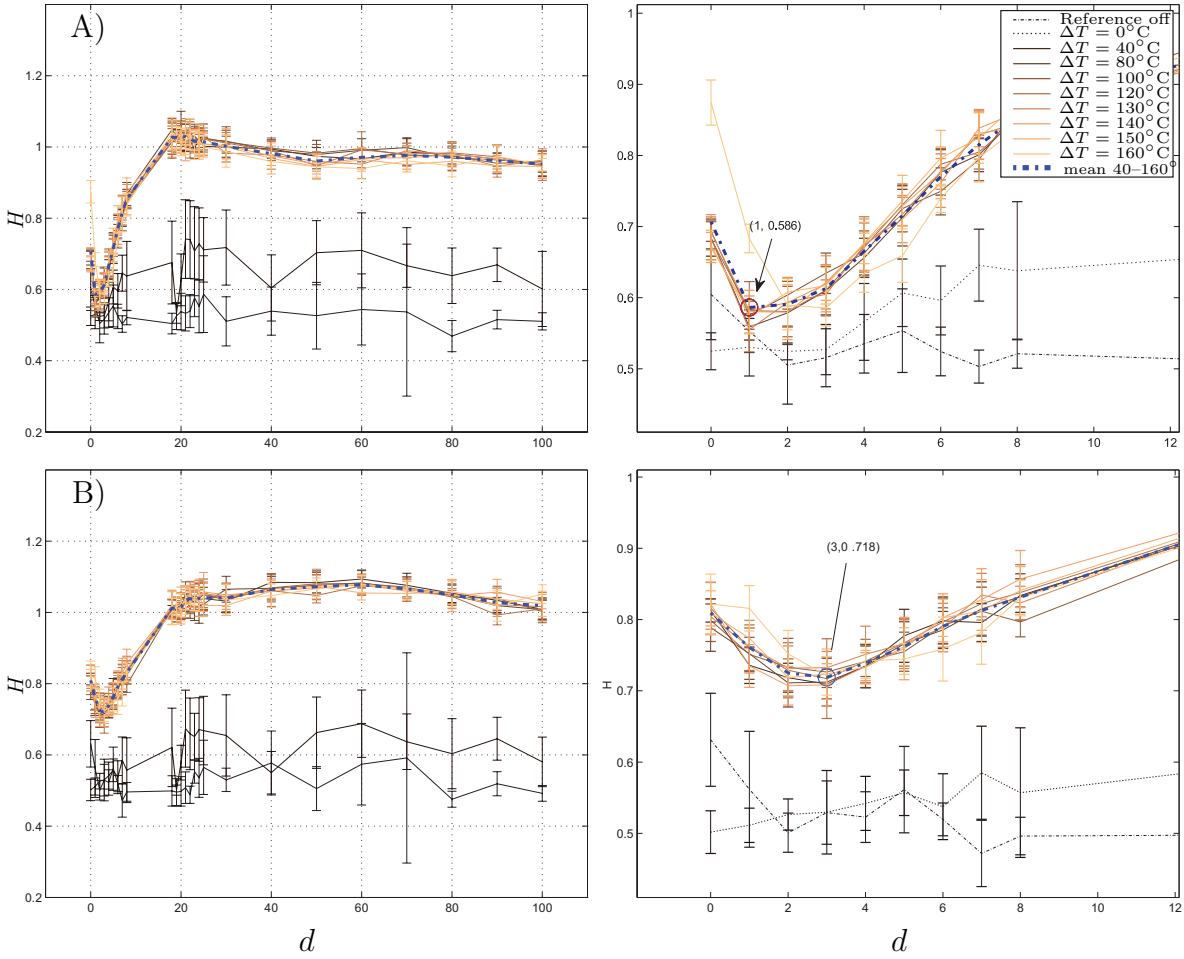

Figure 2.15: A) Hurst exponent as a function of the difference d for the on-plane wandering series; the left image portrays the whole range, on the right the zoomed region where inflection occurs. B) Hurst exponent as a function of the difference d for the off-plane wandering series; the left image portrays the whole range, on the right the zoomed region where inflection occurs. Observe that both references have H values near 1/2.

Fig. 2.15 shows the results of this procedure. For every given ΔT (associated with a unique C_n^2), the Hurst exponent reveals a function of the beam separation. In both axis

we observe values around 0.5 (brownian motion) for references; this is the noise of the system dynamics. For all the temperature differences studied (greater than zero) the behaviour is exactly the same. Long-range correlations appear to occur for ~ 20 mm and above, and with the given error bars one could guess this is the same phenomena observed for different temperatures. Moreover, values for the off-plane axis are slightly greater than those for on-plane axis indicating anisotropies (known to exist) in the turbulator.

Now, the saturation of the Hurst exponent is a phenomenon of the distance: the average curve starts at 0.7, and reaches a minimum (around the 3 mm, see Fig. 2.15 left), then an inflection point occurs that leads to a saturation in H. We associate this change in convexity to the occurrence of a change in the dynamics of the optical turbulence. Under this method the determination of the inflection point should be related to the inner-scale. We proceed by fitting the averaged exponent with a rational functions (R-square 0.98)—see Fig. 2.16, and estimate the inflection distance. From this we obtain $\ell_0 = 0.620 \pm 0.046$ cm for the on-plane wandering series, and $\ell_0 = 0.459 \pm 0.026$ cm for the off-plane series. Notoriously, the on plane scale is the closest to the previously estimated inner-scale.

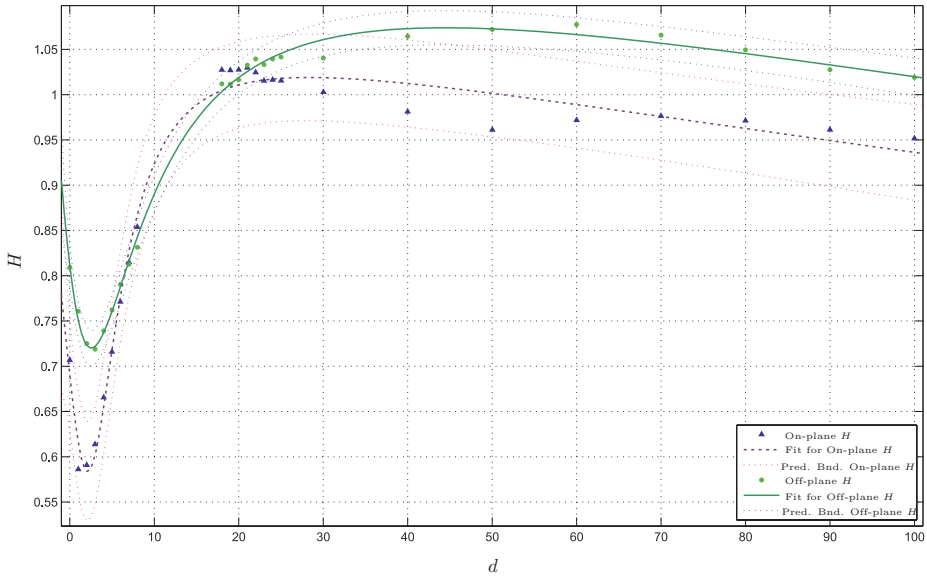

Figure 2.16: Fits for the averaged Hurst exponents estimated for each turbulence strength are displayed. The anisotropy is clearly observed, and the inflection points can be estimated.

Each of the eight turbulent strengths present similar values for the adimensional propagation distance and the scale-ratio, see Table 2.1, but due to the tails huge uncertainties are observed. Moreover, as discussed in Pérez and Funes (2012) the free-space propagation should be relevant, but for the on- and off-plane covariances fits a good fit was only obtained for $p \simeq 0.35$ instead of 0.71, an important deviation from the experimental fraction. On the other hand, the maxima method proposed originally by Consortini and O'Donnell (1991) is quite stable under any circumstance. In this case, good fits for the covariance difference are found for p around 0.71. The inner-scale is determined from Eq. (2.6) for the maxima given by the best fit, $\ell_0 = 0.69 \pm 0.04$ cm. Also, the outer-scale can be estimated from these fits, and results $L_0 = 13.21 \pm 2.36$ cm; this is to be expected since the width of the camera where the turbulent mixing occurs is 17 cm.

		ΔT			
		40°C	80°C	100°C	120°C
B_y	L_m	267.9 ± 44.1	214 ± 57.7	229.5 ± 36.2	202.1 ± 22.4
	q	0.0067 ± 0.0037	0.0115 ± 0.0090	0.0109 ± 0.0045	0.0173 ± 0.0079
B_x	L_m	280.3 ± 93.2	251.8 ± 34.2	246.3 ± 24.3	270.4 ± 11.2
	q	0.0212 ± 0.0173	0.0206 ± 0.0080	0.0210 ± 0.0065	0.0154 ± 0.0037
		130°C	140°C	150°C	160°C
B_y	L_m	206.1 ± 30.6	233.5 ± 42.7	247.3 ± 58.1	224.5 ± 34.8
	q	0.0153 ± 0.0085	0.0104 ± 0.0064	0.0100 ± 0.0073	0.0154 ± 0.0054
B_x	L_m	249 ± 17.9	261.4 ± 21.1	267.1 ± 28.7	279.5 ± 22.8
	q	0.0170 ± 0.0053	0.0156 ± 0.0046	0.0119 ± 0.0046	0.0120 ± 0.0048

Table 2.1: Best Fit adimensional parameters for different values of C_n^2.

2.2 Optimal sampling rate for laser beams propagation through atmospheric turbulence

Fig. 2.13 shows the band where the turbulence is active, which is different from the band where the noise is located. That figure pushed us to investigate a new procedure.

Sampling rate and frequency content determinations for optical quantities related to light propagation through turbulence are still unsettled experimental problems. Many

works about estimating properties of the optical turbulence seem to use some *ad hoc* assumptions to set the sampling frequency used; without further analysis, this chosen sampling rate is assumed good enough to perform a proper measurement. On the other hand, other authors estimate the optimal sampling rate via Fourier transform of the data series associated to the experiment, specifically the fast Fourier transform algorithm (FFT), defining a cut-off frequency with an arbitrary criterion—that may be related to an underlying model. However, these theoretical developments require the exact knowledge of the turbulence properties, which is unreachable experimentally. For instance, to obtaining the variance of angle-of-arrival and the aperture diameter, the inner-scale knowledge is required. In this way, one measurement supports the other one. The aim of this section is to propose an alternative, and practical, method to estimate a proper sampling rate. By means of the discrete wavelet transform, this approach can prevent any loss of information and, at the same time, avoid oversampling. Moreover, it is independent of the statistical model imposed on the turbulence.

Frequency content of fluctuations of lightwave parameters in turbulent media was first determined by Tatarskĭ (1967). By using the *frozen turbulence hypothesis* and the Obukhov-Kolmogorov (OK) model, he showed that the phase and amplitude frequency spectra of a wave propagating through turbulent media span up to a frequency that linearly depends on the mean transverse flow velocity. According to (Andrews and Phillips, 1998)—see Sec. 1.3, the previous result is valid within the weak turbulence regime, i.e., when the Rytov variance is much less than one, $\sigma_R^2 \ll 1$.

As the Nyquist-Shannon sampling theorem asserts, sampling rate is directly related to the frequency content; therefore, any experiment should warrant that all the relevant frequencies of the observed quantities are included for the chosen sampling rate. In the last decades several authors have performed experiments to measure fluctuations in lightwave parameters, but the choice of a specified sampling rate—f_s, is rarely clear or directly specified. Usually, its choice is unjustified, or there are technical limitations precluding its selection (sampling frequency limits on the measurement device, interface, lack of computing power, etc.). Ultimately, the frequency content due to the optical turbulence depends on the experimental arrangement, thus its determination is subject to measurement aspects. Some authors have estimated, through the fast Fourier transform (FFT), that the spectral range of turbulence extends from 20 to 200Hz. These values are directly related to the turbulent quantity under study, and,

consequently, they can not be employed in other experiments.

Wavelet analysis was first introduced in seismology to provide a temporal scale to seismic data, since Fourier analysis was unable to cope with transient events (Mallat, 2009). Wavelets were used ever since in various fields with very good performance for non-stationary signal analysis and processing. Fourier transform decomposes signals through plane waves, thus it is specially suited for periodic or non-localized stationary data. As turbulent data seem to be composed of coherent structures with a well-defined scale hierarchy, wavelets naturally become more appropriate to study it. The wavelet transform allows the analysis of intermittent behaviour commonly present in turbulent signals. This is possible since it yields scale-time information, while the Fourier transform is only able to show the frequency content of the signal.

The *discrete wavelet transform* (DWT, or Mallat Algorithm) decomposes a signal into low- and high-frequency components by convolution with low- and high-pass filters, respectively, generated from a special function of compact support, *mother wavelet*, and its dilations—see Mallat (2009). The global features of the signal are kept by low-frequency components, *approximation coefficients*, whereas the local features are retained by the high-frequency ones, *detail coefficients*. The DWT is a versatile tool for extracting features and information from any given signal. For instance, the detail coefficients can be examined by bands to detect transient events, and specific denoising algorithms can be applied to eliminate spurious noise. Also, the DWT can be particularly useful in estimating the normalized energy content per frequency bands.

A wavelet decomposition requires of a *mother wavelet* function fulfilling the following properties:

$$\int_{-\infty}^{\infty} \psi(u)du = 0, \tag{2.7}$$

$$\int_{-\infty}^{\infty} \psi(u)^2 du = 1, \tag{2.8}$$

Through dilations and translations it is possible to generate an orthonormal basis of $\mathbf{L}^2(\mathbb{R})$:

$$\left\{ \psi_{j,n}(u) = \frac{1}{\sqrt{2^j}} \psi\left(\frac{u - 2^j n}{2^j} \right) \right\}_{(j,n)\in\mathbb{Z}^2} \tag{2.9}$$

This orthonormal wavelet bases, carry characteristic of the signal with a resolution of

2^{-j}. From here arises the multiresolution analysis.

This last application provides a fast and practical estimation of the optimal sampling rate: henceforth called *wavelet energy spectrum* (WES)—see Funes et al. (2013). The scale band frequency employed in the wavelet decomposition for the WES is defined by a dyadic scaling of the sampling rate—see Eq. (2.9), $2^J f_s$, where J goes from $J_{\min}$ to -1, with $J_{\min}$ determined by the length of the signal to be analysed. In general, each band is composed of frequencies from $2^{(J-1)} f_s$ to $2^J f_s$—for example, the $J = -1$ band contains frequencies from $2^{-2} f_s$ to $2^{-1} f_s$. The WES is obtained by evaluating

$$E_J = \frac{\sum_k C_J(k)^2}{\sum_{J,k} C_J(k)^2}, \tag{2.10}$$

with $C_J(k)$ the detail coefficients, and k is the sampling time index. The detail coefficients can be obtained from the energy conservation condition for the DWT, thus

$$\|S\|^2 = \|W\|^2 = \sum_{J,k} C_J(k)^2. \tag{2.11}$$

where S is the column vector and it represents the signal, W is the matrix for the wavelet transform and it is written as

$$W = \widetilde{W} \otimes S. \tag{2.12}$$

with $\widetilde{W}$ as the matrix which contains the dilations and translations of the mother wavelet.

The *power spectral density* (PSD) is the Fourier analogue to the WES. Usually, the determination of the sampling rate through the PSD is bound to an arbitrary criterion, i.e.: locating the frequency at which 90% of the power is contained, and then estimating the sampling rate as twice this frequency (Nyquist). Alternatively, the inverse of the cross-temporal correlation's half-life time can provide another estimate. Although arbitrary, these criteria are still very powerful tools. Unfortunately, they are only valid for stationary series. The optical turbulence (like many natural phenomena) is prominently non-stationary; therefore, a criterion based on the wavelet energy spectrum should be more robust. Naturally, it presents a significant fraction of energy located in those bands where the turbulent phenomenon is more active. We particularly argue

that if the energy of the highest band (E_{-1}) is quite different from zero, some activity may be missing—the spectrum may appear slashed. That is, there are unaccounted for features at higher frequencies disregarded by the actual sampling rate: the recorded data is undersampled.

2.2.1 Experimental configuration

To demonstrate this procedure we have performed a conceptually simple experiment of laser propagation through turbulent media at different sampling rates (0.8, 2, 6, and 12 kHz). Basically, it consists in the propagation of a Gaussian thin beam (635nm, and $1/e^2$ beam diameter of 3mm) through artificial turbulence. The beam propagates through the optical setup described at Sec. 2.1.2—see Fig. 2.2 and picture 2.10.

The experience is dynamic. The first 20 seconds consist of keeping the hot air flow at room temperature. Afterwards, the temperature difference between the two fluxes is increased. When reached the highest temperature possible, the cooling process is achieved by lowering the temperature at the hot flow. A continuous measurement of seven and a half minutes is obtained. Although, temperature differences up to 150°C are achieved, the turbulence is weak, with $\sigma_R^2 = 0.02$ and structure constant $C_n^2 = 6 \times 10^{-10}$ m$^{-2/3}$ at its highest point ($\sigma_R^2 = 0.003$ and $C_n^2 = 9 \times 10^{-11}$ m$^{-2/3}$ at the end)—see Fig. 2.17. Air flow velocity is fixed so the turbulence characteristics are only due to the temperature difference.

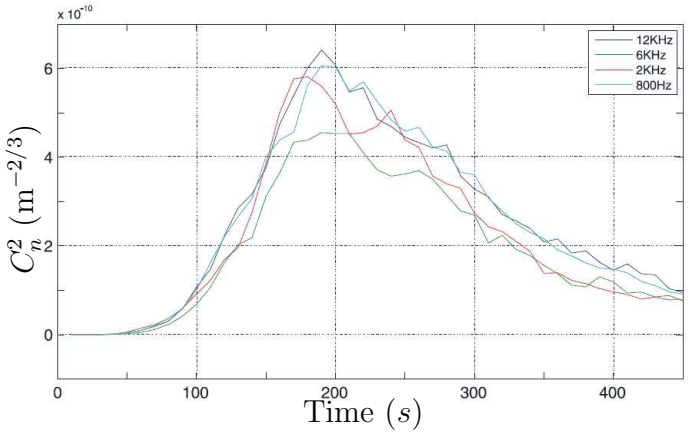

Figure 2.17: Values of the structure parameter during the experiment. This figure features a fast heating and a slow cooling due to the thermal inertia. Graph from Funes (2014).

2.2.2 Analysis

In order to analyse the recorded data we use the DWT algorithm with a Haar basis, this is the simplest mother wavelet. It is very well localized in time, but poorly in frequency, thus making it well suited to detect sudden changes. Computationally, it has been proven to be fast when examining large amount of data. Because of the disadvantage of the Haar basis, we have also estimated the WES with other wavelet basis for some reference data series and found no major discrepancies. Therefore, the use of more complex mother wavelets is unjustified for our purposes. The wavelet spectrum for different sampling rates for horizontal displacements can be observed in Fig. 2.18—the vertical displacements behave alike and would not be shown here.

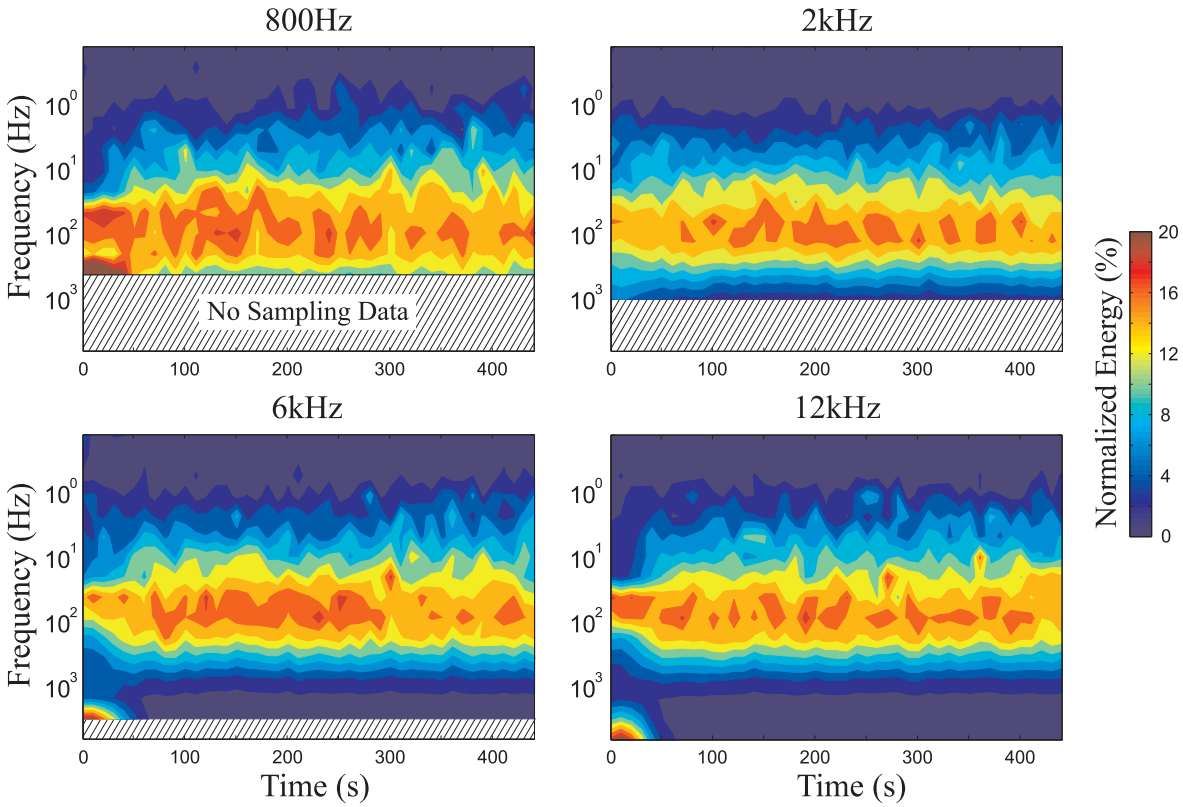

Figure 2.18: WES for the horizontal displacements for different sampling rates showing the temporal evolution.

At the beginning of the experiment the WES shows a maximum of energy around the highest frequency band; this is related to spurious noise caused by the detector.

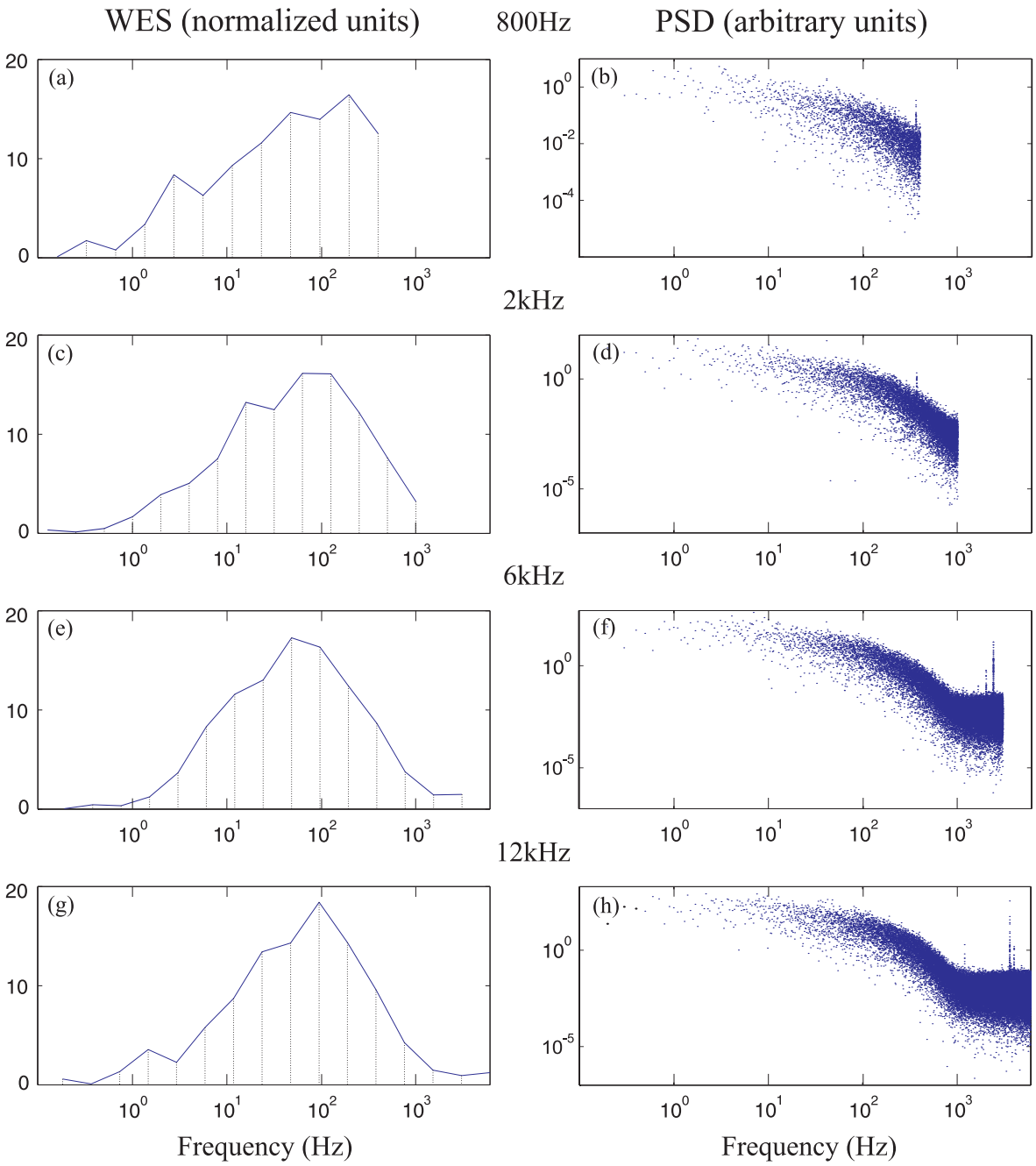

Figure 2.19: a) WES and b) PSD at a sampling rate of 800Hz, c) and d) idem for 2kHz, e) and f) idem for 6kHz, g) and h) idem for 12kHz. The frequencies were delimited for the WES. The time index is 80s.

As the experiment progresses the frequency content related to the turbulence becomes predominant; signal to noise ratio increases, and this peak vanishes. The energy distribution per frequency remains unchanged: the bell-shaped WES is centered around the same frequency bands. This is in good agreement with theoretical results since the flow velocity is fixed (Tatarskĭ, 1967; Andrews and Phillips, 1998).

Fig. 2.19 shows the comparison between the estimated WES and PSD for the same data series at a given sampling rate, again for horizontal displacements, at time index around 80s. The very first two wavelet spectra obtained (at 0.8 and 2kHz) present considerable contribution to the energy at the highest frequency band: there is missing information from the turbulence under study. Although for the second in a lesser extent, both sampling rates can be considered as improper since the original signal is undersampled, and our aim is to have a complete view of the frequency spectrum. On the other hand, the measurements performed at 6 and 12kHz clearly provide full information of the horizontal wandering. Therefore, a lower bound for the sampling frequency should be around 3kHz. A higher sampling frequency is unnecessary since it would carry no new information about the turbulence, thus we are avoiding oversampling. Finally, as the sampling rate increases, the PSD (Fig. 2.19, left column) reveals the occurrence of a knee around 1kHz. It is unclear if the turbulence ceased to be active or the signal-to-noise ratio is too high. Either way, what naturally appears in the WES would require a deeper inspection of the PSD—if a theoretical model is unavailable, it could be unfathomable.

2.3 Conclusions

In this chapter we have carried out two experiments based in the same optical configuration. In the first one, we have presented a thorough exposition of the Geometrical Optics approach for non-Kolmogorov turbulence. It presents some drawbacks to note, from the theoretical point of view it is model dependent, and the exact value of H is unknown. The experimental approach is more challenging, electronic and mechanical noise certainly affects the correlations. Moreover, anisotropies and inhomogeneities are observed with larger separations, such anisotropies are not caused by the experimental arrangement. Although this is inherent to the turbulent nature of the fluid dynamics inside the turbulator, real turbulence should commonly presents such anomalies.

Therefore, additional information should be recollected to solve some of these issues, such as scintillation measurements. In order to have a more suitable interpretation of these results the GO model must be replaced by one based on the physical optics.

Noises present in the system can be greatly mitigated by a wavelet filtering procedure. The signals obtained after filtering are more robust; particularly, the covariance difference can pass the best-fit procedure with R-square above 60%, and inner- and outer- estimated values are in accordance with expected values for this device—the values reported here are similar to those seen in Keskin et al. (2006). Nevertheless, some inconsistencies remain, such as the fat tails observed in both covariances and the high correlation for $d = 0$.

Finally, a new method for estimating the inner-scale is proposed: the determination of the inflection point in the Hurst exponent estimated under the multifractal detrended fluctuation analysis. Not only successfully provides values for the inner-scale, but also provides the first hints to an anisotropic inner-scale in optical turbulence. On the other hand, the exponent H obtained in this way differs from the expected values: once the threshold of the inner-scale has been exceeded the asymptotic values should be near 5/6, as discussed in Sec. 2.1.4. The excess in this value is unaccounted through classical models, or even single scale non-Kolmogorov extensions. Further research on whether this is the product of temporal correlations or the existence of a non-Gaussian statistics should be performed.

The latter experiment, two main considerations should be used to determine an optimal sampling rate from the WES: the bell-shaped energy distribution corresponding to the optical turbulence must be completely visible for a given f_s; and the lowest and highest bands, associated to mechanical and electronic noise, should have a negligible signature in the spectrum—observe the temporal evolution of the WES in Fig. 2.18, for 6 and 12kHz. Under these conditions we can obtain a practical estimation of the optimal sampling rate without losing any information regarding the original dynamics. The advantage of this method is twofold. It permits to isolate noise from signal and be applied indistinctly to both stationary and non-stationary series. Furthermore, this procedure is independent from any theoretical model or *ad hoc* hypotheses regarding the optical turbulence (Funes et al., 2013).

Chapter 3

Thin Laser Beam Wandering and Intensity Fluctuations Method for Evapotranspiration Measurement

Laser beam propagation through a random medium can be applied to many areas, such as free space optical (FSO) communication systems, laser radar, imaging, remote sensing, to name a few. In this chapter we enlarge the scope of applications and we extend us to a new area: "evapotranspiration". The corresponding heat flux values are sensed by the optical wave propagation in its path, which allows us to obtain the vegetation evapotranspiration. Straightforward, we propose a new device to measure the heat fluxes and we compared it with a well-known and calibrated eddy-covariant instrument.

3.1 Evapotranspiration process

In general, evapotranspiration is the sum of evaporation and transpiration and it is defined as the water lost to the atmosphere from the ground surface, evaporation from the capillary fringe of the groundwater table, and the transpiration of groundwater by plants whose roots tap the capillary fringe of the groundwater table. Here we will not include evaporation from surface water.

The transpiration aspect of evapotranspiration is essentially evaporation of water

from plant leaves. Plants put down roots into the soil to draw water and nutrients up into the stems and leaves. Some of this water is returned to the air by transpiration. Transpiration rates vary widely depending on weather conditions, such as temperature, humidity, sunlight availability and intensity, precipitation, soil type and saturation, wind, and land slope. During dry periods, transpiration can contribute to the loss of moisture in the upper soil zone, which can have an effect on vegetation and food-crop fields.

Plant transpiration is pretty much an invisible process, which changes the atmosphere natural conditions. Just because we cannot see the water does not mean it is not being put into the air. One way to visualize transpiration is propagate a beam and to study its fluctuations of intensity.

The amount of water that plants transpire varies greatly geographically and over time. There are a number of factors that determine transpiration rates:

(*i*) *Temperature*: Transpiration rates go up as the temperature goes up, especially during the growing season, when the air is warmer due to stronger sunlight and warmer air masses. Higher temperatures cause the plant cells which control the openings (stoma) where water is released to the atmosphere to open, whereas colder temperatures cause the openings to close.

(*ii*) *Relative humidity*: As the relative humidity of the air surrounding the plant rises the transpiration rate falls. It is easier for water to evaporate into dryer air than into more saturated air.

(*iii*) *Wind and air movement*: Increased movement of the air around a plant will result in a higher transpiration rate. Wind will move the air around, with the result that the more saturated air close to the leaf is replaced by drier air.

(*iv*) *Soil-moisture availability*: When moisture is lacking, plants can begin to senesce (premature ageing, which can result in leaf loss) and transpire less water.

(*v*) *Type of plant*: Plants transpire water at different rates. Some plants which grow in arid regions, such as cacti and succulents, conserve precious water by transpiring less water than other plants.

Evapotranspiration, as well as precipitation, condensation, evaporation, and amount other process, contributing to the global water cycle.

3.2 Introduction to the experiment

Climate change and water demand are increasing over the past years. Water resource management is becoming essential for agriculture. One of the long term solutions lies in understanding how one can improve the efficiency with which water is used to reduce wastage. As water use for agriculture is subject to increasing scrutiny from policy makers and environmentalists, the result is that agriculture is under growing pressure to demonstrate that water is being used efficiently. Numerous methods are available to provide informations on crop water use (or evapotranspiration, ET), crop irrigation requirements, and efficiency with which crops area produced, or water use efficiency. Of these, field level methods (e.g., lysimeters, Eddy covariance, Bowen Ratio, surface renewal, scintillometry, soil water balance) used to estimate (or measure) evapotranspiration (ET) from surfaces have been evaluated extensively in the past.

Thus, crop evapotranspiration knowledge is a precious asset for the evaluation of water losses and for precision irrigation. Several ways to remotely obtain a value of evapotranspiration exist, but only one takes into account the strength of the small fluctuations in the index of refraction due to temperatures fluctuations through the measurement of the refractive index structure of air C_n^2 via an optical metrology with scintillometric measurements of a laser beam. Techniques used to obtain C_n^2 have been reviewed in Sec. 1.6. A newly different method to sense the atmospheric turbulence measures intensity fluctuations after propagation in a turbulent medium patterned on a holographic plate (Barillé et al., 2013).

However if the scintillometer method is well known, the beam wandering method is less used and the holographic method has never been used in surface heat measurements.

3.2.1 Scintillometer

A scintillometer is an instrument that consists of a transmitter and a receiver. The receiver measures intensity fluctuations in the radiation emitted by the transmitter caused by refractive scattering of turbulent eddies in the scintillometer path. Scintillometers exist since the 1970's (Wang et al., 1978), and mostly use large aperture devices (Moene et al., 2004) to measure the refractive index structure parameter C_n^2 with the variance of intensity fluctuation measurements.

Generally, when the measurement of C_n^2 is made over a path in a range > 50 m, intensity fluctuations is used only. Beam wandering measurements with a collimated laser beam leading to values of C_n^2 have been made in laboratory experiments at small scales and in real conditions over longer distances, but never to indirectly measure the surface heat flux to our knowledge.

We propose in this study a scintillometer based on a thin collimated laser beam in the aim to measure values of C_n^2 over a crop field. We show that this scintillometer has several advantages and drawbacks. The obtained values of refractive index structure parameter can then be used to compute the sensible flux and the latent heat flux over the laser beam path when they are coupled to other meteorological data.

We measure in our experiment C_n^2 values using both the intensity fluctuations and the wandering fluctuations of the beam over a long beam propagation path with the developed device. The results obtained with the two methods are compared to data obtained with a micrometeorological method and a 3D sonic anemometer.

3.3 Evapotranspiration by remote sensing

The relation between energy balance, heat flux density and surface temperature is long known and was investigated early (Li et al., 2009; Rana and Katerji, 2000). The theoretical basis of energy fluxes modeling is studied taking the land surface as a flat and thin layer such that no heat storage exist, the surface energy balance equation at the interface between the land surface and the overlying atmosphere is written as:

$$R_n = H + \lambda E + G_0 \tag{3.1}$$

where R_n is the net radiation flux, λE is the latent heat flux—or evaporation when is expressed in term of water depth, H is the sensible heat flux and G_0 is the soil heat flux. The sign convention in Eq. (3.1) is that R_n is considered positive when directed towards the land surface, while H, λE and G_0 are considered positive when directed away from the land surface. For the sake of simplicity, all flux densities will be called fluxes, and the units is W/m^2.

Incoming solar radiation is mainly driven by the azimuth and zenith angle of the sun at a given position and time. However, many other factors have to be taken into

account to reproduce global radiation correctly. In particular, ground elevation and relief determine the direct incoming radiation pattern in mountainous areas, cloud cover can reduce direct radiation, and atmospheric aerosols content will significantly affect the contribution of diffuse radiation to the global radiation. Atmospheric radiation is mainly driven by the atmosphere temperature and column water content (and by extension cloud type and content). The vertical structure and properties of the atmosphere must be known to reproduce the surface radiative fluxes.

The soil heat flux is often parameterized proportionally to the net radiation arriving at the soil surface, therefore is a function of the vegetation cover—see (Faivre, 2014) and references therein.

In the context of applying remote sensing measurements to estimate heat fluxes, the latent heat flux or evaporation is calculated as the residual of energy balance Eq. (3.1), and the major concern is to calculate sensible heat flux H. As in Faivre (2014), H is calculated by two mehtods; the Single-source parameterization and the Dual-source parameterization. In the former, the sensible heat flux is related to the difference between the air temperature at a source height z_0 for heat transfer (so-called the aerodynamic surface temperature, T_{aero}) and air temperature T_a at a reference height. The Dual-source parameterization makes a difference between the surface energy transfer of soil and canopy sub-systems. This model allows to distinguish radiometric and aerodynamic surface temperatures by incorporating the effects of sensor view geometry to partion surface energy and temperature into soil and vegetation sub-components. Here we use the eddy covariance method (Barillé et al., 2016), which belongs to the Single-source parameterization. The method will be described below.

3.3.1 Single-source parameterization of H and λE

The sensible heat flux is related to the difference of temperatures and is written by a bulk transfer equation

$$H = \rho_a c_p \frac{T_{aero}(z_0) - T_a(z)}{r_{ah}(z_0, z)} \tag{3.2}$$

where T_{aero} is the aerodynamic surface temperature at source height z_0, T_a is the air temperature at a reference height z, ρ_a is the air density (kg/m^3), c_p is the heat capacity of the air (J/Kg/K), $r_{ah}(z_0, z)$ is the aerodynamic resistance for heat transfer (s/m—is

the inverse of the speed, "vertical wind speed") between the source height (z_0) and the reference height (z) in the Atmospheric Surface Layer (ASL).

The aerodynamic resistance for heat transfer is given by

$$r_{ah}(z_{0h}, z) = \frac{1}{ku_*}\left[ln\left(\frac{z-d_0}{z_{0h}}\right) - \psi_h\left(\frac{z-d_0}{L}\right) + \psi_h\left(\frac{z_{0h}}{L}\right)\right] \tag{3.3}$$

where k is the Von Karman constant ($k = 0.4$), d_0 is the displacement height (m), ψ_h is the Monin-Obukhov stability correction function for heat transfer, z_{0h} is the effective source height, i.e. the roughness length for heat transfer is usually not measurable directly; and u_* is the friction velocity (m/s) in the ASL—defined as $(\tau_0/\rho_a)^{1/2}$ with τ_0 the surface shear stress. The velocity is expressed as:

$$u_* = \frac{ku_z}{ln\left(\frac{z-d_0}{z_{0m}}\right) - \psi_m\left(\frac{z-d_0}{L}\right) + \psi_m\left(\frac{z_{0m}}{L}\right)} \tag{3.4}$$

with z_{0m} the roughness length for momentum transfer (m), ψ_m is the Monin-Obukhov stability correction function for momentum transfer, and L in the equations above is the Monin-Obukhov length given as:

$$L = -\frac{\rho_a c_p u_*^3 \theta_{av}}{kgH} \tag{3.5}$$

where θ_{av} is the potential virtual air temperature near the surface (K) and g is the gravitational acceleration.

By analogy, latent heat flux is expressed by a bulk transfer equation as

$$\lambda E = \frac{\rho_a c_p}{\gamma}\frac{e_0 - e_a}{r_{aw}} \tag{3.6}$$

where λ is the latent heat for vaporization of water (J/kg), E is the actual evaporation rate (mm/s), γ (Pa/K) is the psychrometric constant, e_0 (Pa) is the surface vapor pressure, e_a (Pa) is the actual water vapor pressure of the air at temperature T_a, r_{aw} is the bulk aerodynamic resistance for water vapor transfer between the source height of water vapor (z_{0w}) and reference height (z_{ref}) in the ASL.

Assuming the land surface or soil-vegetation system can be represented as a big leaf and introducing two resistances in series, aerodynamic resistance between "surface"

and reference height in ASL and canopy surface resistance (r_c) which regulates the evapotranspiration from the vegetation by adjusting the stomata aperture, latent heat flux can be written as in the Penman-Monteith combination equation (Faivre, 2014):

$$\lambda E = \frac{\triangle r_{ah}(z_{0h}, z)(R_n - G_0) + \rho_a c_p[e_*(T_{aero}(z_{0h})) - e_a(T_a(z))]}{r_{ah}(z_{0h}, z)(\gamma + \triangle) + \gamma r_c} \tag{3.7}$$

where $\triangle$ is the slope of saturated vapor pressure at the air temperature T_a. In the Penman-Monteith equation, we assumed that the aerodynamic resistance for water vapor transfer r_{aw} is the same as for heat transfer r_{ah}, and the surface vapor pressure e_0 is equal to the saturation water vapor pressure e_* at temperature T_{aero}. For surface fully covered by wet vegetation or open water, Eq. (3.7) is reduced to Penman equation

$$\lambda E = \frac{\triangle r_{ah}(z_{0h}, z)(R_n - G_0) + \rho_a c_p[e_*(T_{aero}(z_{0h})) - e_a(T_a(z))]}{r_{ah}(z_{0h}, z)(\gamma + \triangle)} \tag{3.8}$$

3.4 Evapotranspiration and its connection with refractive index fluctuations

Evapotranspiration varies in function of numerous factor, for instance, temperature. The temperature, or better say, fluctuations of temperature affect also the index of refraction. Turbulence fluctuations are influenced by the refractive index n_ν which is dependant of humidity and principally by temperature according to (Tunick, 2003):

$$\frac{\partial n_\nu}{\partial z} = \frac{\partial n_\nu}{\partial \theta}\frac{\partial \theta}{\partial z} + \frac{\partial n_\nu}{\partial q}\frac{\partial q}{\partial z} \tag{3.9}$$

with θ the temperature, q the specific humidity and z the vertical elevation.

The structure function of the refractive index at two different points is related to the structure parameter—C_n^2, see Sec. 1.1.4

3.4.1 Index of refraction structure constant—method

One can calculate the value of the sensible flux with the measured value of C_n^2, providing that some additional meteorological data are acquired at the same time. The method is

explained in (Solignac, 2009; Rana and Katerji, 2000; Ezzahar et al., 2007; Meijninger et al., 2002). Briefly we sum up the method here.

The refractive index structure parameter C_n^2 can be written (Meijninger et al., 2002), with the structure parameter of temperature (C_T^2), humidity (C_q^2) and the covariant term (C_{Tq}) as follows:

$$C_n^2 = \frac{A_T^2}{T^2} C_T^2 + \frac{A_T A_q}{T_q} C_{Tq} + \frac{A_q^2}{q^2} C_q^2 \tag{3.10}$$

Where A_T and A_q are quantities dependent on optical wavelength and mean value of temperature (T), humidity (q) and atmospheric pressure (P, hPa).

For the wavelength used in our setup, these quantities are given by (De Bruin et al., 1995):

$$A_T = -0.776 \times 10^{-6} \frac{P}{T} \tag{3.11}$$

$$A_q = -47 \times 10^{-6} q \tag{3.12}$$

Thus, the first term in Eq. (3.10) containing C_T^2, is considered to be much larger than the two other terms. The temperature structure parameter C_T^2 can then be derived from the refractive index structure parameter C_n^2 by (Hill et al., 1980):

$$C_T^2 = C_n^2 \left(\frac{-0.78 \times 10^{-6} P}{T^2} \right)^{-2} \left(1 + \frac{0.03}{\beta} \right)^{-2} \tag{3.13}$$

Where β is the Bowen ratio, which connect temperature and humidity by the ratio of sensible flux and latent heat flux ($\beta = H/\lambda E$). The second term in brackets is a correction for the effects of humidity.

The Monin-Obukhov Similarity Theory (MOST) allows to bound the temperature structure parameter with temperature scale T^*:

$$C_T^2 = T^{*2} (z-d)^{-2/3} f_n \left(\frac{z-d}{L} \right) \tag{3.14}$$

where z and $d = 0.67 \cdot h_{veg}$ are the measurement height and the zero plane displacement height (h_{veg} referring to the height of the vegetation) respectively, and f_h is the universal

function of similarity theory, determined empirically, and depending on z and Monin-Obukhov length—L see Eq. (3.5). The Monin-Obukhov length allows to obtain the temperature T^*.

Several functional forms have been proposed to represent f_h. In this thesis, the definition of the universal function given by De Bruin et al. (1995) will be used, because it has an average behavior compared to the existing definitions in Solignac (2009). This function depends on the stability of the atmospheric surface boundary layer (ASL)—see (Barillé et al., 2016) and references therein.

In this experiment we will measure the index of refraction structure constant through two different methods. The first one is "scintillation index"—see Sec. 1.6.3, and the second one is "beam wander"—see Sec. 1.6.2.

In the far-field $\Lambda_0 \geqslant 1$, lowest-order Gaussian-beam wave is considered as a spherical wave. The values of the structure parameter are given from Eq. (1.78) at Sec. 1.6.3.

On the other hand, the second method—beam wandering, can be used to get the value of refraction index structure parameter C_n^2 through the variance of the point of maximum irradiance. For a collimated beam in the case of infinite outer scale, the values of C_n^2 are given by Eq. (1.71) at Sec. 1.6.2. We write the beam wander according to the mean square of the beam position on the detector,

$$\langle r_c^2 \rangle = \langle x^2 \rangle + \langle y^2 \rangle \tag{3.15}$$

providing that we assume locally homogeneous fluctuations. In our case, the position (horizontal x and vertical y from a zero reference) is monitored by the mean of a position sensing detector. This detector can be a lateral effect photodiode (LEP), which is a two-dimension detector that generates photocurrents proportional to the position and the intensity of the centroid of light on the active area. The current carriers generated in the illuminated region are divided between the electrodes in proportion to the distance of the current paths between the illuminated region and the electrodes. Or it can be also a quadrant ($4Q$) photodiode, which consist of four photodiodes separated by a small gap (few dozen micrometer), the position being deduced from the difference of photocurrent between the right and left side or the top and bottom side. The noise sensitivities of the $4Q$ detector and the LEP are roughly 0.2 and 0.5 (Makynen et al., 1996). In case of low background illumination, the noise level of an LEP is typically

more than ten times higher than that of the 4Q receiver due to the low (typically 10 k Ω) inter-electrode resistance. Consequently, in electrical sense the achievable SNR, and accordingly the resolution of the $4Q$ detector are better than that of the LEP (Makynen et al., 1997). We then choose a $4Q$ detector in our experiment.

3.5 Experimental setup

The scintillometer setup consists of an emitter and a receiver, placed in front of each other at the distance L, on which the measurement will be made. The emitter consists of a continuous laser and a pair of lenses to collimate the beam over the optical path. The laser wavelength used is 473nm with a power of 400mW, and with a 1.5 mrad of beam divergence. The lenses are chosen in order to have a Galilean telescope expanding the output beam of the laser and to collimate the beam over a long distance typically for distances less than 200 m. The first lens, placed just after the laser output, is a plano-concave lens with a focal length of −50mm (Thorlabs, LC1259-A). A second lens, plano-convex with a 250mm focal length is placed 20 cm from the first, in order to have a magnification of 5. The diameter of the beam at the output of the emitter is then 1 cm. This pair of lenses allows having a Rayleigh range of around 142m for the output collimated beam.

A Galilean telescope is also used in the receiver to recollect the light (Thorlabs, BE10). The measurement field for a $4Q$ detector is defined by the size of the light spot, as the detector will provide position information only up to the point where the edge of the spot reaches the gap. Therefore, to provide a sufficiently large measurement field, it is essential to enlarge the $4Q$ detector. The first lens is plano-convex with a focal length of 60mm and the second is plano-concave with a focal length of −12mm. The two lenses are separated with a distance of 86mm, enabling a magnification of 5. After the telescope, the beam is separated in two parts with a 90 : 10 beam splitter cube. The 10% part of the beam is then sent on a quadrant photodiode, which allows recording the beam position and intensity simultaneously. The quadrant photodiode is 100mm^2 (10mm ×10mm) and the gap between the four quadrants is 50μm. The 90% part of the beam is sent to an azopolymer thin film, used to record a mean value of C_n^2 over the acquisition time by the mean of self-organized surface relief grating (Barillé et al., 2013; AhmadiKanjani et al., 2005; Barillé et al., 2009). All the optical

components are mounted on a metal board for stability during the measurements. The electronic system includes a card for managing the acquisition data and a remote interface with the operators. The setup is presented in Fig. 3.1,

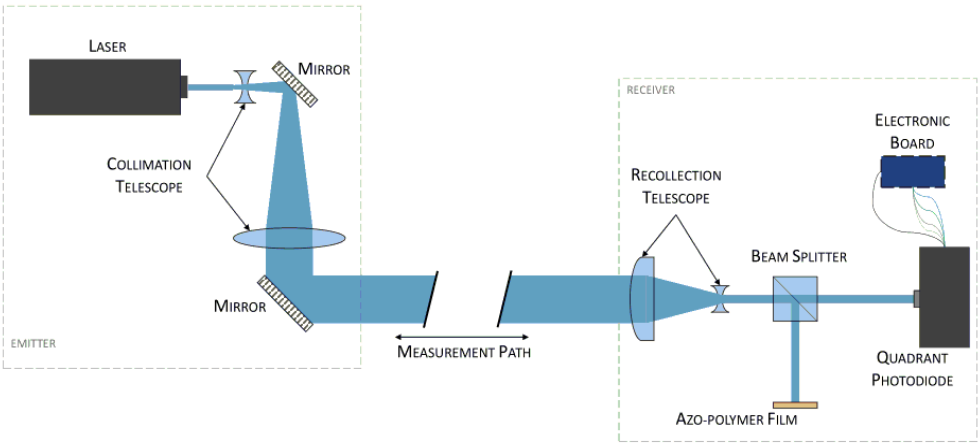

Figure 3.1: Setup with the emitter and receiver used for the experiment (shown close to one another for clarity).

The estimation of the position of the light spot center with respect to the $4Q$ center along the Y axis (Makynen et al., 1996) with P_I, P_{II} and P_Σ the power acquired by the first quadrant, second quadrant and all the quadrant respectively is:

$$\psi(x,y) = 2\frac{P_I(x,y) + P_{II}(x,y)}{P_\Sigma(x,y)} - 1 \tag{3.16}$$

Considering the symmetry of the irradiance distribution of the laser spot the same expression is also valid for the x axis. The estimation of the position can be written as:

$$\psi(x,y) \simeq \frac{\partial\psi(0,0)}{\partial(y/R)} \cdot \left(\frac{y}{R}\right) = S_y \frac{y}{R} \tag{3.17}$$

with S_y the sensitivity in A/W and R the $4Q$ radius. The sensitivity of the Quadrant Position Detector (QPD) is given with respect to the relative displacement y/R instead of the absolute displacement. The $4Q$ sensitivity for the two axial directions in the case of a Gaussian distribution of the light spot irradiance onto the $4Q$ surface is given

by the following expression (Manojlovic, 2011):

$$S_x = S_y = \frac{2R}{\omega\sqrt{\pi}} \frac{\operatorname{erf}\left(\frac{R}{\omega}\right) \exp\left[\left(\frac{R}{\omega}\right)^2\right] - \frac{2R}{\omega\sqrt{\pi}}}{\exp\left[\left(\frac{R}{\omega}\right)^2\right] - 1} \tag{3.18}$$

with ω the light spot radius and erf the Gauss error function of its arguments. We find a high sensitivity considering the used parameter of the beam width and the dimension of the $4Q$ and we obtain $S_y = S_x = 5.64$. The sensitivity is equal to 1 when the light spot radius is equal to the $4Q$ radius and higher for $\omega < R$.

However the sensitivity can change with fluctuations of the laser beam. The laser beam is not only subjected to beam wandering but also fluctuations in intensity and modifications of the beam diameter. We need to calculate the relative change $\Delta S_y/S_y$ of the $4Q$ sensitivity versus the relative change $\Delta\omega/\omega$ of the light spot radius. The absolute change of the sensitivity is given in Manojlovic (2011):

$$\Delta S_y = \Delta S_x = \frac{dS_y}{d\omega}\Delta\omega = -\frac{R}{\omega^2}\frac{dS_y}{d\left(\frac{R}{\omega}\right)}\Delta\omega \tag{3.19}$$

and the ratio of the $4Q$ sensitivity relative change and the light spot radius relative change versus the ratio of light spot radius and $4Q$ radius is then:

$$\frac{\frac{\Delta S_y}{S_y}}{\frac{\Delta\omega}{d\omega}} = -1 - 2\left(\frac{R}{\omega}\right)^2 \left\{\frac{1}{\exp\left[\left(\frac{R}{\omega}\right)^2\right] - 1}\right\} + \frac{\frac{2R}{\omega\sqrt{\pi}}}{\operatorname{erf}\left(\frac{R}{\omega}\right)\exp\left[\left(\frac{R}{\omega}\right)^2\right] - \frac{2R}{\omega\sqrt{\pi}}} \tag{3.20}$$

We consider a symmetric fluctuation of the beam width $\Delta\omega/\omega$ in the range of $\pm 10\%$ and we find a value of -1 meaning that the sensitivity relative change of the $4Q$ is not affected by the relative change of the beam diameter and is proportional to the beam width change. In the case of fluctuations of the beam size in the vertical direction as it occurs during the experiment the ratio $(\Delta S_x/S_x)/(\Delta\omega/\omega)$ is similar.

During the measurement, intensity and beam wandering fluctuations are measured continuously, and an average is recorded every 8 s as well as the temperature and the humidity. The error on the value of C_n^2 (measured with intensity) is 1×10^{-15} m$^{-2/3}$ and the error on the value of C_n^2 (measured with beam wandering) is 2.9×10^{-15} m$^{-2/3}$. The error on the temperature measurement is 0.5 °C and the error on the humidity

measurement is 2%. All measured and computed data during the experiment are logged in a text file for further studies.

3.5.1 Site Instrumental de Recherche par Télédetection Atmosphérique (SIRTA)

In the aim to validate our experimental setup of scintillometry, the setup was installed in an open field situated in the experimental platform of the SIRTA. The receiver was placed 72m far from the emitter, and the measurements were made during one day from 11 a.m. to 4 p.m. at the Atmospheric Research Laboratory of the Pierre Simon Laplace Institute. The results obtained by our scintillometer setup are compared with measurements obtained with data acquired in parallel by the SIRTA's instruments on the experimental platform.

The SIRTA's instruments consist in a meteorological platform with 3D sonic anemometers measuring wind speed in all directions and temperature. The vertical wind fluctuations and temperature correlation can be obtained. The optical setup was placed close to a 3D sonic anemometer—see photos 3.2 and 3.3, in order to acquire the local atmospheric turbulence simultaneously.

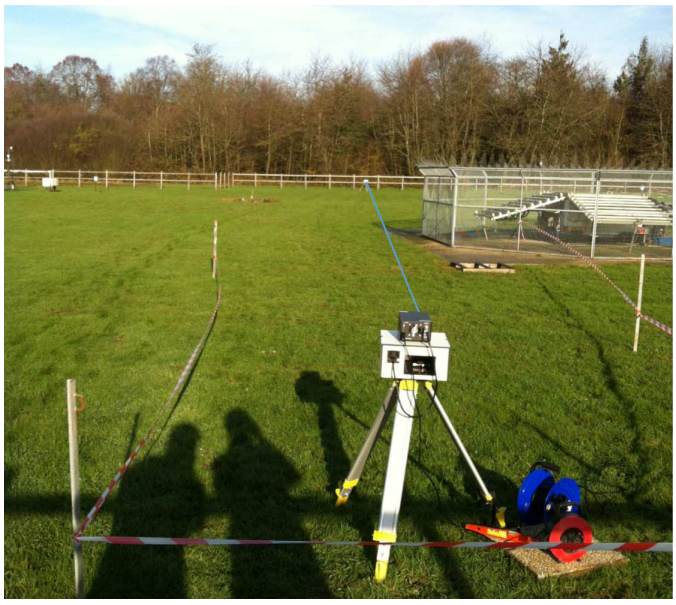

Figure 3.2: Photo of the emitter.

The 3D anemometer's data cannot provide directly a value of C_n^2, but it is possible, with the eddy covariance method, to calculate the sensible flux from the surface H (Rana and Katerji, 2000). The value of H [W/m^2] is then given by Eq. (3.2) and the latent heat flux—"evapotranspiration", and the other fluxes are calculated as in the procedure described in Sec. 3.3.

Figure 3.3: Photo of the receptor.

3.6 Experimental results

3.6.1 Refractive index structure parameter

The value of C_n^2 versus time calculated with Eq. (1.78) and the intensity fluctuations is presented in Fig. 3.4 with temperature and humidity data measured simultaneously.

A good correlation between the behavior of C_n^2 and the evolution of the temperature and humidity acquired during the experience is shown. When the temperature decreases the humidity increases simultaneously during the first half hour of the measurement. The increase of the temperature dries the atmosphere and reduces the humidity. There is a maximum time shift of 10 minutes between the large variations of the temperature and humidity and C_n^2. The Fig. 3.5 compares humidity and temperature with C_n^2 to account for the inertial variation of these two parameters on the atmospheric turbulence. We consider in the calculation the moving average values to smooth all the data.

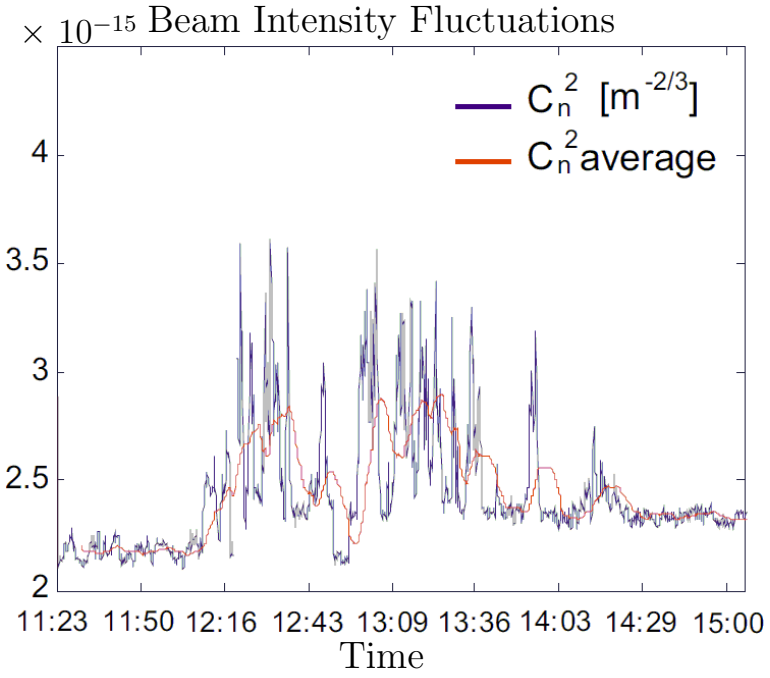

Figure 3.4: C_n^2 vs time calculated with the laser beam intensity fluctuations.

The maximum changes in the refractive index structure constant appears for a maximum of humidity and a minimum of temperature changes meaning that C_n^2 is modified by the gradient of temperature. In Fig. 3.5 the positive gradient of temperature is delimited. We observe that a positive gradient of temperature of 0.5 °C induces a variation of 1×10^{-15} m$^{-2/3}$. We note that humidity and temperature are measured locally at the receptor and cannot account for the very high peaks on the C_n^2 measured on a large distance. This result confirms that two micrometeorological data (temperature and humidity) can reflect the average turbulence.

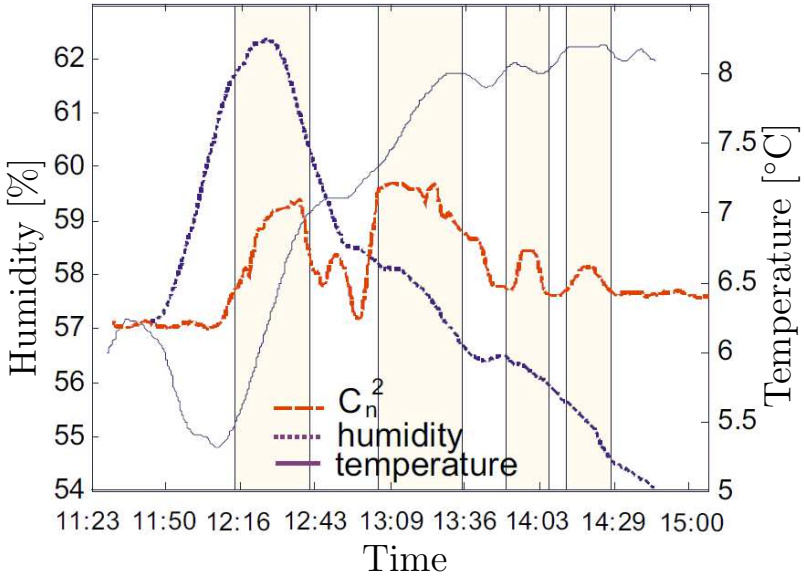

Figure 3.5: Comparison of evolution of *temperature* (left axis) and *humidity* (right axis) with atmospheric turbulence measured with the intensity fluctuations.

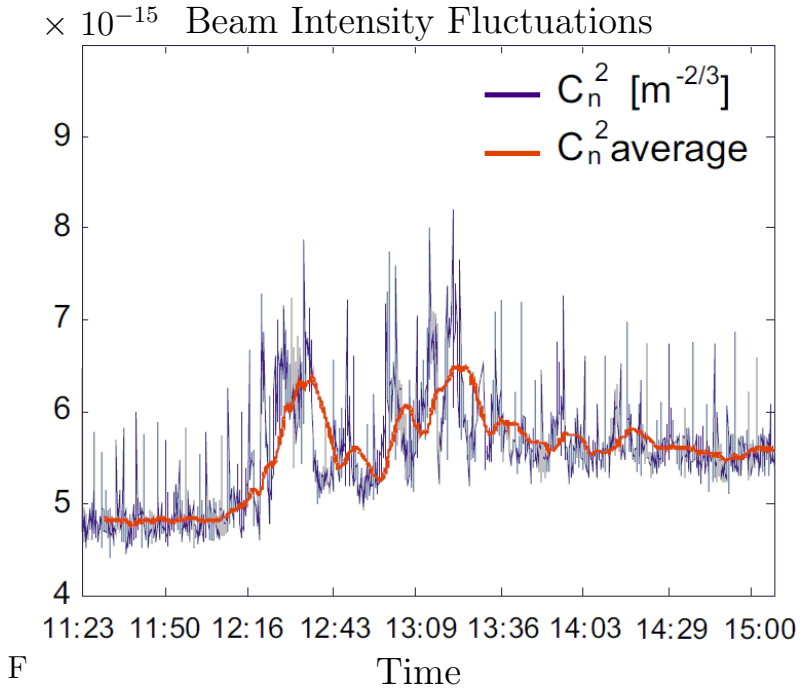

F

Figure 3.6: C_n^2 *vs* time calculated with the laser beam wandering fluctuations using Eq. (1.71).

The values of C_n^2 calculated with the intensity fluctuations are compared with the beam wandering method—see Eq. (1.71). Using the measured fluctuations of the beam positions onto the detector during acquisition of data. The results are presented in Fig. 3.6.

We observe a ratio between the two calculated values of C_n^2 of 2.28 corresponding to a value of C_n^2 with the beam deflection of almost twice the one calculated with the intensity fluctuations. This result can be explained by the precision on the beam wandering measurement with the $4Q$. During the acquisition with the beam wandering method the laser beam diameter fluctuates in x and y non-symmetrically. An asymmetry on the beam is due to large refractive index fluctuations mainly in the vertical direction where the gradient in the atmospheric layer is the maximum. The fluctuations of the laser positions through the lens at the input of the detector can also induce astigmatism and transverse aberrations. However in the case of the measurement of C_n^2 with the beam wandering method a dynamic is observed with the $4Q$ larger than with the intensity fluctuation method. A part of the two plots of C_n^2 with the two methods is represented in Fig. 3.7 with an estimation of the error in both cases.

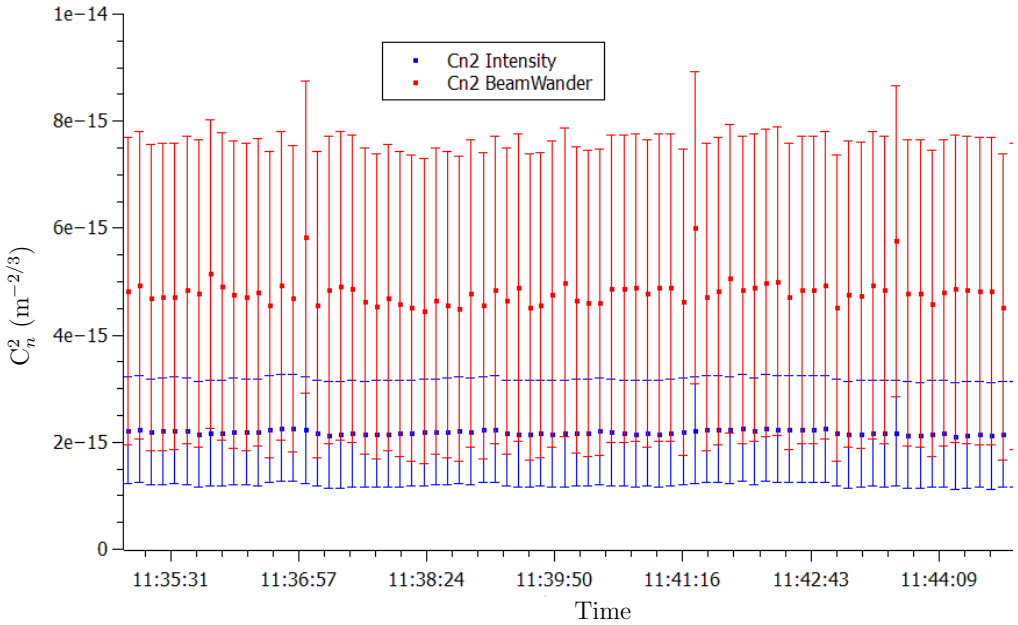

Figure 3.7: Comparison of C_n^2 *vs* time calculated with the beam wandering fluctuations and C_n^2 *vs* time calculated with the laser beam intensity fluctuations during a time range of 10 minutes showing an estimation of the error on both measurements.

For the error on C_n^2 calculated with intensity fluctuations, we assume an error on the measured optical path length of 1 m. The error for intensity fluctuations is taken as the standard deviation: 1.35×10^{-15} m$^{-2/3}$. The error on C_n^2 calculated with the beam wandering method is larger due to the error on the calibration of the detector done with a millimetric translation stage (error = ± 0.5 mm).

During the experiment, we observe that the position fluctuations of the beam are not the same for the horizontal and vertical axis and are given by:

$$\frac{\langle x^2 \rangle}{\langle y^2 \rangle} = 1.45 \tag{3.21}$$

The horizontal fluctuations are almost 45% larger than the vertical fluctuations, this difference is due to the shape of the beam, which was Gaussian on the receiver with a larger dimension in x direction like an ellipsoid shape. Indeed, as the quadrant photodiode is used to measure the position, this measurement is affected by the beam profile, whereas the intensity measurement is not. Moreover, the experiment was conducted in the month of December with outside temperatures showing small fluctuations. The vertical gradient of temperature does not introduce a large difference of position fluctuations between the two axes.

When comparing the mean values for the C_n^2 measured with the two methods, we find:

$$\frac{C_{nBW}^2}{C_{nI}^2} = 2.28 \tag{3.22}$$

as C_{nBW}^2 has 50% more error than C_{nI}^2, this error is a product of the Beam wander equation that doesn't take into account the natural diffraction of the beam through the propagation as the scintillation does. The Fig. 3.7 shows that the two error estimations overlap on a relatively important value range for C_n^2 measured with the intensity fluctuations and beam wandering. The overlap is estimated to be 1×10^{-15} m$^{-2/3}$.

3.6.2 Sensible flux and comparison with SIRTA

The values of the sensible flux H and the latent heat flux λE can be calculated with the C_n^2 values measured by our device and the method described in Sec. 3.4.1. The measurements obtained for the sensible flux H and λE are compared to acquired values using data from the 3D sonic anemometer of SIRTA and using Eq. (3.2). The

sensible flux obtained with our laser scintillometer setup is compared to the sensible flux obtained with the data of SIRTA in the Fig. 3.8.

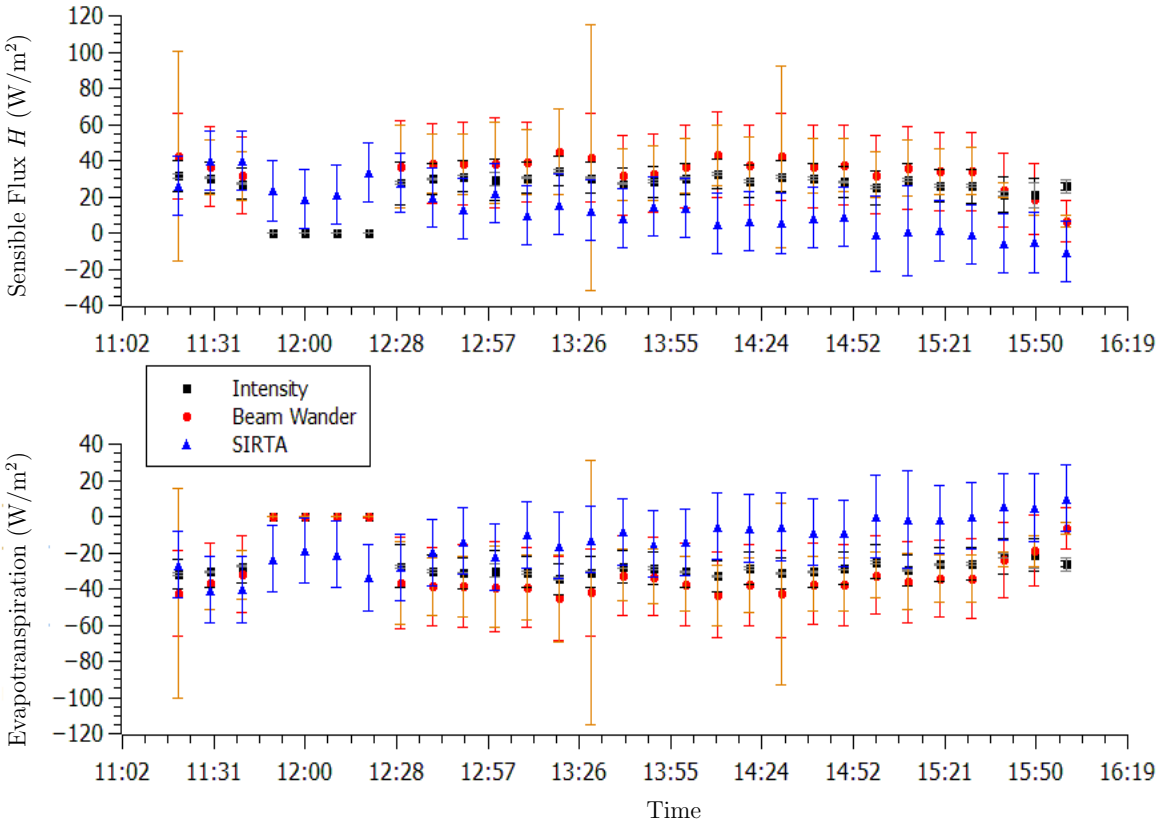

Figure 3.8: Comparison between the values of Sensible flux and evapotranspiration measured with our device (with intensity fluctuations method–*black*–and with beam wandering method–*red*) and the ones calculated from the SIRTA data (*blue*).

The measured sensible flux with our scintillometer setup is very close ($<$ 20 W m^{-2}) to the value calculated with the eddy covariance method using the 3D sonic anemometers of the SIRTA's experimental platform. The data points show common values and a good overlap between error bars. However results obtained with intensity fluctuations are closer to results obtained with the eddy covariance than values obtained with the beam wandering in the range of 7%.

The comparison between a well known scintillometric device and a working commercial device gives us a good appreciation of the accuracy of our setup. However we need to consider that the value of C_n^2 measured with our device is integrated over

the beam path whereas the value obtained by the 3D sonic anemometers is measured at one fix point and at a higher elevation from the ground. Furthermore, data were collected during the month of December, when sensible flux is very small, making the amplitude of the data as small as 40 W m^{-2}. These two points explain why the Fig. 3.8 doesn't show a slope of ± 1.

3.6.3 Evapotranspiration

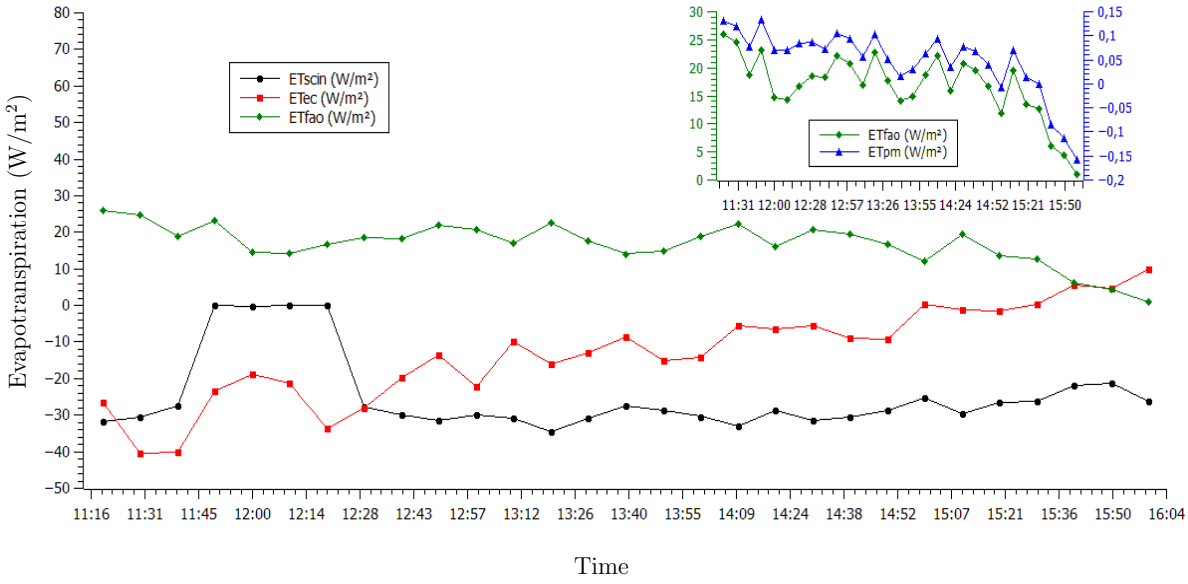

Figure 3.9: Evapotranspiration calculations with data provided by the laser fluctuations (ET_{scin}) and the eddy covariance (ET_{ec}) and comparison with the calculation given by the FAO model.

Three calculations of evapotranspiration are compared. The evapotranspiration calculated with data acquired by the scintillometer set-up (ET_{scin}) with the intensity fluctuations and based on the model described in Meijninger et al. (2002), is compared with the results calculated with the eddy covariance data (ET_{ec}). These two calculations of evapotranspiration are compared to the FAO Penman-Monteith method as a standard ET_o method (Von Randow et al., 2008; Cai, Liu, Lei and Pereira, 2007)—The United Nations Food and Agriculture Organization (FAO) accepts as a standard method for modeling evapotranspiration, the Penman–Monteith equation—see Eq. (3.7). This method has been reported to be able to provide ET_o values in many regions and cli-

mates and it has been accepted worldwide as a good ET_o estimator when compared with others methods especially for daily computation. This method requires daily data on maximum and minimum air temperatures (T_{max} and T_{min}), relative humidity and wind speed. We observe in the Fig. 3.9 that the measurements with the scintillometer are close to the measurements with the eddy-covariance. The measurements with eddy-covariance rise with a slope and follow the variation of temperatures given in Fig. 3.5. However the slope for the measurements with the scintillometer is low. This can be explained by the average measurements along the laser path compared to the eddy-covariance giving a local measurement. Finally we can conclude that the FAO model gives the upper limit with a relative constant evolution as a function of time and the ET values with the scintillometer gives the lower values.

3.7 Conclusions

The present work proposes a comparison of two optical techniques for measuring the atmospheric turbulence. This optical metrology is tested in real condition over a path length of 72 m in the experimental platform of SIRTA. C_n^2 values are obtained using intensity and beam wandering fluctuations in parallel. Both values of C_n^2 acquired with intensity fluctuations and beam wandering calculated with the Eqs. (1.78) and (1.71) respectively are accurate, since we find the same value of the sensible flux (H) in the limit of the error bars when compared to the value given by eddy covariance data acquired at the same time. The values of C_n^2 obtained with the beam wandering method (1.71), are very close to the ones obtained with the intensity fluctuation method (1.78). Our measurements show the main contribution of the two atmospheric parameters (temperature and humidity) in the evapotranspiration variations and particularly the temporal contribution. This comparison gives us a good insight of our device's accuracy and capabilities. Finally these measurements lead us to calculate the evapotranspiration. We have then compared our measurements with two other models calculated with local atmospheric parameters. Our model is close to the results calculated with the eddy-covariance data and far from the values calculated with the FAO model.

Chapter 4

Propagation of Unconventional Beams through Turbulence

The scintillation is an important detrimental effect due to the atmospheric turbulence which have been studied with attention. Nowadays, find new transmitters which are affected in a minor degree by the turbulence could improve its applications in diverse areas. In this chapter we will describe two experiments involving the propagation of new unconventional transmitters in a turbulent medium. These experiments are studied from the scintillation index point of view and the transmitters are compared with a tranditional Gaussian beam.

4.1 Introduction to the experiments

Recently, more and more attention is paid to the use of optical beams for free-space optical (FSO) communications due to the increasing requirement for larger bandwidths and high rate of data transfer in optical wavelength. The high direction of the optical beams can guarantee the security of the transmitted data to a certain extent in FSO communications compared to that in Radio-frequency (RF) communications. Furthermore, optical beams are also applied in other applications, such as laser satellite communications, laser radar system and remote sensing. In those applications, propagation of optical beam in atmosphere is inevitably encountered.

However, atmospheric factors are the most serious disadvantage to FSO because

they can limit operating availability and/or cause distortions of the carrier wave. In addition, optical turbulence resulting from small temperature variations in the atmosphere gives rise to further power losses from spreading of the beam spot radius beyond that due to diffraction alone, and to temporal and spatial fluctuations of the laser beam known as scintillation, as well as influences in the degree of coherence and the degree of polarization (Korotkova and Wolf, 2007; Korotkova and Shchepakina, 2010; Ji et al., 2010). Scintillations of a light beams are important since intensity fluctuations degrade ratio of signal to noise and may increase bit error rate. Tyson (2002) analyzed an adaptive optics compensation for atmospheric-turbulence-induced scintillation.

Diverse types of beams have been studied in optical turbulence, those studies are focused in the scintillation and the way to reduce it. Beam scintillations are closely related to beam properties, like beam shape, phase, polarization, coherence to name a few. Previous studies have shown that different beams, appropriately modulating coherence, phase and polarization of input laser beams can reduce the scintillations. It is discovered that the on-axis scintillation index of an elliptical Gaussian beam can be smaller than that of a circular Gaussian beam in weak turbulences under certain conditions (Cai, Chen, Eyyuboglu and Baykal, 2007). Other types of beams have been also studied, such as (multi) Gaussian Schell-model—Gaussian Schell-model (GSM) beams are common in the theoretical studies because in some cases this model allows for analytical results to be derived in a closed form. Since then, investigation of propagation of partially coherent beams in turbulent atmosphere has become a topic of interest, and many optimization schemes have been proposed (Schulz, 2005; Qian et al., 2009; Wang et al., 2012; Korotkova et al., 2012). Qian et al. (2009) found that the degradation of degree of source coherence of pseudo-partially coherent GSM beams may cause reductions of scintillation index, which indicates that partially coherent beams are more resistant to atmospheric turbulence than fully coherent beams. The property of polarization influences the scintillation of a laser beam on propagation in atmospheric turbulence as well (Korotkova, 2008; Gu et al., 2009; Cheng et al., 2009). An appropriately chosen coherent beam of non-uniform polarization also has smaller scintillation index than a beam of uniform polarization (Gu et al., 2009). Gu and Gbur (2012) showed that the turbulence-induced scintillation can be further reduced by using an incoherent beam array composed of beamlets with nonuniform polarization. Chen et al. (2014) have found that the scintillation index of a partially coherent

radially polarized beam can be smaller than that of a completely coherent beam, this study included an outdoor experiment over 400m path.

Another method to reducing scintillation is substituting a single incident beam by beam arrays (Eyyuboğlu et al., 2008; Peleg and Moloney, 2006; Polynkin et al., 2007; Gu and Gbur, 2010). Polynkin et al. (2007) studied the minimum of the scintillation index with respect to the beam separation for multiemitter beams composed of two and four identical fundamental Gaussian beams. Thereafter, the scintillation index can be substantially reduced if the constituent beams overlap at the detector and are properly separated in the transmitter plane.

Beams with spiral phase are known as vortex beams, each photon carrying orbital angular momentum (OAM). OAM can be used to encode data for transmitting information in free-space optical systems (Gibson et al., 2004; Čelechovský and Bouchal, n.d.). It has been demonstrated that the OAM of a beam can be well preserved in a long propagation distance in weak turbulence (Gbur and Tyson, 2008). The scintillations of circular vortex beams in turbulence have also been studied (Ji et al., 2010; Cheng et al., 2009). (Cheng et al., 2009) demonstrated numerically that the vector vortex beam shows substantially lower scintillation than the scalar vortex. Liu and Pu (2011) propagated elliptical vortex beams in turbulent atmosphere finding a new way to reduce scintillation index.

In the next sections, we describe two experiments based on the study of new transmitters through atmospheric turbulence, in them, we analyzing its intensity fluctuations due to the turbulent medium. The first experiment involves a new optical vortex called *Phase-flipped Gaussian beam*, the second one corresponds a multiwavelength beam—*supercontinuum*.

4.2 Phase–flipped Gaussian beam

Had Thomas Young, in his celebrated demonstration of optical interference (Young, 1804), generalized his two-slit experiment to three or more slits, he would have discovered a qualitatively different type of destructive interference*. For in general, when three or more waves interfere, light vanishes at points, rather than on fringes, in two

*In fact, Young could not have generalized his experiment as he did not use slits at all but rather a single line obstruction in a pencil of light.

dimensions. At these places where the intensity of the wave is zero, the phase is undefined—singular, and in general, all 2π phase values occur around the zero, leading to a circulation of the optical energy. These points, which are extremely general features of optical fields, are known by various terms encompassing these properties: nodal points, phase singularities, wave dislocations, and optical vortices.

Optical vortices—also known as a screw dislocation or phase singularity, is an optical field with a point of zero intensity. In optical vortices, light is twisted like a corkscrew around its axis of travel—being cancelled each other out light waves at the axis itself, producing a darkness at the center.

Phase singularities are a phenomenon in a physical field of at least two variables (e.g., positions x and y), where the physical quantity represented by the field can naturally be represented in a plane, such as the Argand plane of complex numbers. In optics, this is naturally the complex amplitude of a scalar optical field, whose modulus is the real amplitude and argument is the phase. For this field, we write

$$U = \rho \exp[i\chi] \tag{4.1}$$

where ρ is the real amplitude, and χ is the phase.

Optical phase singularities have recently become a fashionable topic in optical physics, partly through their relationship with beams carrying orbital angular momentum—see (Dennis et al., 2009, Chp. 5) and references therein, and a range of techniques have been developed to generate optical fields containing vortices. Vortices also occur naturally in optical fields; in a random optical wave such as a speckle field, there are many vortices interspersed between the bright speckles, and the correlation properties of the vortex points are related to those of the field—see Dennis et al. (2009, Chp. 5) to generation of vortex beams.

In this section we study a new type of optical vortex propagating through atmospheric turbulence. This vortex beam has a π phase flip in the intensity amplitudes between the two halves of the beam profile—It is called *flipped mode* and also known as *phase-flipped Gaussian beam*.

A flipped mode is achieved with a Sagnac loop, see Fig. 4.1. Half of the laser beam in the Sagnac interferometer is blocked with a knife edge, in order to create an asymmetry between the interfering beams. The transverse amplitude of the counter-

clockwise (CCW) propagating beam is π phase shifted relative to the clockwise (CW) propagating beam because they each have experienced two transmissions and reflections on the beam splitter, respectively (Delaubert et al., 2002).

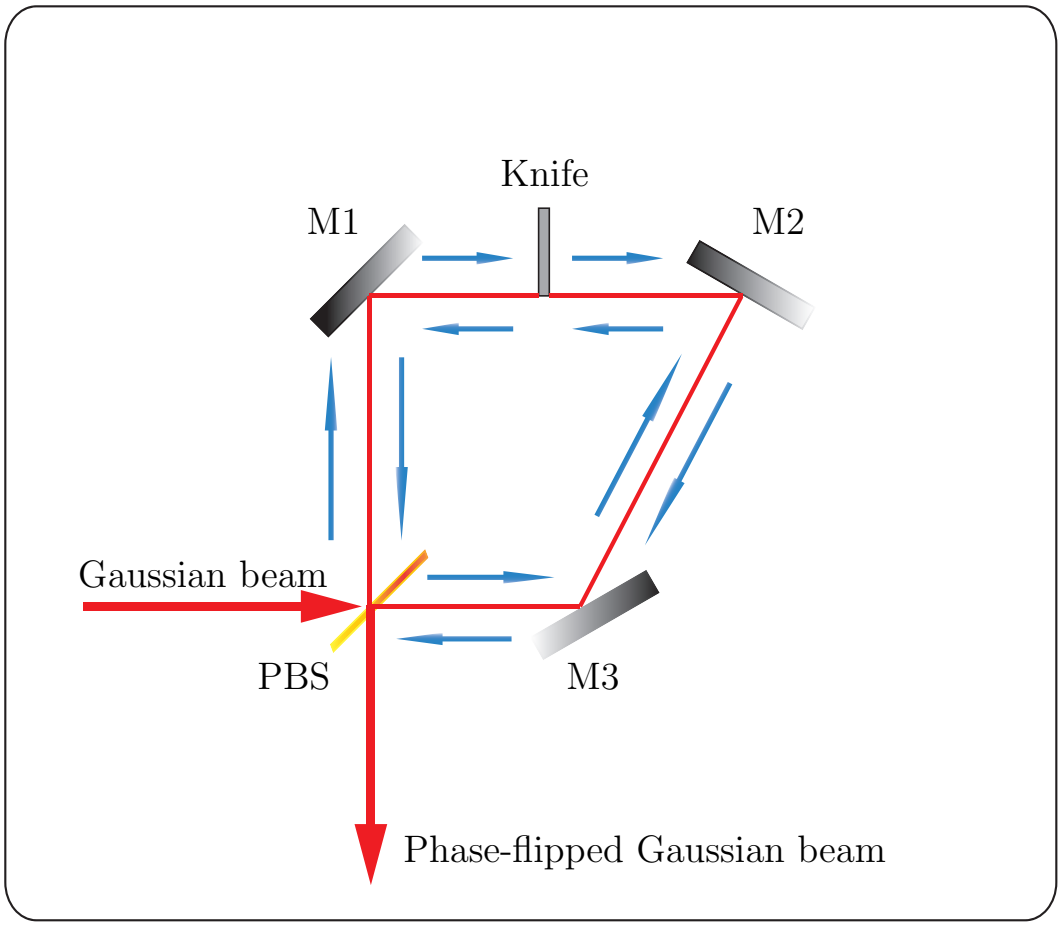

Figure 4.1: Sagnac's Interference: Creation of a phase-flipped Gaussian beam. The red thick line denotes the TEM_{00} at the input, while the thin light-blue lines correspond to the trajectory of each beam inside the loop. Finally at the output, the interferometer generates the flipped Gaussian mode. It is composed by a pellicle beamsplitter (PBS), and three mirrors (M1, M2, M3)

Both beams at the Sganac's interferometer have to traverse the same optical path length up to arrive the knife. Therefore, the beams opposite one another at the knife have the same effective radius. This explain the dispositions of the mirrors at Fig. 4.1.

4.2.1 Optical setup

The development of the experiment was under the frame described in the previous Section. We propagate a collimated beam through a weak turbulence. Both Gaussian beam and phase-flipped Gaussian beam are produced by He-Ne laser of 25mW with a $\lambda =$ 632.8nm (Melles Griot, 25-LHP-828-230 and $1/e^2$ beam diameter of 1.23mm). The beam propagates and enters to the Sagnac interferometer. The interferometer is composed by three mirrors and one beamsplitter of 50:50, which is a pellicle beamsplitter (Edmund Optics, 39485) with no ghost images from second surface reflections and no change in optical path length. We used a knife—Gillete's razor, to obstruct the half of the Gaussian beam. The CCW beam experimented only three reflections instead of the five experienced by the CW beam—see photo 4.2. Photo 4.3 shows the two lobes of the flipped mode, this picture presents the destructive interference at the center.

Figure 4.2: Photo of Sagnac loop.

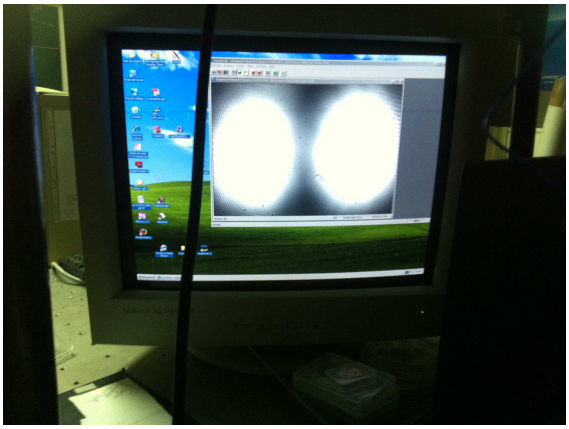

Figure 4.3: Lobes of the flipped mode.

Once the flipped Gaussian mode is created, it is propagated through an optical turbulent channel of 43cm length. We used a camera CCD (Thorlabs, DCC1645C) for the detection, the frame rate used was 25fps. The total path length until the CCD is 54cm.

To simulate the optical turbulence—see Section 2.1.1, we used a turbulator—made it in France by Antonin Poisson. The relation between the structure constant C_n^2 and the difference of temperature ΔT for this equipment is shown in Fig. 4.4. In this figure,

the blue line fit equation is (values are given with a 95% of confidence).

$$C_n^2(\Delta T) = 1.12 \times 10^{-15}\Delta T + 1.506 \times 10^{-14}; \quad R = 0.9046, \tag{4.2}$$

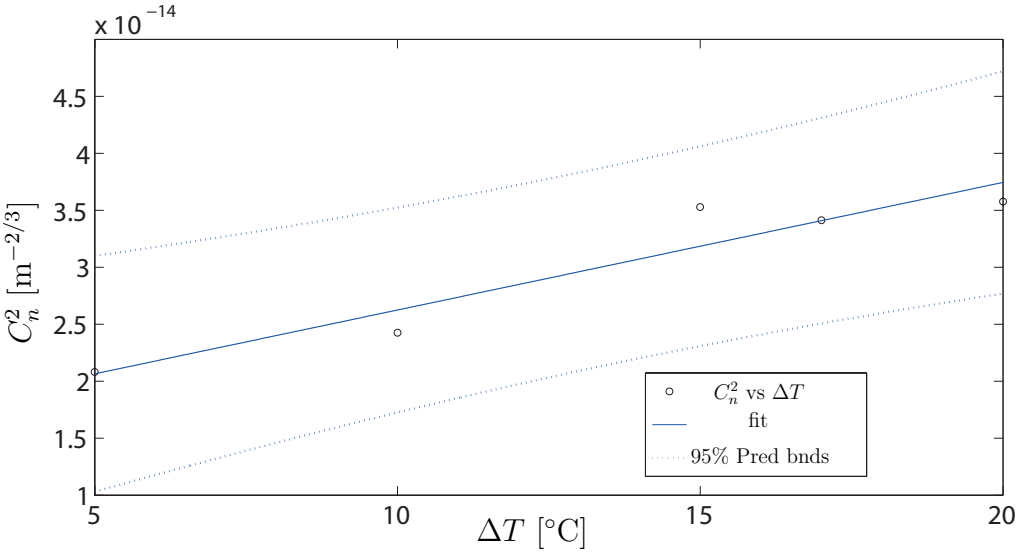

Figure 4.4: C_n^2 in function of ΔT. Characterization of the turbulator developed in France.

The turbulator lets us to develop the experiment in a rank of difference of temperature between 5°C and 20°C. For our experiment we measure 5°C, 10°C, 15°C, and 20°C of temperature difference.

4.2.2 Experimental results

In this section we analyze the data of the experiment taking into account the scintillation index equation—see Eq. (1.74) at Sec. 1.6.3.

Fig. 4.5 displays the experimental results for the scintillation of both, flipped mode and Gaussian beam, at different instensities of turbulence. The structure parameter is $C_n^2 \sim 10^{-14}$ for our experiment, corresponding to a weak turbulence. A experimental mean reduction of 79% is found for the flipped mode scintillation compared to the fluctuations of a Gaussian beam. Also, we can conclude that the intensity fluctuations increase in accordance with the growth of temperature difference—for a Gaussian beam,

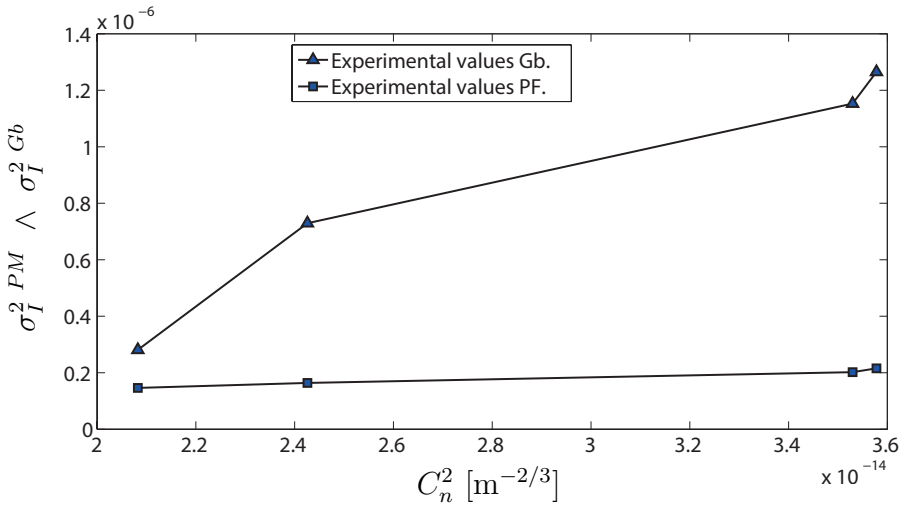

Figure 4.5: Experimental scintillation index for flipped mode (PM) and Gaussian beam (Gb), in relation to structure parameter—C_n^2.

this result is given by the existent proportionality between the scintillation index and the structure parameter—see Sec. 1.6.3. On the other hand, flipped mode's scintillation index is proportional to the change of temperatures as well. Despite of the existing proportionality the curve seems constant, this is explained because the scintillation index is around 80% lower than the intensity fluctuations of the Gaussian beam.

4.2.3 Theoretical approach

A phase-flipped Gaussian beam (PF) is the lowest-order traverse electromagnetic Gaussian-beam wave (TEM_{00}) which has a π phase jump between two halves of its beam profile (Delaubert et al., 2002; Banerji, 2006). Phase singularities are features of scalar optics and occur naturally only in (complex) scalar components of vectorial fields—see Eq. (4.1). In the plane of the emitting aperture of the transmitter, $z = 0$, we propose a representation of the field as

$$U_0^{\text{PF}}(\mathbf{r}, 0) = \exp\left[-\left(\frac{1}{W_0^2} + i\frac{k}{2F_0}\right)\|\mathbf{r}\|^2\right]\exp[-i\ \Delta\varphi(kx)] = U_0(\mathbf{r}, 0)\exp[-i\pi H(kx)] \tag{4.3}$$

where W_0 and F_0 are respectively the *effective beam radius* and *radius of curvature* at the input or transmitter plane, $\mathbf{r} = (x, y)$ are the coordinates in this plane (with origin

at the beam center), and $k = 2\pi/\lambda$ with wavelength λ. The term $\Delta\varphi(kx)$—is the phase χ at Eq. (4.1), it denotes the flipped phase which arises from the difference at the tranverse length path by the two lobes—$\Delta\varphi(kx) = knd(kx) = (\lambda/2)H(kx)$, where $nd(kx)$ is the optical path difference—$d(kx)$ is the transverse path of the lobes, and n is the refractive index of the air in our study—the *Heaviside step function*, $H(\cdot)$, represents the phase flip. $U_0(\mathbf{r}, 0)$ denotes the gaussian part of the field in the absence of turbulence (the initial amplitud has been set to one). The field proposed in Eq. (4.3) is displayed in Fig. 4.6.

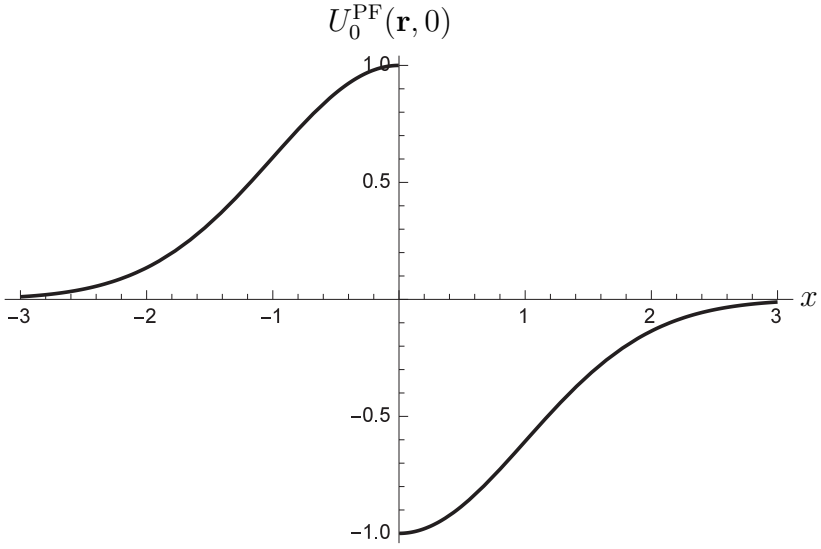

Figure 4.6: Electromagnetic field for a *phase-flipped Gaussian beam.*

Free-space propagation of this field across a distance z from the transmitter plane is given by the Huygens-Fresnel principle (see Section 1.4.2). Straightforward, this principle gives the unperturbed field at $z = L$—see Eq. (A.1) for details,

$$U_0^{\mathrm{PF}}(\mathbf{r}, z) = \operatorname{erf}\left[\sqrt{\frac{k}{2iz}(\Theta - i\Lambda)}x\right] U_0(\mathbf{r}, z)\,, \tag{4.4}$$

where

$$U_0(\mathbf{r}, z) = (\Theta - i\Lambda)\exp\left[ikz + \frac{ik}{2z}\left(\overline{\Theta} + i\Lambda\right)\|\mathbf{r}\|^2\right] \tag{4.5}$$

represents a Gaussian beam at z defined by $\overline{\Theta} = 1 - \Theta$, $\Theta - i\Lambda = 1/(\Theta_0 + i\Lambda_0)$, with

$$\Theta_0 = 1 - \frac{z}{F_0}, \quad \text{and} \quad \Lambda_0 = \frac{2z}{kW_0^2} \tag{4.6}$$

the *curvature* and *Fresnel parameters*, respectively—erf(·) is the error function; Fig. 4.7 displays the Intensity of the field— The intensity at this figure, confirms the Photo 4.3. Observe that the total power of the flipped Gaussian mode at the receiving plane is $\pi\ W_0^2/2$ [Watts]—see Eq. (A.12) for details.

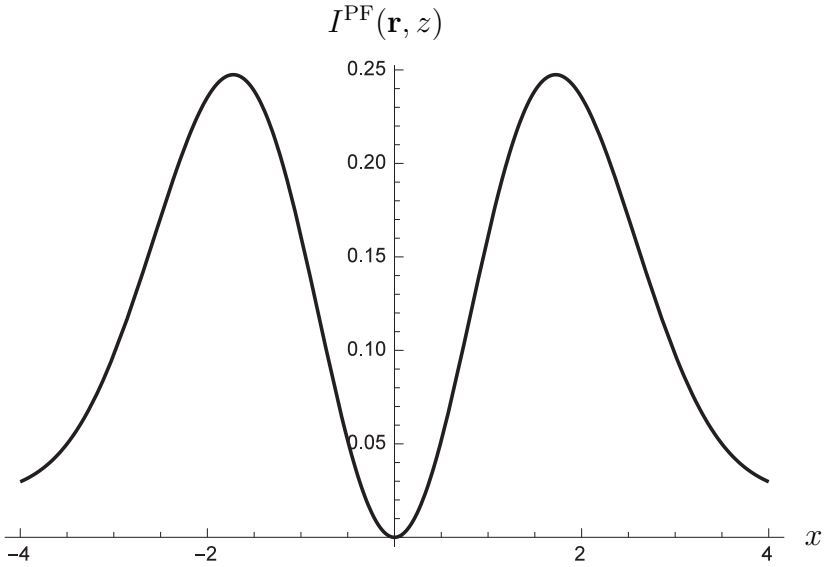

Figure 4.7: Intensity of the flipped Gaussian mode.

4.2.4 Scintillation index for a phase–flipped Gaussian Beam

The stochastic phase-flipped Gaussian beam satisfies the *stochastic Helmholtz equation*. The most well known classical approaches to solve this equation, when the refractive index varies slowly with the position, are the extended Huygens-Fresnel Principle and the Born and Rytov perturbation.

Previously to the scintillation index—see Sec. 1.6.3, we need to obtain the second-order statistical moments—see Sec. 1.5.2. Henceforth, we focus in the spectral representation of the field.

The first-order spectral representation, $\psi_1(\mathbf{r}, L)$, is connected to the first normalized Born perturbation, $\Phi_1(\mathbf{r}, L)$. The former is represented by—see Eq. (1.45) and Eq. (A.13),

$$\psi_1^{PF}(\mathbf{r}, L) \simeq \Phi_1^{PF}(\mathbf{r}, L) = \frac{U_1^{PF}(\mathbf{r}, L)}{U_0^{PF}(\mathbf{r}, L)} =$$
$$= ik \int_0^L dz \int \int_{-\infty}^{\infty} d\nu(\boldsymbol{\kappa}, z) \exp\left[i\gamma \boldsymbol{\kappa} \cdot \mathbf{r} - \frac{i\kappa^2 \gamma}{2k}(L - z) \right] \frac{\operatorname{erf}\left[\left(\frac{x}{W} - \frac{(L-z)}{kW}\kappa_x \right) \sqrt{\frac{\Theta_0 - i\Lambda_0}{i\Lambda_0}} \right]}{\operatorname{erf}\left[\frac{x}{W} \sqrt{\frac{\Theta_0 - i\Lambda_0}{i\Lambda_0}} \right]} \tag{4.7}$$

Eq. (4.7) is written in function of the controllable parameters at the laboratory, Eq. (4.6); while W is the spot size at the receiver, and the complex path amplitude weighting parameter was given in Sec. 1.5.

Assuming that the beam propagates through a statistically homogeneous and isotropic medium in each transverse plane, thereby the wave number $\boldsymbol{\kappa}$ is replaced by its scalar $\kappa = |\boldsymbol{\kappa}|$, that is $\Phi_n(\boldsymbol{\kappa}) = \Phi_n(\kappa)$. Moreover, we ensure statistical homogeneity of the refractive index, see Eq. (A.20) and Eq. (A.21). These integrals have to be calculated numerically.

4.3 Supercontinuum

The process known as supercontinuum (SC) generation occurs when narrow-band incident pulses undergo extreme nonlinear spectral broadening to yield a broadband spectrally continuous output, giving very often a white light (Dudley et al., 2006). In this section, we briefly review the experimental setup for a supercontinuum light, to propagating through optical turbulence. The results show a reduction in the irradiance fluctuations induced by the random media, compared with a monochromatic beam.

4.3.1 Experimental setup

We propagate a collimated SC beam—$1/e^2$ beam diameter of $\sim$ 9mm. SC has a spectrum extends from 400–450nm to 1800–1900nm, with 1064 nm of a pump wavelength passively q-switched microchip laser—microship 10kW peak power, with a 50mW av-

erage power and pulse duration around 800ps. In the fibre, the pulses are longer, due to chromatic dispersion.

The optical turbulence is simulated by the turbulator made in France—we measure 5°C, 10°C, 15°C, 17°C, and 20°C of temperature difference. The intensity of turbulence is $C_n^2 \sim 10^{-14}$, given by the Eq. (4.2) and Fig. 4.4. At the receptor, we used a quadrant detector (First Sensor, QP100−6SMD) for sensing the intensity—it is given by the sum of the voltage at each quadrant. The quadrant detector is controlled by an Arduino (MEGA2560)—sampling at 600 data per second. The total length path until the detector is 45cm. We use some interferential filters to select specific wavelengths to compare with the SC beam. The setup is showed in Photo 4.8,

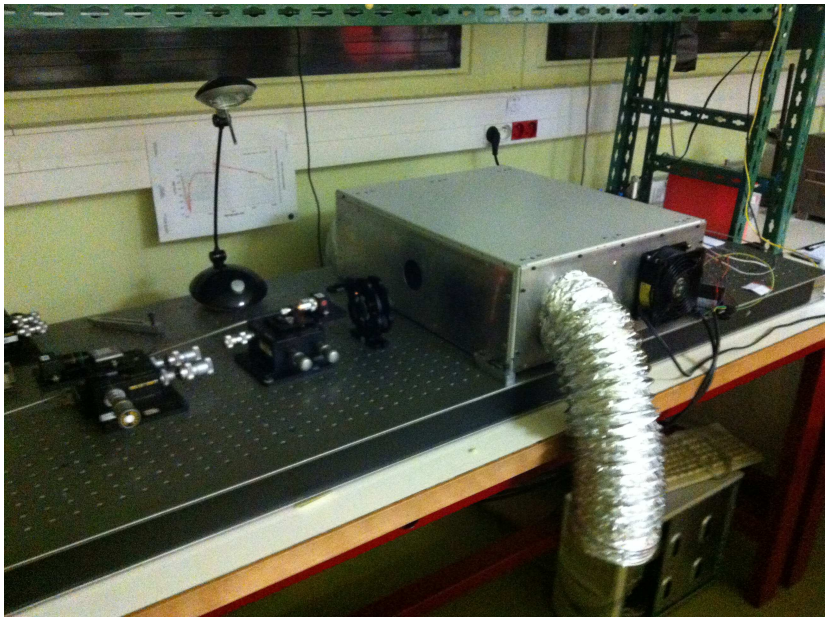

Figure 4.8: Optical setup for supercontinuum.

4.3.2 Results

In this experiment we analyze the fluctuations of intensity at the quadrant detector—see Eq. (1.74) at Sec. 1.6.3.

The Fig. 4.9 presents the experimental results. It displays the scintillation reduction regarding different intensities of turbulence, the structure parameter is $C_n^2 \sim 10^{-14}$ for our experiment, as in the Sec. 4.2.2. A mean reduction of 99%, 97%, and 96% shows the

scintillation for a SC in relation to a monochromatic beam with wavelength of 600 nm, 700 nm, and 800 nm, respectively. From the Fig. 4.9 we conclude, the Gaussian beam's scintillation index goes towards to the scintillation index of a SC to the extent that the wavelength goes to the size of the bandwidth—in number. That is, a monochromatic beam with wavelengths close to the infrared (IR) senses less the detrimental effects of the turbulence. Moreover, as in Secs. 1.6.3 and 4.2.2, the intensity fluctuations for a Gaussian monochromatic beam are proportional to the index of refraction structure constant. The more prominent result which validates the proportionality is given at 600nm, the increase in proportion to the temperature difference is kept for 700nm and 800nm. The same proportional growth is given for SC, which seems constant due to the 100% (roughly) of mean reduction in relation to the Gaussian monochormatic beam of 600nm.

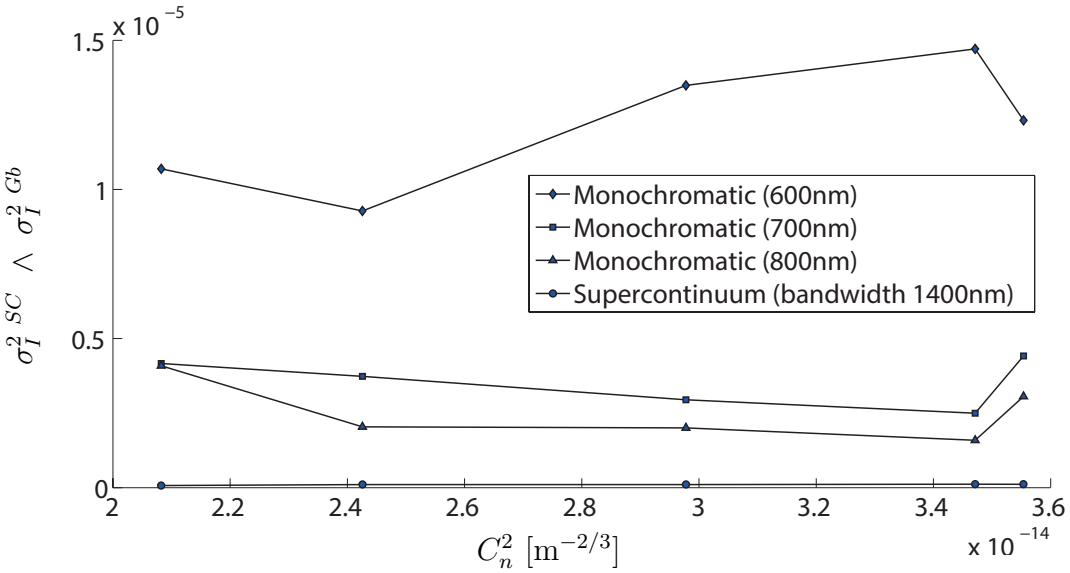

Figure 4.9: Experimental scintillation index for a Supercontinuum (SC) and Gaussian beam (Gb), in relation to structure parameter—C_n^2.

Conclusions

We started Chp. 1 making a revision of the passive scalar fields, for instance, the refractive index is among them: this is well-known in Atmospheric Optics. Later on, we described theoretical spectrum models for optical turbulence and—see Sec. 1.2. In addition, we review the significance of these studies by its application areas and its detrimental effects over these subjects.

In the latter Secs. 1.5 we review the equation governing the propagation of a beam through a random medium—*stochastics Helmholtz equation*, and the approximations to solving it. All over this section the Markovian approximation is used. It has dominated the Atmospheric Optics scenario among the classic models. It discriminates the direction of propagation, z, from the remaining coordinates. Thus, we used this model to calculate the effects of the turbulence over the beams. Thereafter, we explain some important quantities which describe the behavior of a beam propagatiny in a turbulent medium.

Afterwards, with the tools exposed in the first chapter we can advance to Chp. 2. Therein, we proposed a new optical setup to investigate the parameters of the turbulence, as well as the sampling rate for the optical turbulence. In the former experiment, we studied the statistical quantities for two thin beams which propagate in a turbulent atmosphere. The on– and off–plane covariances are given for non-Kolmogorov spectrum, under GO approximation with the aim of avoid the physical parameters of the beams. The filtered covariances via Wavelet shown a good agreement—see Fig. 2.14, with the theoretical results of Pérez and Funes (2012). Furthermore, we can deduce that the size of the smallest eddies are strongly dependent of the *Hurst exponent*—see Eq. (2.6).

On the other hand, the second experiment developed at this chapter, is based in the analysis of temporal series via Wavelet. It allows to determinate the WES and

its optimal sampling rate for the turbulence. The Wavelet analysis is independent of the model used and it can be extended for any optical configuration. For instance, in adaptive optics, Wavelet lets obtain the frequencies of the turbulence without any previous knowledge of the structure function or the wind velocity profile. Generally, information of the turbulence in any dynamic state (inertial, anysotropic, convective, etc. . .), strong or weak, can be studied.

Two main considerations should be used to determine an optimal sampling rate from the WES: the bell-shaped energy distribution corresponding to the optical turbulence must be completely visible for a given f_s; and the lowest and highest bands, associated to mechanical and electronic noise, should have a negligible signature in the spectrum. Under these conditions we can obtain a practical estimation of the optimal sampling rate without losing any information regarding the original dynamics. The advantage of this method is twofold. It permits to isolate noise from signal and be applied indistinctly to both stationary and non-stationary series. Finally, even though this approach is highly qualitative, it has proven to be fast and effective; therefore, our future objective is to improve it by using more complex wavelet transforms such as the wavelet packets Mallat (2009). This will allow us to identify the dominant frequencies in a more accurate way, and reduce any possible subjectivity in the optimal sample rate estimation.

In Chp. 3 we have developed an experiment which involves evapotranspiration by remote sensing, where we measured beyond the fluxes—see Sec. 3.3. We also measured the influence of intensity of turbulence to the evapotranspiration through the relationship between the structure constante of temperature C_T^2 and the refractive index structure parameter C_n^2. Good agreements are found between the SIRTA's instruments and our device to estimate evapotranspiration—see Fig. 3.9, we compare the results with FAO Penman-Monteith method as a reference for evapotranspiration (Zotarelli et al., 2010).

The values of C_n^2, obtained in this chapter, differ mainly because of the methods used. The Eq. (1.78) is obtained under Kolmogorov spectrum which does not take into account the scales of turbulence, and the "beam wander" method—see Eq. (1.71) is obtained considering the size of the eddies. Therefore, we applied the exponential spectrum model; of course, beam wandering is primarily an effect due to the refraction of large scales which are reflected in this spectrum. These differences affecting the

values of the refractive index structure parameter—see Fig. 3.6, the superposition of error bars in this figure show a good agreement.

On the other hand, the energy balance equation is explained by "The Surface Energy Balance Index (SEBI)" concept (Colin et al., 2006; Faivre, 2014).

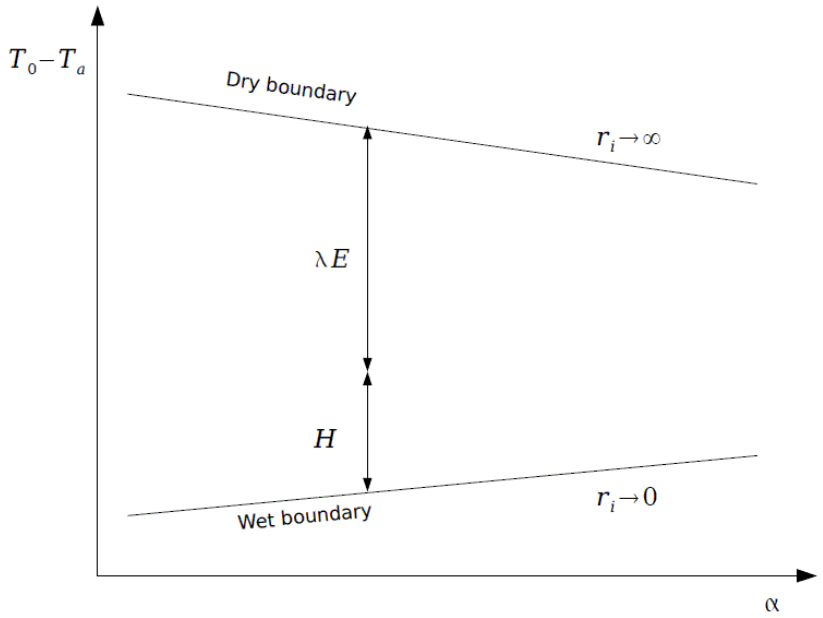

Figure 4.10: The SEBI concept, illustrated in terms of relationship between the land surface albedo—α, and the surface air temperature difference. Figure from Faivre (2014).

In Fig. 4.10, r_i is the internal resistance (or surface, or stomatal), which is regulated by soil water availability. Since the generic term of internal resistance apply for both bare soil and vegetation, it avoids to differentiate soil evaporation from plant transpiration. The range of $T_0 - T_a$ corresponds with an hypothetical change in evapotranspiration from zero to potential rate at constant surface reflectance and roughness.

The upper limit (i.e. the dry boundary) of surface-air temperature difference is a virtual temperature difference that would occur if the land surface becomes perfectly dry under the same meteorological and surface structure conditions of the actual case. That is, no water is evaporated from the surface. In addition, the low limit (i.e. the wet boundary) of surface-air temperature difference is another virtual temperature difference that would attain if the land surface is wet and evaporates at its potential rate under the same meteorological and surface structure conditions as the actual case.

Fig. 4.10 explains the Fig. 3.8, when the evapotranspiration λE increases the water in the atmospere also grows, to cooling the temperature. In addition, the sensible heat flux decreases because that the difference of temperature is reduced—see Sec. 3.3.1.

The deployment of the device was successful and measures have been carried out over a period of about 5 hours. Some minimal difficulties were encountered in beam alignment, probably due to transport material.

In addition, It is well known that the atmospheric factors are the most serious disadvantage to FSO because they can limit operating availability and/or cause distortions of the carrier wave that are uncommon to RF systems. Power losses associated with laser beam radiation in the visible range can be caused by absorption and scattering of the constituent gases and particulates of the atmosphere. In addition, optical turbulence resulting from small temperature variations in the atmosphere gives rise to further power losses from spreading of the beam spot radius beyond that due to diffraction alone, and to temporal and spatial fluctuations of the laser beam known as scintillation. Small pointing errors can easily lead to unacceptable fade levels owing to a Gaussian roll-off in the mean irradiance profile combined with large off-axis scintillation. Finally, In the latter Chp. 4, we presented a few unfinished works which are focused in this frame. At Secs. 4.2 and 4.3, we have studied experimentally the propagation of a phase-flipped Gaussian beam through optical turbulence and a supercontinuum beam, finding them as a good transmitter with a reduction on its fluctuations of intensity. For the former, the reduction is explained from the nature of the optical vortex, for instance, its scintillation index corresponds only a radial fluctuations of intensity, where there is not a longitudinal scintillation—analytical solution given under ideal condition (These results have been presented in SPIE. REMOTE SENSING, Centre de Congrès Pierre Baudis., 21 - 24 September 2015 in Toulouse, France). This vortex beam is presented as a new transmitter for experiments which involve optical wave propagation, improving the transmission of information through the atmosphere and the performance of various optical communication system as measured by the BER, e.g., in case of bidirectional earth-space transmission, uplink, downlink and horizontal paths. The latter Fig. 4.5 showed a experimental decreasing for the scintillation index of a flipped mode, regarding the Gaussian beam. Same behavior is observed for a supercontinumm in according with the scintillation index for a Gaussian beam—Fig. 4.9. This result can be explained (maybe) due to the contribution of all the wavelengths, i.e.

for a SC beam, the multi-wavelengths balanced out the fluctuation for each wavelength because of the continuity existent between the wavelengths, as a result, reduces the intensity fluctuations. Thereby, supercontinuum light is a high-performance transmitter through optical turbulence for all the propagation path—its theory still in progress.

All the latter sections at the Chp. 4, are between the main goals of this year.

Appendix A

In Sec. 4.2.3 we have developed the physical propagation through atmospheric turbulence of a special beam, which is derivative it from a Gaussian beam, currently called *flipped mode*. Herein, we review in detail the equations for its free space propagation.

Propagation into half-space

The complex amplitude for Eq. (4.3) at propagation distance z from the source is given by Huygens-Fresnel integral

$$U_0^{PF}(\mathbf{r}, z) = -2ik \int_{-\infty}^{\infty} \int_{-\infty}^{\infty} G(\mathbf{s}, \mathbf{r}, z) U_0^{PF}(\mathbf{s}, 0)\ d^2s$$

where $U_0^{PF}(\mathbf{s}, 0)$ is the optical wave for a flipped Gaussian mode at the source plane and $G(\mathbf{s}, \mathbf{r}, z)$ is the free-space Green's function under the paraxial approximation, thus

$$\begin{aligned} U_0^{PF}(\mathbf{r}, z) &= \frac{ik}{2\pi z} \exp\left[ikz + \frac{ik}{2z} r^2\right] \times \\ &\times \int_{-\infty}^{\infty} \int_{-\infty}^{\infty} \exp\left[-\frac{ik}{z} \mathbf{s} \cdot \mathbf{r}\right] \exp\left[\frac{ik}{2z} \left(1 + i\alpha_0 z\right) s^2\right] \exp[-i\pi H(k s_x)]\ d^2s \end{aligned} \tag{A.1}$$

we introduced the complex parameter α_0, which is related to the spot size and phase front radius of curvature according to $\alpha_0 = (2/kW_0^2) + (i/F_0)$ in $[\mathsf{m}^{-1}]$. The integral of Eq. (A.1) is calculated in rectangular coordinates. By the "complete squares" method at each exponential, yields a general expression

$$I \equiv \frac{\exp[-ia_u^2/(4b)]}{\sqrt{b}} \int_{t_1}^{t_2} \exp\left[it^2\right]\ dt \tag{A.2}$$

where

$$a_u \equiv \frac{ku}{z}, \quad u = x, y.$$
$$b \equiv \frac{k}{2z}\left(1 + i\alpha_0 z\right),$$
$$t \equiv \sqrt{b}s_u - \frac{a_u}{2\sqrt{b}}.$$

From the integral in Gradshteyn and Ryzhik (2007, Functional relations 8.256),

$$\sqrt{\frac{i}{2}}\ \mathrm{erf}\left(\frac{z}{\sqrt{i}}\right) = \frac{2}{\sqrt{2\pi}}\int_0^z \exp[it^2]\ dt \tag{A.3}$$

Eq. (A.3) features the error function—erf(·), or also called probability integral. Straightforward, Eq. (A.1) becomes

$$U_0^{PF}(x,y,z) = \frac{i\exp[ikz]}{(1+i\alpha_0 z)}\exp\left[\frac{ik}{2z}\left(\frac{i\alpha_0 z}{1+i\alpha_0 z}\right)\left(x^2+y^2\right)\right]\mathrm{erfi}\left[x\sqrt{\frac{ik}{2z(1+i\alpha_0 z)}}\right] =$$
$$= U_0(x,y,z)\mathrm{erf}\left[x\sqrt{\frac{k}{2iz}(\Theta - i\Lambda)}\right] \tag{A.4}$$

we applied the transformation of the imaginary error function—erfi(·), and the following equalities

$$i\ \mathrm{erfi}(x) = \mathrm{erf}(ix) \tag{A.5}$$
$$\frac{i\alpha_0 z}{1+i\alpha_0 z} = \overline{\Theta} + i\Lambda \tag{A.6}$$
$$\frac{1}{1+i\alpha_0 z} = \frac{1}{\Theta_0 + i\Lambda_0} = \Theta - i\Lambda \tag{A.7}$$

The Eq. (A.4) corresponds to Eq. (4.4) at Sec. 4.2.3, and we can identify clearly the electric field for a Gaussian beam wave at distance z—Eq. (4.5).

Phase–flipped Gaussian beam intensity

The irradiance or intensity of the optical wave is the squared magnitude of the field,

$$\begin{aligned} I^{PF}(\mathbf{r},z) &= |U_0^{PF}(\mathbf{r},z)|^2 = U_0^{PF}(\mathbf{r},z)\cdot U_0^{*PF}(\mathbf{r},z) = \\ &= \frac{4}{\pi} I^0(0,z)\exp\left[-\frac{2y^2}{W^2}\right] \mathrm{F}\left[x\sqrt{\frac{ik}{2z}(\Theta - i\Lambda)}\right] \mathrm{F}\left[x\sqrt{\frac{-ik}{2z}(\Theta + i\Lambda)}\right] \end{aligned} \tag{A.8}$$

where $W = W_0\sqrt{\Theta_0^2 + \Lambda_0^2}$ is the free space beam radius, $I^0(0,z)$ is the on-axis irradiance, and $\mathrm{F}(x)$ denotes the Dawson's Integral which is related to the imaginary error function

$$\mathrm{F}(x) = \frac{\sqrt{\pi}}{2}\exp\left[-x^2\right]\mathrm{erfi}(x)$$

The total power is given by

$$\begin{aligned} P &= \int_{-\infty}^{\infty}\int_{-\infty}^{\infty} I^{PF}(\mathbf{r},z)\; d^2r = \\ &= \frac{4}{\pi} I^0(0,z)\int_{-\infty}^{\infty}\exp\left[-\frac{2y^2}{W^2}\right]\; dy\times \\ &\times \int_{-\infty}^{\infty}\mathrm{F}\left[x\sqrt{\frac{ik}{2z}(\Theta - i\Lambda)}\right]\mathrm{F}\left[x\sqrt{\frac{-ik}{2z}(\Theta + i\Lambda)}\right] dx \end{aligned} \tag{A.9}$$

the integral in direction x is computed by the software *Mathematica*

$$\begin{aligned} \int_{-\infty}^{\infty}\mathrm{F}\left[x\sqrt{\frac{ik}{2z}(\Theta - i\Lambda)}\right]\mathrm{F}\left[x\sqrt{\frac{-ik}{2z}(\Theta + i\Lambda)}\right] dx = \\ = \frac{\pi^{3/2}}{4\sqrt{\frac{i\Lambda}{\Theta+i\Lambda}}\sqrt{\frac{k}{z}(\Lambda - i\Theta)}} \end{aligned} \tag{A.10}$$

and in direction y

$$\int_{-\infty}^{\infty}\exp\left[-\frac{2y^2}{W^2}\right]\; dy = \sqrt{\frac{\pi}{2}}W \tag{A.11}$$

these integrals simplify the Eq. (A.9)

$$P = \int_{-\infty}^{\infty}\int_{-\infty}^{\infty} I^{PF}(\mathbf{r},z)\; d^2r = \frac{\pi}{2}W_0^2 \tag{A.12}$$

The result correspond to the power of a Gaussian beam and there is no loss of power, as we expected.

Statistical moments for a flipped mode

To review the free-space propagation of the flipped Gaussian mode under *Rytov theory*, we need to review the spectral representations for Born and Rytov perturbations—see Sec. 1.5. The stochastic optical field at distance $z = L$ from the transmitter will be represented by $U^{PF}(\mathbf{r}, L) = U_0^{PF}(\mathbf{r}, L)\exp[\Psi(\mathbf{r}, L)]$, where $U_0^{PF}(\mathbf{r}, L)$ is the unperturbed—unscattered field, given by Eq. (A.4) and $\Psi(\mathbf{r}, L)$ is the total complex phase perturbation of the field due to random inhomogeneities along the propagation path, which is assumed as a Gaussian random variable under weak-turbulence condition. Currently, the first-order Born perturbation was given in Sec. 1.5,

$$\begin{aligned}\Phi_1^{PF}(\mathbf{r}, L) &= \frac{U_1^{PF}(\mathbf{r}, L)}{U_0^{PF}(\mathbf{r}, L)} = \\ &= \frac{k^2}{2\pi}\int_0^L dz \int\int_{-\infty}^{\infty} d^2s \exp\left[ik(L-z) + \frac{ik|\mathbf{s}-\mathbf{r}|^2}{2(L-z)}\right]\frac{U_0^{PF}(\mathbf{s}, z)}{U_0^{PF}(\mathbf{r}, L)}\frac{n_1(\mathbf{s}, z)}{(L-z)},\end{aligned} \tag{A.13}$$

and the first-order spectral representation for a phase-flipped Gaussian beam will be written with the help of the two-dimensional Riemann-Stieltjes integral form for the index-of-refraction fluctuations—see Eq. (1.49) at Sec. 1.5. Eq. (A.13) in rectangular coordinates, thus

$$\begin{aligned}&\Phi_1^{PF}(x, y, L) = \\ &= \frac{k^2}{2\pi}\frac{1}{\operatorname{erf}\left[x\sqrt{\frac{k}{2iL}(\Theta(L) - i\Lambda(L))}\right]}\int_0^L dz \int_{-\infty}^{\infty}\int_{-\infty}^{\infty}\frac{d\nu(\kappa_x, \kappa_y, z)}{\gamma(L-z)}\exp\left[i\frac{k\gamma(x^2+y^2)}{2(L-z)}\right]\times \\ &\quad\times\int_{-\infty}^{\infty}\exp\left[i\frac{ks_x^2}{2(L-z)\gamma} + is_x\left(\kappa_x - \frac{kx}{L-z}\right)\right]\operatorname{erf}\left[s_x\sqrt{\frac{k}{2iz}(\Theta(z) - i\Lambda(z))}\right]ds_x\times \\ &\qquad\times\int_{-\infty}^{\infty}\exp\left[i\frac{ks_y^2}{2(L-z)\gamma} + is_y\left(\kappa_y - \frac{ky}{L-z}\right)\right]ds_y,\end{aligned} \tag{A.14}$$

From the integral in Gradshteyn and Ryzhik (2007, Functional relations 8.259, Eq. 1), will resolving the integral in direction x

$$\int_{-\infty}^{\infty} \exp\left[-px^2\right] \operatorname{erf}[a+bx]\, dx = \sqrt{\frac{\pi}{p}} \operatorname{erf}\left[\frac{a\sqrt{p}}{\sqrt{b^2+p}}\right], \quad \text{Re } p > 0, \quad a, b \text{ real.} \tag{A.15}$$

The equation above is an improper integral and its functions are entire (analytical without singularities), by virtue of Cauchy Integral theorem the integral in complex plane is the same as in the Real line, i.e. for a and b complex, the integral remains invariant. The reason is that as a result of shifting the integration countour into the complex plane no singularities are encountered. On the other hand, for direction y, the "complete squares" method yields a general expression

$$\int_{-\infty}^{\infty} \exp\left[At^2 + Bt\right] dt = \frac{\exp[-B^2/(4A)]\,\sqrt{\pi}}{\sqrt{-A}}, \quad \text{Re } A < 0. \tag{A.16}$$

These integrals allow to write the first-order spectral representation as

$$\Phi_1^{PF}(\mathbf{r}, L) = \frac{U_1^{PF}(\mathbf{r}, L)}{U_0^{PF}(\mathbf{r}, L)} =$$
$$= ik \int_0^L dz \int\int_{-\infty}^{\infty} d\nu(\boldsymbol{\kappa}, z) \exp\left[i\gamma\boldsymbol{\kappa}\cdot\mathbf{r} - \frac{i\kappa^2\gamma}{2k}(L-z)\right] \frac{\operatorname{erf}\left[\left(\frac{x}{W} - \frac{(L-z)}{kW}\kappa_x\right)\sqrt{\frac{\Theta_0 - i\Lambda_0}{i\Lambda_0}}\right]}{\operatorname{erf}\left[\frac{x}{W}\sqrt{\frac{\Theta_0 - i\Lambda_0}{i\Lambda_0}}\right]} \tag{A.17}$$

where we used $\mathbf{r} = (x, y)$ and the parameter γ—from Eq. (1.53) at Sec. 1.5. In addition, the second order Born perturbation is defined by Eq. (1.46). The substitution of Eqs. (1.49), (A.17), (A.15) and (A.16), yield the second-order spectral representation

for a flipped mode

$$\Phi_2^{PF}(\mathbf{r},L)=\frac{U_2^{PF}(\mathbf{r},L)}{U_0^{PF}(\mathbf{r},L)}=-k^2\int_0^L dz\int_0^z dz'\int_{-\infty}^{\infty}\int_{-\infty}^{\infty}\int_{-\infty}^{\infty}\int_{-\infty}^{\infty}d\nu(\boldsymbol{\kappa},z)d\nu(\boldsymbol{\kappa}',z')\times$$
$$\times\exp\left[i\gamma(\boldsymbol{\kappa}+\gamma'\boldsymbol{\kappa}')\cdot\mathbf{r}-\frac{i\gamma|\boldsymbol{\kappa}+\gamma'\boldsymbol{\kappa}'|^2}{2k}(L-z)-\frac{i\kappa'^2\gamma'}{2k}(z-z')\right]\times$$
$$\times\frac{\operatorname{erf}\left[\left(\frac{x}{W}-\frac{(L-z)}{kW}\kappa_x-\left(\frac{z-z'}{\gamma(L-z)}+\gamma'\right)\frac{(L-z)}{kW}\kappa_x'\right)\sqrt{\frac{\Theta_0-i\Lambda_0}{i\Lambda_0}}\right]}{\operatorname{erf}\left[\frac{x}{W}\sqrt{\frac{\Theta_0-i\Lambda_0}{i\Lambda_0}}\right]},\quad\text{(A.18)}$$

with $\gamma'=(1+i\alpha_0 z')/(1+i\alpha_0 z)$.

Carrying on, we compute the statistical moments defined in Sec. 1.5.2. For the case when $n_1(\mathbf{R})$ is delta correlated in the direction of propagation—often referred to as the *Markov approximation*, we have $\kappa_z=0$ and the power spectrum reduces to $\Phi_n(\boldsymbol{\kappa})=\Phi_n(\kappa_x,\kappa_y,0)$. Consequently, we introduce the *two-dimensional spectral density* $F_n(\boldsymbol{\kappa},z)$ defined by the transform Fourier relation,

$$2\pi\ \Phi_n(\boldsymbol{\kappa})=\int_{-\infty}^{\infty}F_n(\boldsymbol{\kappa},z)dz.\quad\text{(A.19)}$$

we have assumed a medium statistically homogeneous so each quantity are a function of only the difference $\mathbf{R}_1-\mathbf{R}_2$. In addition, we assume that the beam propagates through an isotropic random medium in each transverse plane, then we can replace $\boldsymbol{\kappa}$ by its scalar magnitude κ, that is $\Phi_n(\boldsymbol{\kappa})=\Phi_n(\kappa)$.

Next, to ensure statistical homogeneity of the refractive index, we have to write for $E_2(\mathbf{r}_1,\mathbf{r}_2)$—see Eq. (1.59),

$$\langle d\nu(\boldsymbol{\kappa},z)d\nu^*(\boldsymbol{\kappa}',z')\rangle=F_n(\boldsymbol{\kappa},|z-z'|)\delta(\boldsymbol{\kappa}-\boldsymbol{\kappa}')d^2\kappa d^2\kappa',\quad\text{(A.20)}$$

where δ is the delta function—$\delta(\boldsymbol{\kappa}\pm\boldsymbol{\kappa}')=\delta(\kappa_x\pm\kappa_x')\delta(\kappa_y\pm\kappa_y')$, and based on the fact that $n_1(\mathbf{s},L)$ is a real function; the "amplitudes" $d\nu(\boldsymbol{\kappa},z)$ for $E_1(\mathbf{r},\mathbf{r})$ and $E_3(\mathbf{r}_1,\mathbf{r}_2)$—see Eq. (1.58) and Eq. (1.60), satisfy the relation (Andrews and Phillips,

1998, Sec. 5.4.3)

$$\begin{aligned}\langle d\nu(\boldsymbol{\kappa}, z)d\nu(\boldsymbol{\kappa}', z')\rangle &= \langle d\nu(\boldsymbol{\kappa}, z)d\nu^*(-\boldsymbol{\kappa}', z')\rangle \\ &= F_n(\boldsymbol{\kappa}, |z - z'|)\delta(\boldsymbol{\kappa} + \boldsymbol{\kappa}')d^2\kappa d^2\kappa',\end{aligned} \tag{A.21}$$

with the two-dimensional spectral density of the index of refraction—$F_n(\boldsymbol{\kappa}, |z-z'|) \geq 0$ (Tatarskĭ, 1971, Chp. 1—Sec. 4).

Bibliography

AhmadiKanjani, S., R. Barillé, S. DabosSeignon, J.-M. Nunzi, E. Ortyl and S. Kucharski (2005), 'Multistate polarization addressingusing one single beam in an azopolymer film.', *Opt. Lett.* **30**(15), 1986–1988.

Andrews, Larry C. and Ronald L. Phillips (1998), *Laser Beam Propagation Through Random Media.*, SPIE Press.

Andrews, Larry C. and Ronald L. Phillips (2005), *Laser Beam Propagation Through Random Media. Second edition*, SPIE Press.

Banerji, J. (2006), 'Propagation of a phase flipped gaussian beam through a paraxial optical abcd system.', *Opt. Com.* **258**, 1–8.

Barillé, R., A. Poisson, A. Fernández, D. G. Pérez and Jean-CharlesDupont (2016), 'Thin laser beam wanderingand intensity fluctuations method for evapotranspiration measurement', *Optics & LaserTechnology* **80**, 33–40.

Barillé, R., D. G. Pérez, Y. Morille, S. Zielińska and E. Ortyl (2013), 'Simple turbulence measurements with azopolymer thin films.', *Opt. Lett.* **38**, 1128–1130.

Barillé, R., P. Tajalli, J. M. Nunzi, S. Zielioskaaand, E. Ortyl and S. Kucharski (2009), 'Surface relief grating on azopolymer nanosurface.', *Appl. Phys. Lett.* **95**(053102).

Cai, J., Y. Liu, T. Lei and L. Pereira (2007), 'Estimating reference evapotranspiration with the fao penman–monteith equation using daily weather forecast messages', *Agr. For. Meteorol.* **145**, 22–35.

Cai, Yangjian, Yuntian Chen, Halil T. Eyyuboglu and Yahya Baykal (2007), 'Scintillation index of elliptical gaussian beam in turbulent atmosphere', *Opt. Lett.* **32**(16), 2405–2407.

Charnotskii, Mikhail. (2015), 'Extended huygens—fresnel principle and optical waves propagation in turbulence: discussion.', *J. Opt. Soc. Am. A.* **32**, 1357 –1365.

Chen, Ziyang, Shengwei Cui, Lei Zhang, Cunzhi Sun, Mengsu Xiong and Jixiong Pu (2014), 'Measuring the intensity fluctuation of partially coherent radially polarized beams in atmospheric turbulence', *Opt. Express* **22**(15), 18278–18283.

Cheng, Wen, Joseph W. Haus and Qiwen Zhan (2009), 'Propagation of vector vortex beams through a turbulent atmosphere', *Opt. Express* **17**(20), 17829–17836.

Colin, J., M. Menenti, E. Rubio and A. Jochum (2006), 'A multi scales surface energy balance system for operational actual surface evapotranspiration monitoring.', *AIP Conference Proceedings.* **852**, 178.

Consortini, A. and K. O'Donnell (1991), 'Beam wandering of thin parallel beams through atmospheric turbulence.', *Waves in Random Media.* **3**, S11–S28.

Consortini, A and K. O'Donnell (1993), 'Measuring the inner scale of atmospheric turbulence by correlation of lateral displacements of thin parallel laser beams.', *Waves in Random Media.* **3**, 85–92.

De Bruin, H. A. R., B.J. Van Den Hurk and W. Kohsiek (1995), 'The scintillation method tested over a dry vineyard area.', *Boundary- Layer Meteorol.* **76**(1–2), 25–40.

Delaubert, V., D. A. Shaddock, P. K. Lam, B. C. Buchler, H-A. Bachor and D. E. McClelland (2002), 'Generation of a phase-flipped gaussian mode for optical measurements', *J. Opt. A: Pure Appl.* **4**, 393–399.

Dennis, Mark R., Kevin. O'Holleran and Miles J. Padgett (2009), *Progress in Optics.*, Elsevier.

Dudley, J. M., G. Genty and S. Coen (2006), 'Supercontinuum generation in photonic crystal fiber', *Rev. Mod. Phys.* **78**, 1135 –1184.

Eyyuboğlu, H.T., Y. Baykal and Y. Cai (2008), 'Scintillations of laser array beams', *Applied Physics B* **91**(2), 265–271.

Ezzahar, J., A. Chehbouni, J. C. B. Hoedjes, S. Er-Raki, Chehbouni. Ah, J. M. Boulet, G. Bonnefond and H. A. R. De Bruin (2007), 'The use of the scintillation technique for monitoring seasonal water consumption of olive orchards in a semi-arid region.', *Agric. Water Manag.* **89**(3), 173–184.

Faivre, Robin. (2014), Multi-sensor remote sensing parametrization of heat fluxes over heterogeneous land surfaces, Ph.D. thesis, Université de Strasbourg.

Funes, Gustavo (2014), Desarrollo, análisis y aplicación de nuevos modelos para la propagación láser en medios turbulentos, Ph.D. thesis, Universidad Nacional de La Plata.

Funes, Gustavo, Ángel Fernández, Darío G. Pérez, Luciano Zunino and Eduardo Serrano (2013), 'Estimating the optimal sampling rate using wavelet transform: an application to optical turbulence', *Opt. Express* **21**(13), 15230–15236.

Gbur, Greg and Robert K. Tyson (2008), 'Vortex beam propagation through atmospheric turbulence and topological charge conservation.', *J. Opt. Soc. Am. A.* **25**, 225–230.

Gibson, Graham, Johannes Courtial, Miles J. Padgett, Mikhail Vasnetsov, Valeriy Pas'ko, Stephen M. Barnett and Sonja Franke-Arnold (2004), 'Free-space information transfer using light beams carrying orbital angular momentum', *Opt. Express* **12**(22), 5448–5456.

Gradshteyn, I. S. and I. M. Ryzhik (2007), *Table of integrals, Series, and Products*, seventh edition edn, Academic Press.

Gu, Y. and G. Gbur (2010), 'Scintillation of airy beam arrays in atmospheric turbulence.', *Opt. Lett.* **35**(20), 3456–3458.

Gu, Yalong and Greg Gbur (2012), 'Reduction of turbulence-induced scintillation by nonuniformly polarized beam arrays', *Opt. Lett.* **37**(9), 1553–1555.

Gu, Yalong, Olga Korotkova and Greg Gbur (2009), 'Scintillation of nonuniformly polarized beams in atmospheric turbulence', *Opt. Lett.* **34**(15), 2261–2263.

Hill, R. J., S. F. Clifford and R.S. Lawrence (1980), 'Refractive-index and absorption fluctuations in the infrared caused by temperature, humidity, and pressure fluctuations.', *J. Opt. Soc. Am.* **70**, 1192–1205.

Innocenti, C. and A. Consortini (2005), 'Refractive index gradient of the atmosphere at near ground levels.', *J. Mod. Opt.* **52**, 671–689.

Ji, Xiaoling, Halil T. Eyyuboğlu and Yahya Baykal (2010), 'Influence of turbulence on the effective radius of curvature of radial gaussian array beams', *Opt. Express* **18**(7), 6922–6928.

Keskin, Onur., Laurent. Jolissaint and Colin. Bradley (2006), 'Hot-air optical turbulence generator for the testing of adaptive optics systems: principles and characterization.', *Appl. Opt.* **45**, 4888 –4897.

Kolmogorov, A. N. (1941), 'Local structure of turbulence in an incompressible viscous fluid at very large Reynolds numbers', *Dokl. Akad. Nauk. SSSR* **30**(4), 299–301.

Korotkova, Olga. (2008), 'Scintillation index of a stochastic electromagnetic beam propagating in random media', *Opt. Com.* **281**, 2342 –2348.

Korotkova, Olga. and Elena. Shchepakina (2010), 'Color changes in stochastic light fields propagating in non-kolmogorov turbulence', *Opt. Lett.* **35**, 3772 –3774.

Korotkova, Olga and Emil Wolf (2007), 'Beam criterion for atmospheric propagation', *Opt. Lett.* **32**(15), 2137–2139.

Korotkova, Olga., Serkan. Sahin and Elena. Shchepakina (2012), 'Multi-gaussian schell-model beams', *J. Opt. Soc. Am. A.* **29**, 2159 –2164.

Li, Zhao-Liang., Ronglin. Tang, Bi Yuyun. Wan, Zhengming, Chenghu. Zhou, Bohui Tang, Guangjian Yan and Xiaoyu. Zhang (2009), 'A review of current methodologies for regional evapotranspiration estimation from remotely sensed data.', *Sensors.* **9**, 3801–3853.

Liu, Xianhe and Jixiong Pu (2011), 'Investigation on the scintillation reduction of elliptical vortex beams propagating in atmospheric turbulence', *Opt. Express* **19**(27), 26444–26450.

Makynen, A.J., J.T. Kostamovaara and R.A. Myllyla (1996), 'Positioning resolution of the position-sensitive detectors in high background illumination.', *IEEE Trans. In-strum. Meas.* **45**, 324–326.

Makynen, A.J., J.T. Kostamovaara and R.A. Myllyla (1997), 'Displacement sensing resolution of position-sensitive detectors in atmospheric turbulence using retroreflected beam.', *IEEE Trans. In-strum. Meas.* **46**, 1133–1136.

Mallat, S. (2009), *A wavelet tour of signal processing.*, Academic Press, Elsevier.

Manojlovic, L. M. (2011), 'Quadrant photodetector sensitivity', *Appl. Opt.* **50**(20), 3461–3469.

Masciadri, E. and J. Vernin (1997), 'Optical technique for inner-scale measurement: possible astronomical applications.', *Appl. Opt.* **36**, 1320–1327.

Meijninger, W. M. L., O. K. Hartogensis, W. Kohsiek, J. C. B. Hoedjes, R. M. Zuurbier and H. A. R. De Bruin (2002), 'Determination of area-averaged sensible heat fluxes with a large aperture scintillometer over a heterogeneous surface– flevoland field experiment.', *Boundary- Layer Meteorol.* **105**(1), 37–62.

Moene, A. F., W. M. L Meijninger, O. K. Hartogensis, W. Kohsiek and H. A. R. Debruin (2004), 'A review of the relationships describing the signal of a large aperture scintillometer.', *Meteorology and Air Quality Group, Wageningen University, Wageningen, the Netherlands* **Internal Report 2004/2.**, 40.

Owens, J. C. (1967), 'Optical refractive index of air: Dependence on pressure, temperature and composition', *Appl. Opt.* **6**(1), 51–59.

Peleg, Avner and Jerome V. Moloney (2006), 'Scintillation index for two gaussian laser beams with different wavelengths in weak atmospheric turbulence', *J. Opt. Soc. Am. A* **23**(12), 3114–3122.

Pérez, Darío G. (2010), 'Atmospheric and Statistical Optics Laboratory', `http://atsol.fis.ucv.cl/experiments/dltmm`.

Pérez, Darío G. and Gustavo Funes (2012), 'Beam wandering statistics of twin thin laser beam propagation under generalized atmospheric conditions', *Opt. Express* **20**(25), 27766–27780.

Pérez, Darío G. and Gustavo Funes (2015), 'On a quasi-wavelet model of refractive index fluctuations due to atmospheric turbulence', *Opt. Express* **23**(25), 31627–31639.

Polynkin, Pavel, Avner Peleg, Laura Klein, Troy Rhoadarmer and Jerome Moloney (2007), 'Optimized multiemitter beams for free-space optical communications through turbulent atmosphere', *Opt. Lett.* **32**(8), 885–887.

Pérez, Darío G., Ángel Férnandez, Gustavo Funes, Damián Gulich and Luciano Zunino (2012), 'Retrieving atmospheric turbulence features from differential laser tracking motion data', *Proc. SPIE* **8535**, 853508–853508–11.

Qian, Xianmei, Wenyue Zhu and Ruizhong Rao (2009), 'Numerical investigation on propagation effects of pseudo-partially coherent gaussian schell-model beams in atmospheric turbulence', *Opt. Express* **17**(5), 3782–3791.

Rana, G. and N. Katerji (2000), 'Measurement and estimation of actual evapotranspiration in the field under mediterranean climate: a review.', *Eur.J. Agron.* **13**, 125–153.

Schulz, Timothy J. (2005), 'Optimal beams for propagation through random media', *Opt. Lett.* **30**(10), 1093–1095.

Solignac, P.-A. (2009), *Conception, réalisation et mise en oeuvre d'un scintillomètre: influence de la vapeur d'eau dans la bande* 940 *nm*, Centre d'Etudes Spatiales de la Biosphère-CESBIO, Toulouse, France.

Tatarskĭ, V. I. (1961), *Wave Propagation in a Turbulent Medium*, Mc Graw-Hill, New York.

Tatarskĭ, V. I. (1967), *Wave Propagation in a Turbulent Atmosphere*, Nauka Press, Moscow.

Tatarskĭ, V. I. (1971), *Effect of the Turbulent Atmosphere on Wave Propagation*, Israel Program for Scientific Translations, Jerusalem.

Toselli, Italo, Larry C. Andrews, Ronald L. Phillips and Valter Ferrero (2007), 'Angle of arrival fluctuations for free space laser beam propagation through non kolmogorov turbulence'.

Tunick, A. (2003), 'c_n^2 model to calculate the micrometeorological influences on the refractive index structure parameter', *Environ. Model. Softw.* **18**, 165–171.

Tyson, Robert K. (2002), 'Bit-error rate for free-space adaptive optics laser communications.', *J. Opt. Soc. Am. A.* **19**, 753 –758.

Čelechovský, Radek and Zdeněk Bouchal (n.d.), 'Optical implementation of the vortex information channel', *New Journal of Physics* **9**(9), 328.

Von Randow, C., B. Kruijt, A. A. M. Holtslag and A. B. L. De Oliveira (2008), 'Exploring eddy-covariance and large-aperture scintillometer measurements in an amazonian rain forest', *Agric. For. Meteorol.* **148**, 680–690.

Wang, Fei, Yangjian Cai, Halil T. Eyyuboğlu and Yahya Baykal (2012), 'Twist phase-induced reduction in scintillation of a partially coherent beam in turbulent atmosphere', *Opt. Lett.* **37**(2), 184–186.

Wang, Ting-i., G. R. Ochs and S. F. Clifford (1978), 'A saturation-resistant optical scintillometer to measure c_n^2.', *J. Opt. Soc. Am.* **68**, 334–338.

Zotarelli, Lincoln, Michael D. Dukes, Consuelo C. Romero, Kati W. Migliaccio and Kelly T. Morgan (2010), 'Step by step calculation of the penman-monteith evapotranspiration (fao-56 method).', *Agricultural and Biological Engineering Department, UF/IFAS Extension.* .

UNIVERSITE BRETAGNE LOIRE

université angers

Thèse de Doctorat

Angel Martin FERNANDEZ ALVAREZ

Expériences pour la Propagation d'un Faisceau Laser à travers de Turbulence Optique. Développement, Analyse et Applications.

Experiments for Laser Beam Propagation through Optical Turbulence: Development, Analysis and Applications.

Résumé

La turbulence atmosphérique générée par une différence de température entre la surface de la Terre et l'atmosphère, provoque des effets sur les ondes optiques et présente un grand intérêt pour les scientifiques depuis de nombreuses années. Les distorsions du front d'onde optique induites par le résultat de la turbulence atmosphérique génèrent un étalement du faisceau au-delà de celui dû à la diffraction pur, des variations aléatoires de la position du centre de gravité du faisceau, et une répartition aléatoire de l'énergie du faisceau qui conduit à des fluctuations de l'irradiance.
Ces effets ont des conséquences sur l'imagerie astronomique, les communications optiques en espace libre (OFS), la télédétection, la communication par satellite laser, l'imagerie astronomique, l'optique adaptative, la désignation de cible, le LiDAR hyperspectral, et d'autres applications qui nécessitent la transmission d'ondes optiques dans l'atmosphère sur une grande portée.
Tout au long de cette thèse, nous introduisons le concept général de la turbulence, en se concentrant sur la turbulence atmosphérique. Diverses expériences ont été réalisées, par exemple, la propagation de deux minces faisceaux parallèles dans les conditions de l'optique géométrique pour l'étude des paramètres de turbulence optiques. La même configuration optique a été utilisé pour étudier la meilleure fréquence d'échantillonnage pour la turbulence optique. En outre, nous avons indirectement mesuré l'évapotranspiration, pour laquelle nous tenons compte des fluctuations de l'indice de réfraction de la turbulence à travers les variations d'intensités du faisceau laser. Enfin, certaines expériences qui considèrent de nouveau émetteur ont également été développées, tel que le saut de mode montre une réduction expérimentale des fluctuations de l'irradiance induite par la turbulence. Ce faisceau a une meilleure performance comme émetteur d'informations pour la communication optique en espace libre.

Mots clés
Turbulence atmosphérique – propagation d'un faisceau laser, processus stochastiques – Evapotranspiration.

Abstract

Atmospheric turbulence, generated by a differential temperature between the Earth's surface and the atmosphere, causes effects on optical waves that have been of great interest to scientists for many years. Wave front distortions in the optical wave induced by atmospheric turbulence result in a spreading of the beam beyond that due to pure diffraction, random variations of the position of the beam centroid, and a random redistribution of the beam energy within a cross section of the beam leading to irradiance fluctuations. Those effects have far-reaching consequences on astronomical imaging, free space optics (FSO) communications, remote sensing, laser satellite communication, astronomical imaging, adaptive optics, target designation, hyperspectral LiDAR, and other applications that require the transmission of optical waves through the atmosphere.
Throughout this thesis, we introduce a globally concept of *turbulence*, focusing in atmospheric turbulence. Diverse experiments have been carried out, for instance, the propagation of two parallel thin beams under geometrical optics condition for studying the parameters of optical turbulence, and besides, the same optical configuration was used to investigate the best sampling rate for optical turbulence. Furthermore, we have measured evapotranspiration by remote sensing, in which we have heeded the fluctuations of the refractive index through the intensities of the turbulence. Finally, experiments which involve a new beam are also developed, such as *phase-flipped Gaussian beam*. This beam shows an experimental reduction on its irradiance fluctuations induced by the turbulence, which means that it has a high performance in optical communications. The experimental reduction aforementioned is proved through the comparison with the theory developed.

Key Words
Atmospheric Turbulence. Laser Beam Propagation. Stochastic Process and Statistics. Turbulence. Evapotranspiration.

L'Université Bretagne Loire
UTFSM & PUCV